Sensitivity and resolution in 19F and 15N solid-state NMR: applications to pharmaceutical systems

ROBBINS, ANDREW,JAMES

1 Sensitivity and resolution in ^{19}F and ^{15}N solid-state NMR: applications to pharmaceutical systems

Andrew James Robbins

University of Durham

A thesis submitted in partial fulfillment of the requirements
For the degree of Doctor of Philosophy

Supervisors: Dr. Paul Hodgkinson, Dr. Alessia Portieri (AZ)
and Dr. Andrew Phillips (AZ)

Department of Chemistry, University of Durham
2009

Abstract

'Sensitivity and resolution in ^{19}F and ^{15}N solid-state NMR: applications to pharmaceutical systems'

PhD thesis Andrew J. Robbins June 09

This thesis describes a study into the improvement of solid-state NMR methods for the detection and characterisation of pharmaceutical compounds.

The revised thesis addresses the different specific comments and corrections listed by the examiners, including the addition of a section at the start of Chapter 1 on the quantum mechanical basis of NMR. In response to the general structural problems, Chapters 1 and 2 in particular have been completely revised to remove repetition and overlap between the different sections. Problems with section numbering have been corrected and the cross-referencing improved. The chapters on ^{15}N indirect detection and ^{19}F linewidths also have been revised to eliminate repetition and improve the overall flow. The original chapter on REDOR, which was not central to the original work, has been moved to an appendix. The final text is now much tidier and considerably more compact (shorter by about 40 pages).

Chapter 1 Introduces the principles of solid-state NMR from the quantum mechanical basis to the vector model and the various interactions involved in solids NMR.

Chapter 2 outlines the key experimental techniques employed within this work.

Chapter 3 investigates the usefulness of indirect detection as a method to detect and possibly quantify the ratio of ^{15}N present for multiple ^{15}N containing systems. The work highlights how cross-polarisation at fast MAS is affected by the RF inhomogeneity of the probe, and how this is reduced by using ramped CP. The ^{15}N indirect detection is found to be useful for certain applications, although it is not a simple replacement for standard direct detection.

Chapter 4 Investigates the factors that determine ^{19}F resolution in solid-state NMR. A large number of model compounds were selected to reflect the broad range of possible fluorine environments, and the homogeneous and inhomogeneous linewidths investigated. Combining the data from the model compounds has led to a better understanding of the factors that determine ^{19}F resolution. A suitable work scheme for achieving the best possible resolution for ^{19}F containing compounds is presented.

Chapter 5 investigates the combination of ^{19}F NMR and calculated data in order to assign chemical shifts to specific crystal sites[1]. The results show that by combining *ab initio* calculations with 2D NMR data confident assignment of peaks is possible.

(1) Robbins, A. J.; Ng, W. T. K.; Jochym, D.; Keal, T. W.; Clark, S. J.; Tozer, D. J.; Hodgkinson, P. *Phys. Chem. Chem. Phys.* **2007**, *9*, 2389.

Acronyms used within thesis

NMR	Nuclear magnetic resonance
SSNMR	Solid-state NMR
RF	Radio frequency
ppm	Parts per million
Hz	Hertz
B_1 field	Applied RF field
B_0 field	Static magnetic field
FWHM	Full width at half medium
T_1	Longitudinal relaxation
T_2	Transverse relaxation
$T_1\rho$	Longitudinal relaxation during spin locking
CSA	Chemical shift anisotropy
MAS	Magic angle spinning
XRPD	X-Ray powder diffraction
CW	Continuous wave
TPPM	Two pulse phase modulation
CRAMPS	Combined Rotation And Multiple Pulse Spectroscopy
REDOR	rotational echo double resonance
SPINAL-64	Small phase incremental alteration with 64 steps
CP	Cross polarisation
HH	Hartmann-Hahn
FID	Free induction decay
HHCP	Hartmann Hahn cross polarisation
ct	Contact time
VT	Variable temperature
FT	Fourier transform
EXSY	Exchange spectroscopy
NOESY	Nuclear Overhauser Effect spectroscopy
XRD	X-Ray diffraction
AZ	AstraZeneca
ms	Millisecond
OFN	Octafluoronaphthalene
ABMS	Anisotropic Bulk Magnetic Susceptibility
RR	resonance recoupling
CSD	Cambridge Structural Database
XiX	X inverse X
RFDR	Radio-Frequency-driven Dipolar Recoupling
PBE	Perdew-Burke-Ernzerhof
KT3	Keale-Tozer
DFT	Density Functional Theory
INADEQUATE	Incredible Natural Abundance Double Quantum Transfer Experiment

2 Introduction

2.1 Introduction

Nuclear magnetic resonance is the technique of measuring the NMR frequency of an atomic nucleus in a strong external magnetic field, after the excitation by electromagnetic radiation. The precession rate of the magnetisation is dependent upon the nuclear environment, therefore bonding information can be obtained from NMR experiments, to help gain structural information.

The main drawback of NMR is the inherent low sensitivity of the technique. This is due to there being a small difference in energy between the different nuclear spin states. This small energy difference results in the population of the two levels being similar, which means in effect only a fraction of the nuclei are being detected. The sensitivity is reduced even further by the fact that there is typically only a low abundance of NMR 'active' nuclei e.g.^{13}C and ^{15}N [1,2].

2.2 Principles of NMR

All NMR 'active' nuclei possess an intrinsic angular momentum, also termed spin. This spin is determined by the spin quantum number I. The $2I+1$ different spin states are distinguished by the magnetic quantum m_I, where m_I takes the values $-I$ to I in steps of one. The state of an individual nuclear spin can be represented in the so-called Dirac notation by $|I,m_I\rangle$, where I and m_I are the two quantum numbers that specify the (nuclear spin) wavefunction.

Common NMR nuclei such as ^{1}H, ^{13}C and ^{19}F have $I = \frac{1}{2}$, and so there are two possible energy states, $m_I = +\frac{1}{2}$ and $m_I = -\frac{1}{2}$. If I is greater than $\frac{1}{2}$, the nucleus is said to be quadrupolar. Quadrupolar nuclei possess, in addition to their magnetic dipole moment an electric quadruple moment. This electric quadrupolar moment is able to interact with local electric field gradients (quadrupolar interactions) which complicate the technique further. As none of the work covered in this thesis involves quadrupolar nuclei, the relevant theory will not be covered.

These spin states have the same energy (i.e. are degenerate) when outside a magnetic field. However the interaction between the nuclear magnetic moment and external magnetic fields (termed the Zeeman interaction) mean the spin states

are no longer equivalent when placed into a magnetic field. The Zeeman interaction can be expressed in quantum mechanical terms using the Hamiltonian:

$$\hat{H}_{\text{Zeeman}} = -\gamma B_0 \hat{I}_z$$

where B_0 is the external magnetic field (which has its conventional alignment along the z-axis), γ is the magnetogyric ratio for the nucleus in question, and $\hat{I}_z$ is the operator for the z-component of the nuclear spin angular momentum. It is it trivial to determine the energies of the nuclear spin states for this Hamiltonian as the $2I + 1$ spin states are already eigenfunctions of $\hat{I}_z$:

$$\hat{I}_Z \left| I, m_I \right\rangle = m_I \hbar \left| I, m_I \right\rangle$$

i.e. the z-component of the angular momentum is $m_I \hbar$. Combining the above equations gives:

$$\hat{H}_{\text{Zeeman}} \left| I, m_I \right\rangle = -\gamma \hbar B_0 m_I \left| I, m_I \right\rangle$$

i.e. the energy of a given state is

$$E(m_I) = -m_I \gamma \hbar B_0$$

At thermal equilibrium there will be more slightly more spins in the lower energy states resulting in an overall net magnetisation aligned with the applied magnetic field. The sensitivity of NMR experiments can be improved by working at higher magnetic fields since this increases the energy difference, and hence the population difference, between the spin states.

The selection rule for NMR transitions is $\Delta m_I = \pm 1$. The energy difference corresponding to these allowed transitions is:

$$\Delta E = E(m_I + 1) - E(m_I) = \hbar \gamma B_0$$

The corresponding frequency of radiation required to excite these transitions is then

$$\nu_{\text{NMR}} = \frac{\Delta E}{h} = \frac{\gamma B_0}{2\pi}$$

This radiation is in the radio-frequency (RF) region of the electromagnetic spectrum.

The exact magnetic field experienced by a nucleus in a molecule however is not exactly B_0 due to the effect of the surrounding electrons, which is termed shielding. The applied magnetic field induces "circulation" of the surrounding electrons which in turn generate small magnetic fields which oppose B_0. The nucleus is thus said to be shielded from the external field. The field experienced

by any nucleus is expressed in Equation 1, where σ represents the shielding constant.

$$B = B_0(1-\sigma)$$

Equation 1

This results in subtle variations in the NMR frequencies, making NMR a useful tool for probing local chemical environment.

The absolute shielding constant (σ) is an inconvenient measure of chemical shift, and the common method is to define the chemical shift in terms of the difference in resonance frequencies between the nucleus of interest (ν) and a reference nucleus (ν_{ref}), see Equation 2. The frequency difference is divided by ν_{ref} so that δ is a molecular property and independent of the applied magnetic field.

$$\delta = 10^6 \frac{(\nu - \nu_{ref})}{\nu_{ref}}$$

Equation 2

2.2.1 The vector model

The quantum mechanical treatment used above can be extended to situations involving more than one nuclear spin. However, full quantum mechanical treatments rapidly become complex and simpler models can often be used to understand many of the important NMR experiments. The so-called vector model is largely sufficient to explain the experiments used in this thesis. For more in-depth discussion on quantum mechanical treatments see Keeler[2].

In the vector model, rather than considering each spin as a quantum mechanical object, the magnetic fields associated with each nuclear spin are summed to give an overall magnetisation vector, and the experiment is described in terms of this overall nuclear magnetisation. This treatment is exact for experiments involving isolated $\frac{1}{2}$ spin nuclei, but is not appropriate for quadrupolar nuclei (such as ^{14}N) and can only be used with care for experiments involved coupling between nuclei. The vector model allows a visual description of the magnetisation on the application of RF pulses[3].

The vector model is often used in combination with the rotating frame of reference, in which the *x, y* axes rotate about the *z*–axis. If this rotation rate matches the frequency of the applied radio frequency, the oscillating magnetic field of the RF appears as a static field, denoted B_1, in the *xy* plane. The orientation of B_1 in the *xy* plane depends on the "phase" of the RF (*x*, *y* etc.). Similarly the rate of precession of the nuclear spin magnetisation about B_0, is now relative to the RF frequency i.e. fast time variations have been factored out.

At equilibrium the nuclear spin magnetisation will be aligned along the *z*–axis, where it will remain until the equilibrium has been disturbed via the application of resonant RF. If RF at the NMR frequency is applied, the nuclear magnetisation will rotate about B_1. (This motion is often termed "nutation"). The angle through which the magnetisation rotates is called the flip angle, β which is dependent upon the duration and power of the applied RF:

$$\beta = \gamma B_1 t_p$$

where t_p is the duration of the pulse, B_1 is the amplitude of the RF field, and β is in radians. A 90º pulse maximises the amount of magnetisation in the *xy* plane.

If the NMR frequency is significantly different from the applied RF frequency ("off resonance"), the excitation will be less effective. Using a stronger B_1 will increase the width over which the spectrum is efficiently excited. In liquid state NMR the typical frequency range for ^{1}H's on a 500 MHz spectrometer is of the order of 5 kHz. Therefore, a 90º pulse of strength $\gamma B_1 / 2\pi >> 5\text{kHz}$ will rotate the magnetisation vectors of all the ^{1}H's irrespective of the resonance frequencies. In solids the ^{1}H frequency range is typically much larger (up to 30 kHz and more) due to associated broader lines seen for solids, and so much stronger RF powers are required. The reasoning for the broad lines seen for solid-state NMR will be discussed later in this chapter and in Chapter 4.

Once the 90º pulse has been applied the magnetisation precesses about the z-- axis. As the magnetisation precesses, an induced current is produced within the receiver coil, which is termed a Free Induction Decay (FID). This overall induced signal is the sum of the response from all the individual precessing spins within the sample, each with varying frequencies due to varying chemical shifts. Fourier transformation of the time domain signal gives the NMR spectrum.

2.3 NMR relaxation

Relaxation is how a system goes towards equilibrium after an initial excitation, in this case by an applied RF pulse. The three most relevant forms of relaxation to this thesis are discussed below.

2.3.1 T_1 relaxation

T_1 relaxation[1], also termed longitudinal or spin-lattice relaxation, determines how quickly the equilibrium population of the energy levels is re-established. For a system to fully relax it is necessary to wait a period of at least $5T_1$ (at which point magnetisation has recovered by 99.33%[1]).
This is an inefficient use of time and it is common practice to use a reduced pulse delay, allowing more pulses to be applied, and improve the sensitivity. For T_1 relaxation to occur efficiently there needs to be an oscillating magnetic field around the NMR frequency. The oscillating magnetic fields are created by mobility within the molecule e.g. rotating CH_3 groups; hence, T_1 can be used to determine mobility within molecules.

For typical molecules the T_1 values for protons (^1H) tend to fall in the range of 0.5-5 s^1, and pulse delays are selected that allow only partial relaxation of the NMR signal. With only allowing partial relaxation of the NMR signal, it makes the process of performing quantitative experiments near impossible. For quantitative experiments to be performed there must be a pulse delay in excess of four times T_1 value of the system[1].

2.3.2 $T_{1\rho}$ relaxation

$T_{1\rho}$ relaxation[1] works in the same principle as T_1 relaxation, in that energy is transferred to the local spin lattice, however $T_{1\rho}$ occurs when the magnetisation is locked by the application of a suitable RF pulse. Unlike T_1 relaxation where the relaxation is sensitive to motion in the MHz region (i.e. NMR Larmor frequencies), $T_{1\rho}$ relaxation is sensitive to motion in the kHz range (i.e. nutation rates due to the spin-locking RF).

2.3.3 T_2 relaxation

T_2 relaxation[1] also termed transverse relaxation is the loss of magnetisation within the *xy* plane due to the magnetisation precessing at different frequencies. The

signal decays as the overall magnetisation is de-phased until there is no net overall signal. The experimental T_2 of a particular nucleus is directly related to the full width at half maximum (FWHM) and can be expressed by Equation 3. The relationship between T_2 and linewidths will be discussed in more detail in Chapter 4.

$$FWHM = \frac{1}{\pi T_2}$$

Equation 3

It is not possible for T_2 value to exceed that of T_1, as the T_1 determines the rate at which the magnetisation returns along the z-axis. If the motion of the sample is very rapid as in liquids T_1 and T_2 are comparable, but in solids the effective T_2 is often much shorter than T_1 by orders of magnitude.

2.4 Differences between liquids and solids

The main difference between liquid-state and solid-state NMR is the reduced motion for solids in comparison to that of liquids. In the liquid state as the molecules are tumbling at a rapid rate, every molecule is effectively identical, and there are no interactions between the molecules. As all the molecules are identical, it leads to sharp lines in the NMR spectrum, which is one reason why lines are typically well resolved in liquid state NMR.

Most of the interactions experienced by the nucleus are actually anisotropic in character, and can be described by so-called second rank tensors. In liquids, the rapid tumbling of the molecules averages out these anisotropies. However, this is not the case in solids, and so spectra acquired on powdered samples will show strong line broadenings due to the range of crystallite orientations present. The resolution in powders can be improved by rotating the sample in the magnetic field, termed magic angle spinning (MAS)[4], which will be covered in more detail in the next chapter.

There are examples of workers using single crystals in solid-state NMR[5,6], although this tend to be the exception. One reason why single crystals are not commonly used in solid-state NMR experiments, is the inherent difficulty in growing single crystals of a large enough size. The next section will discuss the most common sources of broadening, and how the effects can be reduced.

2.4.1 Chemical shift anisotropy (CSA)

Unless the nucleus is at a high symmetry site (cubic symmetry or higher), the shielding effect will vary with the orientation of the crystallite with respect to the magnetic field[7]. Each orientation will have a slightly different chemical shift value, and so this chemical shift anisotropy (CSA) will result in lines being broadened. The resulting peak shape or "powder pattern" as it is usually termed depends on the symmetry within the molecule e.g., for sites of cubic symmetry the anisotropy is zero.

The chemical shielding tensor can be described in terms of its three principal components σ_{11}, σ_{22} and σ_{33} where conventionally $\sigma_{11} \geq \sigma_{22} \geq \sigma_{33}$. For a system with cubic symmetry these three components are equal, $\sigma_{11} = \sigma_{22} = \sigma_{33} = \sigma_{iso}$, where σ_{iso} is the isotropic value of the chemical shielding, and only one narrow peak is seen (see Figure 1 a)).

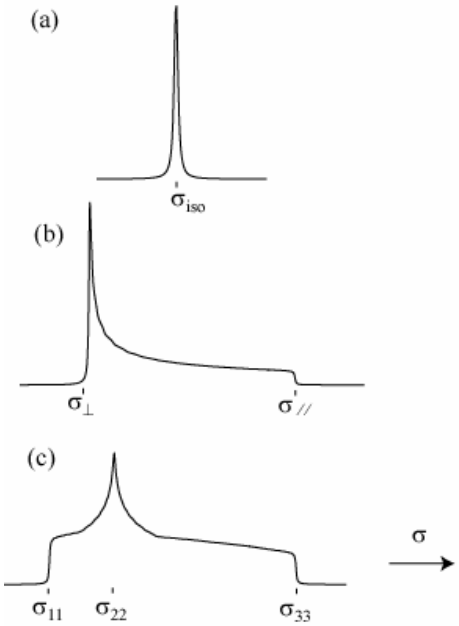

Figure 1 Schematic powder pattern caused by CSA for sites of a) cubic symmetry b) axial symmetry and c) low symmetry.

But most organic molecules do not exhibit cubic symmetry in their crystal structures, and so their orientation within the applied magnetic field will have an affect on the chemical shifts (see **Figure 1**). For an axial symmetry case (e.g. ^{13}C in $CHCl_3$), we have two principal orientations

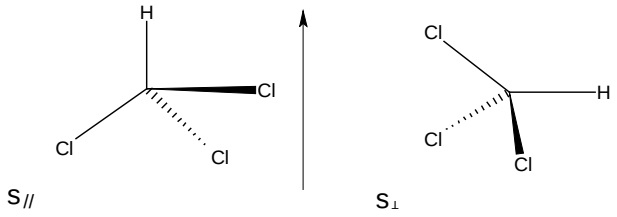

Figure 2 Axial symmetric case

$\sigma_{//}$ and $\sigma_{\perp}$ are the principal components parallel and perpendicular to the symmetry axis respectively.

In general, the chemical shift as a function of the orientation is given by

$$\delta(\theta,\varphi) = \delta_{\text{iso}} + \delta_T \left[\frac{1}{2}\left(3\cos^2\theta - 1\right) - \frac{\eta_T}{2}\sin^2\theta\cos^2\varphi \right]$$

Equation 4

where δ_{iso} is the isotropic chemical shift, δ_T is the anisotropy of the chemical shift and η_T is an asymmetry parameter which describes the deviation from axial symmetry ($\eta_T = 0$). θ and φ are polar angle describing the orientation of the CSA tensor with respect to B_0.

2.4.2 Dipolar couplings

Another feature of solid-state NMR that is not directly visible in liquids is the presence of dipolar couplings. Dipolar couplings are the through-space interaction between a pair of spins (directly analogous to the interaction of two bar magnets). The nucleus of interest has an associated magnetic field surrounding itself, this magnetic field interacts with the magnetic fields of other nuclei, and this is dipolar coupling.

The strength of the dipolar coupling depends on the internuclear distance and is inversely proportional to r^3, where r is the internuclear distance. Dipolar couplings are also dependent on the gyromagnetic ratio of the two nuclei interacting, the higher the gyromagnetic ratio, the larger the coupling. The expression for the dipolar coupling between two nuclei I and S is given by:

$$d_{12} = \frac{\hbar\mu_o}{4\pi}\frac{\gamma_I\gamma_S}{r^3}(3\cos^2\theta - 1)$$

Equation 5

where ħ is the (reduced) Planck constant, γ_I γ_S are the gyromagnetic ratios of I and S respectively, Θ is the orientation of I-S internuclear vector with respect to B_0 and μ_0 is the permeability of free space.

In solution, dipolar couplings are averaged to zero by the rapid isotropic molecular tumbling. This is not the case in solids and this is a major cause of line broadening. However, as discussed below, spinning solid samples at an angle $\theta = 54.7^o$, i.e. when $(1-3\cos^2\theta) = 0$, strongly reduces the effect of the dipolar couplings.

For low abundance nuclei such as ^{13}C and ^{15}N, the homonuclear couplings can be neglected, due to the large distances between each NMR active nucleus. Where homonuclear coupling is a major issue is for ^1H, where a high abundance and gyromagnetic ratio mean there is significant coupling present. Heteronuclear dipolar couplings, typically $^{13}C-^1H$ couplings also need to be removed, as these contribute to line broadening. These can be reduced by the application of RF irradiation at the ^1H Larmor frequency, which is termed ^1H 'decoupling', this will be discussed in more depth in the Chapter 4.

2.5 Application of SSNMR in the pharmaceutical industry

A good example on how solid state NMR differs from its solution-state counter part is differentiating polymorphs[8-10], where polymorphs can be defined as the ability of a solid material to exist in more than one crystal structure. In liquid state NMR, the spectra of two different polymorphs will be indistinguishable, due to the structural information being 'lost' on dissolution. In solid state NMR, the different arrangement of the molecules in the crystal structure results in subtle variations of the chemical shifts in the spectrum of the two polymorphs, making it possible to differentiate between them.

Polymorphism is a real problem for the pharmaceutical industry as there have been examples of where more stable polymorphs (and hence less soluble) have been discovered during the manufacture process, with the classic example being the Ritonavir case[11]. Two years into the manufacturing process a less soluble form was discovered, which resulted in the removal of the product from shelves[12]. The removal of the product from shelves meant huge financial losses and had a severe impact to the companies reputation, which highlights why polymorphism needs to be closely monitored.

Another branch of polymorphism that has applications to the pharmaceutical industry is pseudo-polymorphism, where solvents are incorporated into the crystal structure. The addition of solvents into the crystal structure will result in a totally different packing arrangement of the molecules, and hence physical properties of the solid. The most common solvate used within the pharmaceutical industry are hydrates, where water molecules are an integral part of the crystal structure. One main disadvantage of progression with a hydrate is that the solubility of the compound tends to be around 2-3 times lower[13] than the anhydrous form.

The variable solubility of polymorphs is a major concern within the pharmaceutical industry as this will lead to variation in the bioavailability, and hence efficacy of the drug. The variable solubility will also have a regulatory concern, as they will not release drugs to market until it has been shown that they can be manufactured in a robust process.

A good example of how different polymorphs behave is with diamond and graphite (they are in fact allotropes as they only involve one chemical element, carbon). Diamond is the kinetic product, that is the one produced initially, where graphite is the thermodynamic product, which is more stable. These two solid forms have significantly different physical properties, where diamond is typically used in cutting equipment, and graphite is used as a lubricant. Interestingly the statement 'diamonds are forever' can be said to be erroneous, as over time all diamonds will convert to graphite as it is the thermodynamically more stable. It is simply that this conversion happens on a much slower rate than we can envisage.

Solid-state NMR is also able to measure the number of molecules within the asymmetric unit cell. As the technique is sensitive to the local environment, if there is more than one molecule in the asymmetric unit, it results in the presence of more than one peak for each detected nucleus. It is important to state that it is not possible to assign the peaks to a molecule within the asymmetric unit from the chemical shifts alone, as it is common for the sites to have no consistent correlation between high/low frequency. However it is possible to combine solid-state NMR data with computational chemistry[8,14] to help assign the peaks, and an example will be given later in the thesis.

2.6 References

(1)Claridge, T. D. W. *High resolution NMR techniques in organic chemistry*; Pergamon, 1999.

(2)Keeler, J. *Understanding NMR spectroscopy*; Wiley, 2005.

(3)Hore, P. J. *Nuclear magnetic resonance*; Oxford science publications, 1994.

(4)Andrew, E. R.; Bradbury, A.; Eades, R. G. *Nature* 1958, *182*, 1659.

(5)Klymachyov, A. N.; Dalal, N. S. *Z Phys B: Condens Matter* 1997, *104*, 651.

(6)Griffin, R. G.; Ellett, J. D.; Mehring, M.; Bullitt, J. G.; Waugh, J. S. *J. Chem. Phys* 1972, *57*, 2147.

(7)Duer, M. *Solid-state NMR spectroscopy*; Blackwell, 2004.

(8)Harris, R. K.; Joyce, S. A.; Pickard, C. J.; Cadars, S.; Emsley, L. *Phys. Chem. Chem. Phys.* 2006, *8*, 137-143.

(9)Othman, A.; Evans, J. S. O.; Evans, I. R.; Harris, R. K. *J. Pharm. Sci.* 2007, *32*, 1796.

(10) Tishmack, P. A.; Bugay, D. E.; Byrn, S. R. *J. Pharm. Sci.* 2002, *92*, 441.

(11) Bauer, J.; Spanton, S.; Henry, R.; Quick, J.; Dziki, W.; Porter, W.; Morris, J. *Pharm. Res.* 2001, *18*, 859.

(12) Miller, J. M.; Collman, B. M.; Greene, L. R. *Pharm. Dev. Tec.* 2005, *10*, 291.

(13) Pudipeddi, M.; Serajuddin, A. T. M. *J. Pharm. Sci.* 2005, *95*, 929.

(14) Robbins, A. J.; Ng, W. T. K.; Jochym, D.; Keal, T. W.; Clark, S. J.; Tozer, D. J.; Hodgkinson, P. *Phys. Chem. Chem. Phys.* 2007, *9*, 2389.

3 Experimental

3.1 Introduction

This chapter describes the basic techniques that have been used within this thesis The majority of the work was performed on a Varian InfinityPlus spectrometer, operating at a nominal ^{1}H frequency of 500 MHz (11.7 T). The remaining work involved either a Varian Inova operating at a ^{1}H frequency of 300 MHz (7.05 T) or a Chemagnetics CMX spectrometer operating at a ^{1}H frequency of 200 MHz (4.7 T).

3.2 Probes

Three probes have been used. For high resolution work where fast MAS was required, a 2.5 mm HX probe was used. The majority of the work performed with this probe was investigating linewidths for systems with a high ^{19}F content, with the nominal ^{1}H channel tuned to the ^{19}F frequency (470 MHz). For systems dilute in ^{19}F, it was necessary to move to the 4 mm HFX probe where the spin rate was reduced due to larger rotor diameter. It was now possible to acquire on ^{19}F while simultaneously applying ^{1}H decoupling. Experimentally this was more complicated due to the similarity in the frequencies of ^{19}F and ^{1}H (~9% difference) meaning that the two channels had to be isolated fully using the probe's trap circuit.

The 2.5 mm HX probe was also used in the indirect detection experiments as fast MAS was required to achieve higher resolution for the ^{1}H channel. (Initial work in optimising the cross polarisation step was performed on a 3.2 mm HXY probe)

3.3 Magic angle spinning (MAS)

Magic Angle Spinning (MAS)[1,2] is an essential tool in solid-state NMR for reducing spectral linewidths and hence improving resolution. As mentioned in Chapter 1, the three main interactions that lead to broadenings of lines in solid-state NMR are dipolar couplings, chemical shift anisotropy and quadrupolar couplings. All three interactions are sensitive to their orientation within the applied magnetic field, and contain anisotropic terms that vary as $(3\cos^2\theta-1)/2$ where θ is the angle between the tensor principal axis and the magnetic field (e.g. **Equation 5**). These terms are zero when $\theta = 54.7^{o}$, the "magic angle"[2,3].

In MAS, the sample is spun in a rotor oriented at the magic angle with respect to the magnetic field, $\beta = 54.7^{o}$ in the diagram below. If the spinning rate is larger than the magnitude of the anisotropic interaction, then the interaction is averaged out by the spinning and a single line (the

"centreband") is observed. At slower spinning rates, "spinning sidebands" are observed which are separated from the centreband by multiples of the spinning rate. At slow spinning rates, the envelope of the spinning sidebands approximates to the shape of the powder pattern observed for static samples (see **Figure 1**).

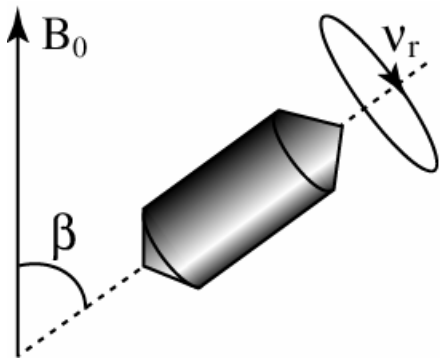

Figure 3 Schematic diagram representing magic angle spinning.

Dipolar couplings can not be totally removed as spin rates would need to be greater than the static band width, which is generally tens of kHz, which is not physically possible with current technology. The resolution can be improved further with the application of suitable ^{1}H decoupling, (see section 5.7) such as TPPM[4] in the heteronuclear case.

Chemical shift anisotropies are relatively easily averaged out by magic angle spinning. The spinning sidebands are sharp and the spinning rate only needs to be slightly greater than the anisotropy for the CSA to be fully averaged out.

The MAS rate of a sample can be controlled by applying varying air pressures to the probe. The maximum spin rate possible is determined by the diameter of the rotor being used; with smaller rotors permitting faster spin rates. To reduce friction the rotors sits on a bed of air, with the pressure of the air increased for faster MAS to hold the rotor more securely. This is termed the "bearing pressure" at least for Varian spectrometers, while the air pressure used to rotate the sample is called the "drive pressure". By combining suitable bearing and drive pressures, the MAS rate can be varied over a significant range, depending on the rotor diameter being used.

3.3.1 Setting the angle

To ensure optimum MAS averaging, it is essential that the spinning angle is accurately set. The traditional method of setting the angle uses a sample of potassium bromide (KBr) and acquires the ^{79}Br signal. KBr is a convenient angle-setting sample as the frequency of ^{79}Br is similar to that of ^{13}C meaning little tuning variation is required. ^{79}Br is a quadrupolar nucleus and the first order quadrupolar coupling on the satellite transition gives rise to good set of spinning side bands. KBr

is also a suitable sample for setting the angle as it has a short T_1 meaning rapid pulses can be applied, and no decoupling needs to be applied. As such, a suitable signal can be acquired in a matter of seconds.

The angle is optimised by measuring the number of rotational echoes in the FID; the longer the train of echoes, the closer the sample is to 'being on angle'. These rotational echoes in the FID relate to the number of spinning side bands in the spectrum. The angle should be checked at regular intervals, especially after any variable temperature experiments. In general, samples with larger anisotropies are more sensitive to variations from the magic angle.

3.4 Shimming

Even though care is taken to make the applied B_o as homogeneous as possible, there are still imperfections present. These imperfections need to be reduced, as this would lead to broadenings of the lines due to varying NMR frequencies at different positions in the rotor. To compensate for these inhomogeneities of the B_o field, a series of shim coils are located around the sample. These coils have electric currents passing through which can be varied. For each probe, a set shim file is used where the current is determined for each shim coil. These shim parameters are determined manually for all new probes on installation, and saved once optimum conditions found.

3.5 Referencing

To ensure that measured chemical shifts are comparable for each spectrometer it is necessary to reference the spectrum of each nucleus detected against a known standard. The referencing needs to be performed at regular intervals to ensure that any drift from the original magnetic field is allowed for. The standards used are summarised in **Table 1**.

Nucleus	Reference standard	Chemical shift / ppm
^{1}H	PDMSO	0 w.r.t. TMS
^{19}F	Teflon	-122.8 w.r.t. $CFCl_3$
^{15}N	Asparagine	-287.0 (high frequency peak) w.r.t. CH_3NO_2
^{13}C	Adamantane	38.4 (high frequency peak) w.r.t. TMS

Table 1 Referencing standards for nuclei detected

3.6 Solid-state NMR experiments

3.6.1 Pulse and acquire

For nuclei with a high abundance and high gyromagnetic ratio, e.g. ^{19}F and ^{1}H, it is possible to detect the NMR signal directly by applying a 90º pulse then detecting the oscillating NMR frequency (see **Figure 4**). As the T_1 values for these nuclei are typically short and only a small number of acquisitions are required due to their high NMR sensitivity it is feasible to use a pulse delay in excess of five times that of the T_1 to ensure full relaxation of the system. As the systems have been allowed to fully relax it is also possible to perform quantitative experiments more routinely for pulse and acquire experiments, particularly ^{19}F due to the better resolution compared to ^{1}H. When working with systems with long relaxation times it is sufficient to set the pulse delay to three times that of T_1 of the system (~95% of full relaxation) and pulses should be between 80-90º to maximise sensitivity. By not allowing full relaxation performing quantifiable experiments becomes more challenging.

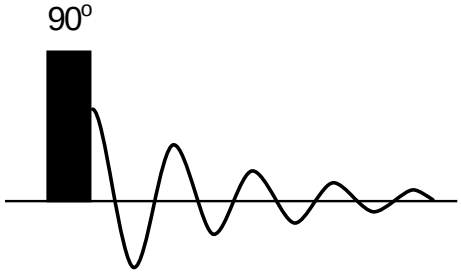

Figure 4 Schematic diagram representing the pulse and acquire experiment, the 90º pulse is used to 'excite' magnetisation

There are times when the samples T_1 are much too long to allow for full relaxation. Sensitivity in experiments where multiple scans are accumulated can be optimised by using a tip angle of less than 90º termed the 'Ernst angle', α_e. This is related to the T_1 of the system and the pulse delay by the equation below:

$$\cos\alpha_e = e^{-t_r/T_1}$$

where t_r is the pulse delay.

For maximum signal in a single scan, the excitation pulse should be calibrated so that it rotates the magnetisation by 90º. To find an accurate 90º pulse the pulse length is increased in small increments until there is a null in the detected signal. This null in signal relates to the 180º pulse, which can then be used to calculate the 90º pulse length. The 90° pulse calibration is performed this way, as it is easier to detect a null signal as opposed locating a maximum. It is difficult to locate a maximum especially for ^{1}H signal due to the associated background signal. Calibration

experiments are a good check to see that the probe is tuned sufficiently, as the 90° will vary significantly from previous experiments if it has not been tuned accurately.

To calibrate the 90° pulse for ^{13}C, adamantane is normally used due to its narrow lines and short T_1 value, meaning short pulse delays can be used. Once the experiment has been fully optimised, the adamantane peaks can also be used as a reference for the chemical shift for ^{13}C, due to the narrow linewidths.

3.7 Cross polarisation

For nuclei that have a low natural abundance and low gyromagnetic ratio e.g. ^{13}C (1.1%) and ^{15}N (0.37%) it is not feasible to detect the nuclei with a standard pulse-and-acquire experiment. The routine method of detecting low sensitivity nuclei in organic molecules is CP[5], where the magnetisation is transferred from the ^{1}H onto the nucleus of interest (see **Figure 5**). This leads to a theoretical increase in sensitivity proportional to the ratio of the gyromagnetic ratio, for ^{13}C this is four times, and ten times for ^{15}N. Also the pulse delay is now governed by the T_1 of the ^{1}H which is typically reduced by the ratio of the gyromagnetic ratios. This significantly reduces the pulse delay and hence the overall signal-to-noise ratio achievable in a given time, i.e. the sensitivity.

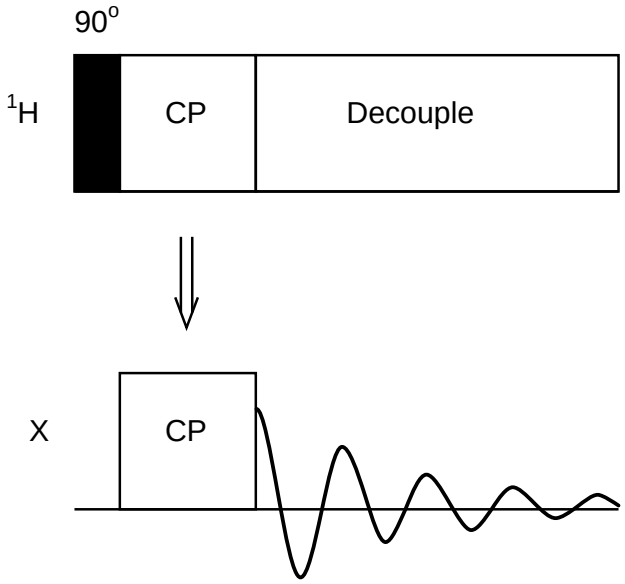

Figure 5 Pulse sequence for the CP process. The initial 90° pulse excites the magnetisation on ^{1}H's and a spin locking pulse is then applied onto both channels simultaneously.

Traditional CP experiments are performed at relatively slow MAS rates (~5 kHz). The optimum CP parameters can be found by incrementing the power on either the proton or heteronuclear channel, termed the spin locking pulse. Typically the power is arrayed on the ^{1}H channel due to the lower associated powers, until a maximum in the signal is seen. The term spin locking is used, as

when the pulse is applied it will hold the magnetisation of that specific nucleus along a particular axis in the rotating frame model. If the precession rates of the two nuclei are equivalent which is termed as the Hartmann-Hahn matching condition (HH)[5], this then allows magnetisation transfer between the two nuclei to occur via dipolar couplings.

At faster MAS (>10 kHz) the Hartmann-Hahn condition breaks down into a series of side bands that are separated from the HH matching condition by a multiple of the MAS rate. This is termed as fast MAS, which is covered in more detail in Chapter 3. Due to the narrow matching conditions finer increments in RF should be used in the optimisation of CP to ensure maximum signal to noise. It is also advised that a ramp is used for one of the spin locking pulses to make the experiment more robust.

By varying the initial ^{1}H pulse within the CP experiment the ^{1}H pulse length can be determined more accurately, as mentioned in the previous section it can be difficult to determine an accurate ^{1}H 90º due to the background signal of the probe. The optimum ^{1}H 90º corresponds to when the ^{13}C signal is greatest.

3.8 Spin echoes

The spin echo experiment allows the "T_2" for a particular system to be measured and this will give an idea of the homogeneous linewidth for a particular system (see section 5.2 for a more in-depth discussion on homogeneous linewidth). The spin echo experiment is able to refocus this inhomogeneous contribution, allowing the T_2 value to be measured from the decay of the signal.

An initial 90º pulse places the magnetisation onto the *xy* plane, where it precesses about the *z*-axis, where the magnetisation will dephase due to homogeneous and inhomogeneous contributions. After time τ a 180º pulse is applied which will invert the magnetisation, and the magnetisation will continue to precess. After time τ any inhomogeneous contributions will be refocused, making it possible to measure T_2 values which correspond to the homogeneous linewidths (see **Figure 6**). A schematic representation of the magnetisation during the spin echo experiment is given in **Figure 7**.

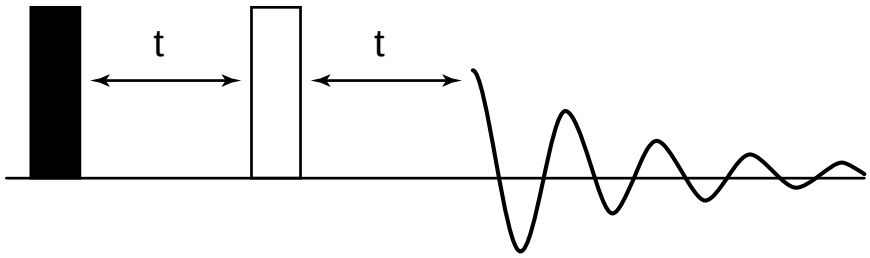

Figure 6 Diagrammatic representation of the spin echo experiment. An initial 90º excites the system, and the magnetisation precesses in the xy plane for time τ. The 180 pulse refocuses any inhomogeneity/chemical shifts at time 2τ.

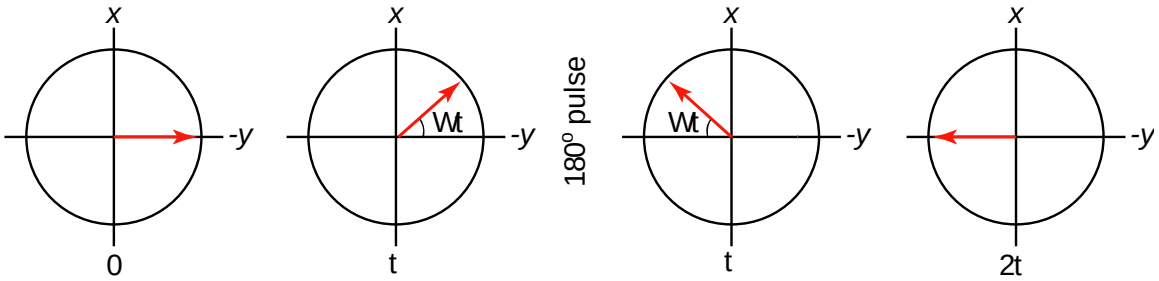

Figure 7 Schematic diagram representing magnetisation during spin echo experiment. Magnetisation precesses due to chemical shifts, inhomogeneous contributions etc. After time τ the magnetisation is 'flipped' with a 180º pulse. The shifts/inhomogeneous contributions are now refocused during the second τ interval[6].

If the experiment is performed along with MAS (which it usually is to improve resolution) then the spin echo delay,τ should be an integral number of rotor periods, so that any rotor echoes induced are refocused.

3.9 Inversion and saturation recovery

To measure T_1 for a given system, a common technique is inversion recovery, which measures the time taken for the system of interest to return to its thermal equilibrium after the spin distribution has been inverted. The experiment is a simple two pulse experiment (see **Figure 8**), where the magnetisation is inverted with a 180º pulse, with the magnetisation aligned along the -*z* axis. The magnetisation will gradually 'shrink' back towards the *x*-*y* plane, where after sufficient time the magnetisation will have fully recovered along +*z* axis. The rate of recovery is determined by the T_1 for that particular nucleus. As it is not possible to detect signal aligned along the *z* axis, it is required to place the magnetisation into the *xy* plane by the application of a 90º pulse after a suitable period,τ, where the recovery of magnetisation can be detected.

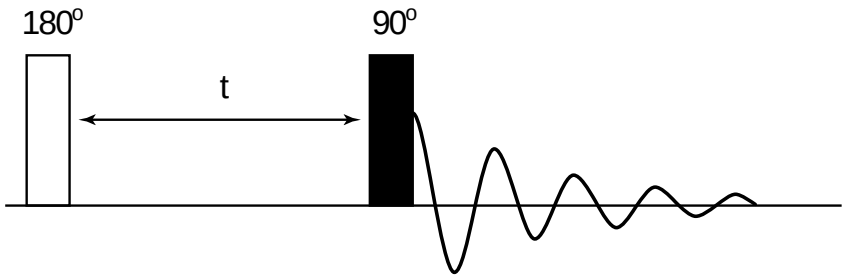

Figure 8 Pulse sequence of the inversion recovery experiment. An initial 180° pulse inverts the signal, and a time delay of τ is allowed before 90° pulse transfers magnetisation into the *xy* plane to be detected.

When τ is zero, there has been no relaxation within the system and the peak will have a full intensity ($-M_0$), with but is inverted, using conventional phasing for the system. As the value of τ is extended, the relaxation of the spins and hence magnetisation, M_t can be measured, until equilibrium has been reached ($\tau > 5T_1$) resulting in the maximum positive signal. The recovery of the magnetisation follows the following equation.

$$M_t = M_o\left(1 - 2e^{(-\tau/T_1)}\right)$$

Equation 6

The main difficulty with this method is that the system has to be fully relaxed before the magnetisation can be inverted. For high sensitivity nuclei, such as ^{19}F and ^{1}H this is not a problem. It becomes more of a problem for the less sensitive nuclei, where more acquisitions are required and longer T_1 values result in longer pulse delays. In some cases, it is not feasible to measure T_1 with the inversion method and another technique needs to be used.

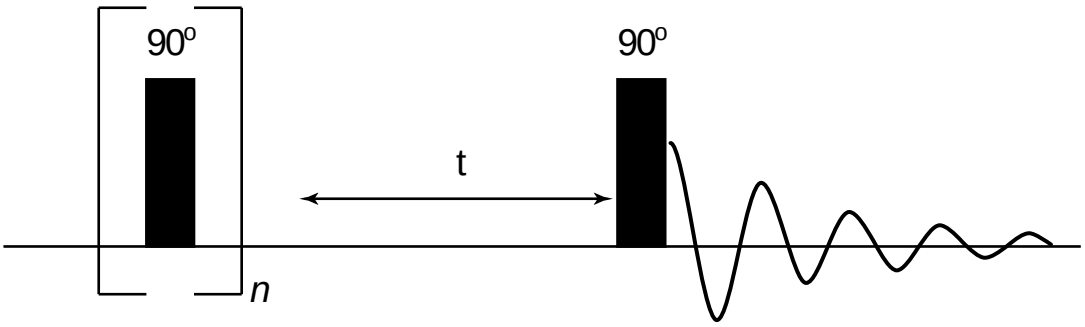

Figure 9 Pulse sequence for the saturation recovery experiment. An initial train of 90° pulses saturates the magnetisation. Magnetisation is allowed to recover over time τ, before the magnetisation is flipped into the *xy* plane by a 90° pulse.

A common solution in solid-state experiments, is the saturation recovery experiment. The sequence initially destroys the magnetisation by saturating the system by a series of 90° pulses. As the 90° pulses are applied, the delay between them is insufficient for T_1 relaxation to occur, and the

magnetisation will be rotated into all possible directions. This results in a zero net magnetisation, due to the two possible energy levels being equally populated with spins.

The magnetisation is then allowed to recover towards equilibrium during time τ. The magnetisation for each τ value is measured by the application of a 90º pulse, which places the magnetisation into the *xy* plane, where it can be detected.

Unlike the inversion recovery experiment where the system requires being fully relaxed before the second acquisition can be performed, the saturation pulse can be started straight after the FID has been fully acquired.

3.10 EXSY/NOESY

The exchange spectroscopy (EXSY)[7] experiment and the nuclear Overhauser effect spectroscopy (NOESY) experiment are both examples of 2D experiments. The only difference between the two experiments is the mechanism of the transfer of magnetisation. The NOESY experiment is predominantly used in liquid state NMR, as the nuclear Overhauser effect (NOE) (which is a cross relaxation process) involves rapid motions, which are not commonly observed in solids. Both EXSY and NOESY experiments are 2D correlation experiments, which correlate NMR frequencies in the t_1 and t_2 periods.

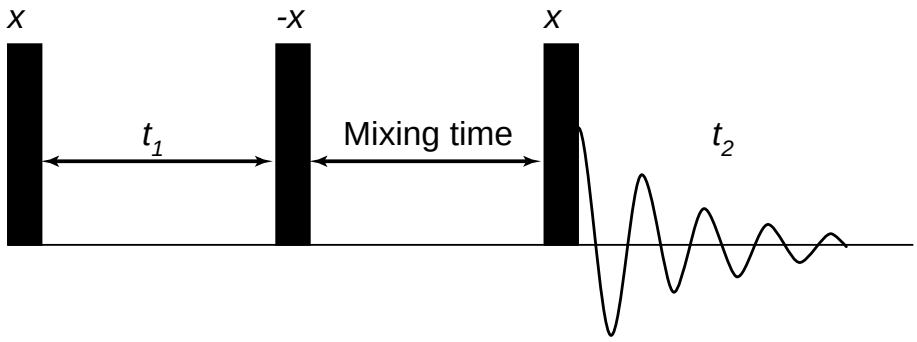

Figure 10 Pulse sequence for EXSY/NOESY experiment.

The pulse sequence is shown in **Figure 10**. Excitation of the magnetisation is performed by an initial 90º pulse, where the magnetisation it then allowed to evolve during time t_1. Another 90º is applied which rotates one component of the magnetisation onto the *z* axis, where it is 'stored' for a mixing time where molecular reorientation may occur. Finally, the magnetisation is converted into an observable signal via another 90º. The signal is Fourier transformed in both the t_1 and t_2 dimension to give a 2D spectrum, where any correlation between nuclei is represented by a series of off diagonal peaks.

3.11 Setup of sample dependent conditions

Unlike the previous experimental parameters, such as pulse length calibrations, which can be applied to all systems containing the relevant nucleus, other settings are sample dependent.

3.11.1 Recycle delay

This is the time between the end of the FID in one acquisition and the next applied RF pulse. The recycle delay is dependent upon the T_1 of the system, and as described previously (see section 2.3) the T_1 relaxation rate is determined by the motion within the system[8]. It is important to choose a sufficient recycle delay as this determines the sensitivity of the experiment. If a pulse delay is too short, the magnetisation becomes saturated and no NMR signal can be detected, resulting in a poor signal-to-noise ratio. If the pulse delay is too long it simply means that less RF pulses can be applied to create excitation in a given time, resulting in a reduced signal-to-noise ratio due to loss of acquisitions.

The pulse delay can be determined by the T_1 of the system and in general, typical pulse delays of around 4-5 times of the T_1 of the system are used for quantitative experiments. However, as highlighted in section 2.5 it is possible to pulse more rapidly if the 90º pulse is adjusted accordingly. For more complicated pulse sequences, e.g. spin echoes, it is essential that the system is fully relaxed before the next RF excitation pulse is applied. Generally, the pulse delay is determined by incrementing the pulse delay in a series of experiments, where the intensity of the signal is compared for each experiment. As the pulse delay is extended the signal should continually rise until a plateau is reached, this is where the system has fully relaxed prior to the next pulse being applied. For optimum signal-to-noise in simple pulse-and-acquire experiments, a relative intensity of 70% to that to when the system is fully relaxed is used, this roughly equates to the pulse delay being 1.2 times that of the T_1 of the system.

3.11.2 Contact time

The contact time in the cross polarisation experiment is the time that the spin locking pulses on the two nuclei are applied simultaneously. For weaker couplings, such as nuclei with low gyromagnetic ratios or spins that are relatively far away, long contact times are required for the cross-polarisation signal to build up. However, the signal decays at longer contact times decays due to $T_{1\rho}$ relaxation, as shown in **Figure 11**. The optimum contact time can be found by simply incrementing the contact time for a particular system.

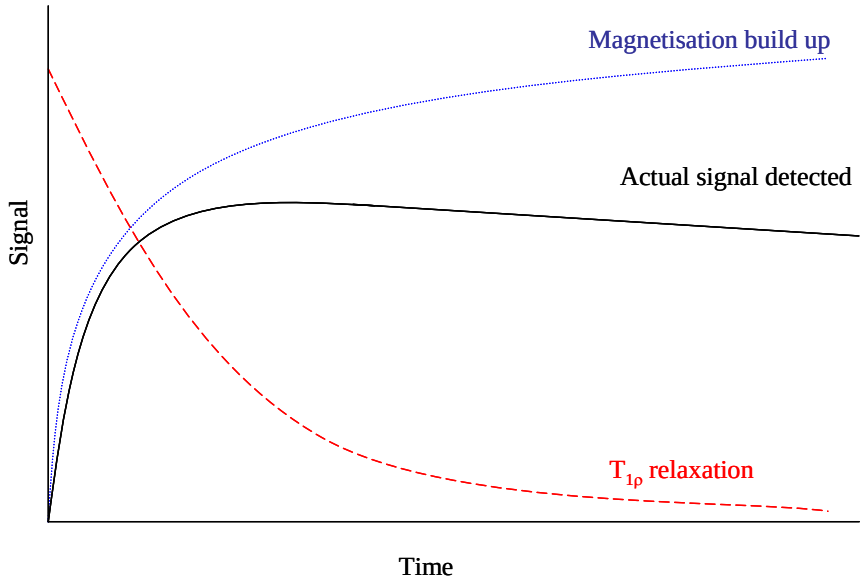

Figure 11 Diagram highlighting the two conflicting processes present during CP. The blue line represents the build up of magnetisation due to cross-polarisation, while the red represent the loss of signal due to $T_{1\rho}$.

Another factor to be considered for CP is that the optimum conditions depend on the nature of the chemical sites. One such example is comparing a $^{13}CH_2$ group to a quaternary ^{13}C, as the CH_2 group will have two local ^{1}H's for magnetisation to be transferred, meaning short contact times are normally optimal. As quaternary carbons have no local ^{1}H, and hence are weakly coupled, they generally need longer contact times. In contrast to what you would expect ^{13}C in a CH_2 group will cross polarise faster than one in a CH_3 group. This is due to the rapid rotational diffusion about the carbon bond, which motionally averages (reduces) the dipolar couplings.

Because the cross-polarisation signals build up at different rates, peaks intensities in CP are not quantitative. In order to perform quantitative experiments a calibration experiment needs to be performed, which is relatively time consuming[9].

3.12 Decoupling

Fast MAS alone is not sufficient to remove all of the dipolar couplings between NMR active nuclei in solids, leading to the broadening of the lines. The main limitation of MAS is that the maximum rotation rates achievable with current technology are orders of magnitude lower than rates of molecular tumbling in liquids.

A method to reduce linewidths which is commonly used in liquid state NMR is the application of constant irradiation on the ^{1}H channel with a RF pulse while detecting on the X channel, termed

decoupling[10]. This results in the couplings to the ^{1}H spins magnetisation being effectively 'averaged out' by rapid flipping of the ^{1}H spins.

Even on the application of full power ^{1}H decoupling in solids there is still a significant contribution to the overall linewidth due to the dipolar couplings. This is due to the maximum decoupling power being limited by the probes specifications, which typically means a ^{1}H precession rate being around 100 kHz for small diameter rotors. This is 'faster' than MAS but still orders of magnitude smaller than the motion in liquids.

The decoupling at faster MAS rates can be improved on the application of more complex decoupling sequences in comparison to the continuous wave (CW) decoupling. These decoupling sequences are able to improve resolution even further by using the same power for the ^{1}H decoupling, by switching the proton phase at regular intervals[4,11-13]. The applications of decoupling are covered in more detail in Chapter 4.

3.13 Calibration of variable temperature experiments

It is possible to perform NMR experiments at variable temperatures (VT). The range of temperatures that can be used varies from probe to probe, and should always be consulted before performing VT experiments.

For performing work below room temperature, nitrogen gas should be used as using compressed air brings about the possibility of freezing any moisture present. The nitrogen gas can be cooled by passing it through a copper coil, which is placed within a dewar of liquid nitrogen. The temperature is controlled by the spectrometer, which heats the 'cooled' gas to the required temperature. Work above room temperature uses compressed air, except for temperatures above about 100 °C for which nitrogen gas is used again to prevent damage of the probe.

In order to get meaningful results the variable temperature experiments need to be calibrated, as the temperature sensor is a long way from the sample. The actual temperature needs to be calculated for a series of spinning speeds and temperatures to get a calibration plot, which can then be used to calculate the actual temperature within the rotor for a combination of MAS rates and temperatures.

In order to calibrate the temperature of the probe it is necessary to have a suitable compound that is sensitive to any temperature variation, and can be used over a wide temperature range. A common choice is lead nitrate ($Pb(NO_3)_2$)[14] where the ^{207}Pb chemical shift is temperature sensitive which have a linear dependence with temperature. The problem is that this gives a relative measurement. In order to get an absolute temperature reading a sample with two signals where the difference between the two signals is sensitive to the temperature is required. Liquid methanol is commonly

used with the difference between the two proton peaks giving an absolute temperature calibration. This can then be applied to the ^{207}Pb chemical shifts.

The shape of the ^{207}Pb peak also highlights any temperature gradient present within the rotor. For close to ambient temperature the peak is relatively sharp indicating a homogeneous temperature throughout the rotor. As the temperature variation from room temperature increases, the temperature gradient through the rotor becomes more extreme, represented by the peak having a significant 'tail'. Once the temperature profile of the probe has been fully calibrated, it is possible to relate the set temperature of the experiment to the actual temperature within the rotor.

3.14 X-ray diffraction

A very powerful tool in determining the crystal structure is single crystal X-ray diffraction (XRD), where a single crystal of the sample of interest is placed within a collimated X-ray beam. The X-rays are reflected from evenly spaced planes of the crystal, producing a diffraction pattern.
The crystal structure can then be determined from the resulting diffractogram.

One major problem with the technique is the difficulty in producing crystals of high enough quality and of a suitable size (order of mm's). Due to the inherent problem of growing crystals of sufficient size in all three dimensions, an alternative method has been developed where the diffractograms of powders are measured.

When it is not possible to grow crystals of suitable quality, powder XRD can be used for rapid crystalline checks, such as polymorphism. The main disadvantage of powder XRD in comparison to single crystal XRD is the loss of information. For single crystal work only one crystal orientation is present, resulting in a pattern of spots spread over a 2D diffractogram. This diffractogram can be used to determine the crystal structure relatively straightforwardly. Due to powder XRD having all possible crystal orientations present the information is now collapsed into a 1D diffractogram. It is complicated to solve the crystal structure from the powder XRD diffractogram alone as there are so many degrees of freedom present. However powder XRD can be used as a quick method to test crystallinity of a sample, and measure crystal information, e.g. unit cell size. As dicussed in chapter 5 the powder XRD data can also be combined with complementary techniques, such as solid-state NMR to aid the crystal structure determination of an unknown compound.

3.15 References

(1) Gan, Z. *J. Am. Chem. Soc.* **1992**, *114*, 8307.

(2) Andrew, E. R.; Bradbury, A.; Eades, R. G. *Nature* **1958**, *182*, 1659.

(3) Pines, A.; Gibby, M. G.; Waugh, J. S. *Journal of Chemical Physics* **1973**, *59*, 569-590.

(4) Bennett, A. E.; Rienstra, C. M.; Auger, M.; Lakshmi, K. V.; Griffin, R. G. *J. Chem. Phys.* **1995**, *103*, 6951-6958.

(5) Hartmann, S. R.; Hahn, E. L. *Phys. Rev.* **1962**, *128*, 2042-2053.

(6) Keeler, J. *Understanding NMR spectroscopy*; Wiley, **2005**.

(7) Jeener, J.; Meier, B. H.; Bachmann, P.; Ernst, R. R. *J. Chem. Phys* **1979**, *71*, 4546.

(8) Duer, M. *Solid-state NMR spectroscopy*; Blackwell, **2004**.

(9) Apperley, D. C.; Harris, R. K.; Larsson, T.; Malmstrom, T. *J. Pharm. Sci.* **2003**, *92*, 2487.

(10) Hoffmann, A.; Foren, S. *Nucl. Magn. Reson. Spec.* **1966**, *1*, 15.

(11) Hodgkinson, P. *Prog. Nucl. Magn. Reson. Spectrosc.* **2005**, *46*, 197.

(12) Brauniger, T.; Wormald, P.; Hodgkinson, P. *Monatsh. Chem.* **2002**, *133*, 1549.

(13) Ernst, M.; Samoson, A.; Meier, B. *J. Magn. Reson.* **2003**, *163*, 332-339.

(14) Bielecki, A.; Burum, D. P. *J. Magn. Reson. A* **1995**, *116*, 215.

4 Indirect detection of ^{15}N via ^{1}H

4.1 Introduction

The receptivity of an NMR nucleus is defined as being the product of a frequency related term (i.e. higher NMR frequencies are detected more efficiently) and natural abundance of the NMR active nucleus. Due to the low overall receptivity of ^{15}N (3.85×10^{-6} with respect to ^{1}H), and the large number of biologically and pharmaceutically active compounds containing nitrogen, there is great interest into trying to improve the quality of ^{15}N spectra in solid-state NMR. In conjunction with my industrial supervisor (AstraZeneca), we are investigating methods of improving ^{15}N sensitivity, principally via indirect detection, that is acquiring the ^{15}N spectra indirectly via ^{1}H.

It has recently been suggested that dilute spins such as ^{13}C and ^{15}N could be efficiently detected indirectly in solid-state NMR. The advantage of detecting the signal indirectly is that it is much more sensitive to detect on ^{1}H compared to ^{15}N, due to the higher NMR frequency of ^{1}H. This is a routine method for detection of insensitive nuclei (such as ^{15}N) in solution state NMR[1]. This is more challenging for solid-state NMR due to the broad ^{1}H lines due to the dipolar coupling network, which results in the loss in sensitivity making it less effective. The increasing MAS rates now available may sufficiently reduce the ^{1}H linewidths to make the technique competitive. In principle ^{1}H resolution could be further improved using combined rotation and multiple pulse spectroscopy (CRAMPS)[2-4]. However, these experiments are technically complex and demanding, particularly if ^{1}H is being detected in the direct dimension, as so we focus here on line-narrowing via fast MAS.

Previous workers[5-11] have used indirect detection to detect insensitive nuclei such as ^{15}N and ^{13}C. Schnell and co-workers[7] reporting sensitivity improvements of a factor of 6–8 using indirect direction of ^{15}N. Note that in this case, one of the polarisation transfer steps used a REDOR-based sequence, as they were interested in quantifying the ^{15}N,^{1}H dipolar couplings. Ishii *et al*[9] reporting a sensitivity improvement of 1.6 to 3.3 for ^{13}C , while other workers have reported more modest sensitivity improvements (2–3 times)[5,6,10] for ^{15}N detection. (We would expect an advantage of about 2.5 for indirect detection of ^{15}N over ^{13}C due to the lower gyromagnetic ratio of ^{15}N.) The sensitivity improvement in Ref 9, was dependent on whether the ^{13}C site was protonated, with the lower sensitivity improvement seen for the non-protonated sites. The non-protonated sites had a lower sensitivity improvement due to weaker ^{1}H-^{13}C dipolar couplings, making the transfer of magnetisation less efficient. As the fundamental step in indirect detection is the transfer of magnetisation between ^{15}N and ^{1}H via cross polarisation (CP), it is important that this step is as efficient as possible. Any improvement in the cross polarisation step (CP) will in effect be squared.

Previous workers have also used REDOR pulse sequences within the indirect detection method[12] to measure ^{15}N-^{1}H bond lengths. To date REDOR-based sequences have generally been used in experiments to quantify ^{15}N–^{1}H couplings, with CP being used for the initial transfer. If the REDOR sequence was seen as a more efficient method to transfer the magnetisation then it would be expected that the workers would have used the REDOR sequence for both magnetisation transfer steps.

4.2 Hartmann-Hahn Cross polarisation (HHCP)

The standard method of polarisation transfer in solids is Hartmann-Hahn cross polarisation (HHCP)[13] (see section 3.7). In this technique, resonant RF fields are applied to two nuclei simultaneously. The rate of precession of the magnetisation of a given nucleus is given by $\eta_I = \gamma_I \mathrm{B}_{1I}$, where γ_I, is the gyromagnetic ratio of the nucleus and B_{1I} is the magnitude of the oscillating magnetic field. If these precession rates are matched for the two nuclei, I and S, (see **Equation 7**), then magnetisation can be transferred between I and S via any dipolar coupling between them.

$$\gamma_I \mathrm{B}_{1I} = \gamma_S \mathrm{B}_{1S}$$

Equation 7

In the case of ^{1}H–^{15}N cross-polarisation, initial ^{1}H magnetisation is transferred onto ^{15}N (prior to detection on ^{15}N). There are a couple of important advantages to this method compared to acquiring a signal directly from the natural ^{15}N magnetisation. Because the nuclear magnetisation is proportional to gyromagnetic ratio, the ^{1}H magnetisation is ~10 times larger than that of ^{15}N $(\gamma(^{1}H)/\gamma(^{15}N) \sim 10)$, hence the ^{15}N signal after cross-polarisation from ^{1}H is ~10 times larger than the "direct polarisation" signal. Another important advantage of the CP experiment, is that the time between signal acquisitions is now determined by the relaxation time (T_1) of the protons. These are much shorter (typically by a factor of ~10 again), allowing many more acquisitions to be made within a given time. As a result, cross-polarisation dramatically increases the sensitivity (S/N ratio) of solid-state ^{15}N spectra.

CP is routinely performed at low MAS rates, with as much sample as possible as this will increase the sensitivity. At low MAS rates the Hartman-Hahn matching profile is relatively insensitive to any variation in spinning rates and the Hartman Hahn matching condition is at the centre of the band ($\eta_I = \eta_S$) (see **Figure 12**).

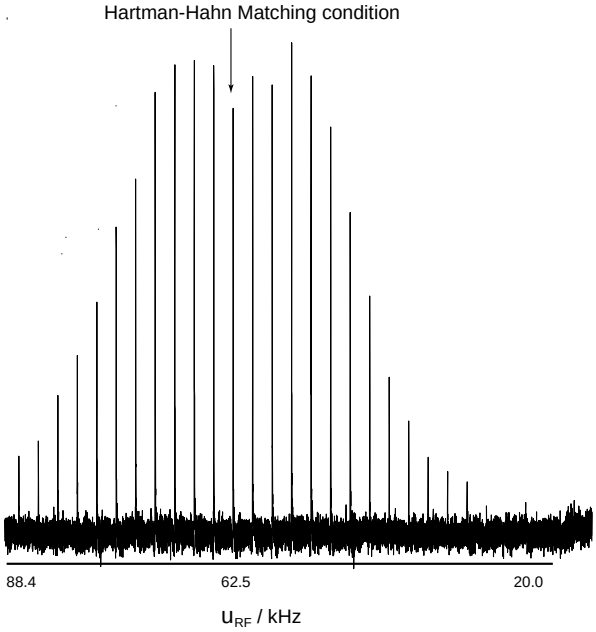

Figure 12 Experimental matching profile for ^{15}N labelled alanine as a function of varying the I spin (^{1}H) amplitude at low spinning speed (5 kHz). The intensity is maximum when RF amplitudes on I and S are matched. The experiment used a 4μs 90º pulse on ^{1}H, with a contact time of 1ms and pulse delay of 5 seconds. ^{1}H decoupling was applied with a power of 62.5 kHz.

Fast MAS is required when performing indirect detection, so that the ^{1}H lines are sufficiently resolved by reducing the ^{1}H-^{1}H dipolar couplings. If indirect detection is performed at modest MAS rates (~ 5 kHz) then any sensitivity improvement is compromised by the increase in the ^{1}H linewidth. However, Hartmann-Hahn matching becomes more complex as the spinning speed of the sample is increased. The matching condition breaks down into a series of relatively sharp peaks, separated from the original matching condition by ± 1 or 2 times that of the spinning frequency[14], where the sideband nutation rate can be defined by $\upsilon_S = \upsilon_I + n\upsilon_r$, where υ_I is the ^{1}H nutation frequency and υ_r is the MAS rate (see **Figure 13**). It is important to note that if the original matching condition for modest MAS is used very little signal will be detected due to inefficient CP, as shown in **Figure 13**.

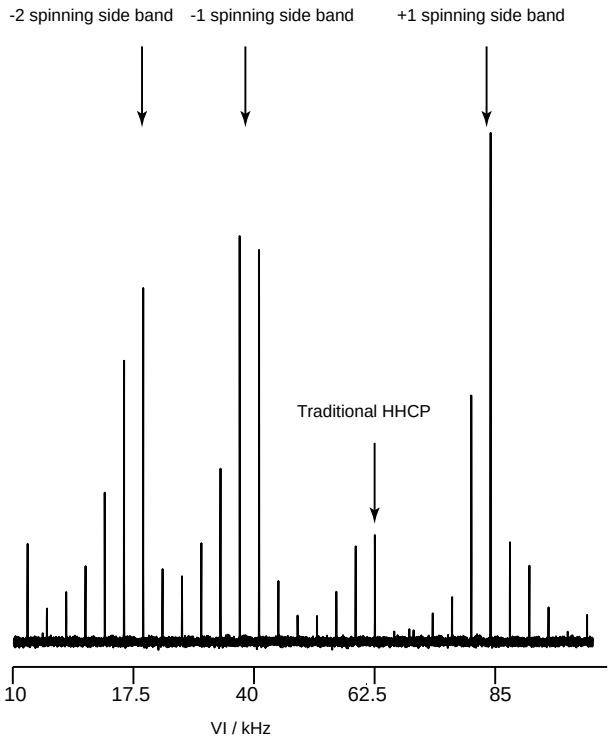

Figure 13 Matching profile at 22 kHz for ^{15}N labelled alanine, as a function of varying the I spin amplitude. Unlike the matching at low spinning the matching profile has broken down to a series of relatively sharp peaks separated by the spinning speed (22 kHz). This makes cross polarisation at fast MAS more difficult.

Due to the much narrower matching condition, the system is now much more sensitive to the RF homogeneity or variations in sample spinning speed. It is therefore more difficult to meet the HHCP condition by using a constant RF amplitude, especially as there may naturally be variations in the matching condition across the sample due to inhomogeneity of the B_1 fields.

Many workers have tackled this problem by using a linear ramped pulse on the proton or X RF amplitude[15-17], with the matching condition being near the middle point of the ramp. This ensures that the amplitude relating to the matching condition will be passed through at some point in the ramp. The main advantage of ramping the RF powers during the contact times is that they compensate for inhomogeneity within the applied B_1 field. The applied B_1 field varies with distance within the coil resulting in a variable precession rate, which is distance dependent. The ramp placed on the RF field limits this effect as the optimum RF field will be swept through for all areas of the rotor. It is common practice to have the optimum matching condition of one of the side bands to be at the centre of the ramp.

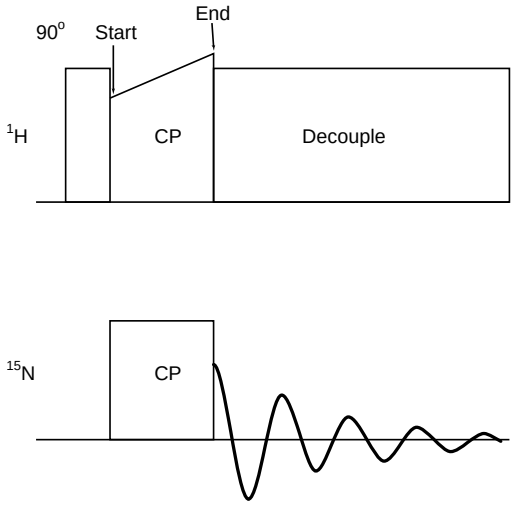

Figure 14 CP pulse sequence with ramp placed on ^{1}H channel. The ramp profile is determined by the starting and end powers used, as well as the contact time used.

Some workers have used more complicated functions than linear ramps, the most common one being the tangential ramp[18-20]. This way, the amplitudes that are not close to the matching condition are quickly swept through, while the gradient of the ramp is decreased for the area of interest. Workers have observed significant increases in intensity (50% increase in intensity in comparison to Hartmann-Hahn CP experiments) using tangential ramps[20,21]. This method may use less power overall as contact times may be decreased, as the time spent on the edge of the matching condition are decreased.

One term commonly used to describe the use of ramps for CP is adiabatic passage. For adiabatic passage to be achieved the matching condition needs to be swept through slowly, allowing the efficient transfer of magnetisation. In Hartmann-Hahn CP experiments, the magnetisation is equally distributed between the two nuclei, where it is shown to oscillate. When the adiabatic passage is fulfilled this allows the complete transfer of magnetisation from one nucleus to another, therefore a theoretical increase in sensitivity of 200% can be achieved.

As previous ramp investigations[15-17] were focused on ^{13}C it was necessary to see if a similar result was seen for ^{15}N CP. This chapter will summarise the work performed into CP optimisation while detecting on ^{15}N and how this can be applied to indirect detection.

4.2.1 Experimental for CP investigation

In order to get a better understanding on the ramped CP for ^{15}N an in depth investigation was performed looking at the ramp difference on the sensitivity at fast MAS (22 kHz). All initial work used 100% ^{15}N labelled alanine to maximise spectrometer efficiency. For the work a 3.2mm probe

was used and the sample was packed for standard experiments, where one spacer was used to limit the effect of RF inhomogeneity. More spacers could have been used to ensure the sample was at the centre of the coil, but this would have meant less material was used. This would have had little impact for the fully labelled system, but would have led to increased experimental time when working for natural abundance ^{15}N. As the aim of this investigation was to improve the sensitivity in detection of ^{15}N, it would have been counter intuitive to use less material.

One advantage of using alanine as the model compound is that it has a relatively long $T_{1\rho}$, enabling relatively long contact times to be used. Some compounds have $T_{1\rho}$ values that are significantly shorter, which results in shorter contact times being used to reduce the impact of signal loss due to $T_{1\rho}$ relaxation. The CP process is less efficient at short contact times however, as the magnetisation does not have sufficient time to transfer fully.

For each ramp condition a standard set of contact times were investigated (0.1ms – 3ms) to ensure that maximum signal was detected for each ramp investigated. To measure the CP efficiency with respect to the ramp difference the intensity of the ^{15}N peak was recorded for each contact time. The intensity for each ramp difference was then plotted with respect to the contact time to see what ramp difference gave the most efficient CP build up. A series of macros have been created for the ramped CP investigation, to maximise efficiency of the spectrometer (see Appendix 3-6).

4.2.2 Results for linear ramped CP

To ensure that the optimum CP efficiency is achieved, the contact time needs to be optimised for every ramp condition. The contact time needs to be optimised for every ramp condition, as when the ramp difference is increased it may take longer to 'sweep' through the matching condition. For each ramp difference used, a series of contact times were investigated to see which gave the best signal to noise, i.e. sensitivity. The effect of the ramp difference and the contact time was investigated and gave the following results (see **Figure 15**).

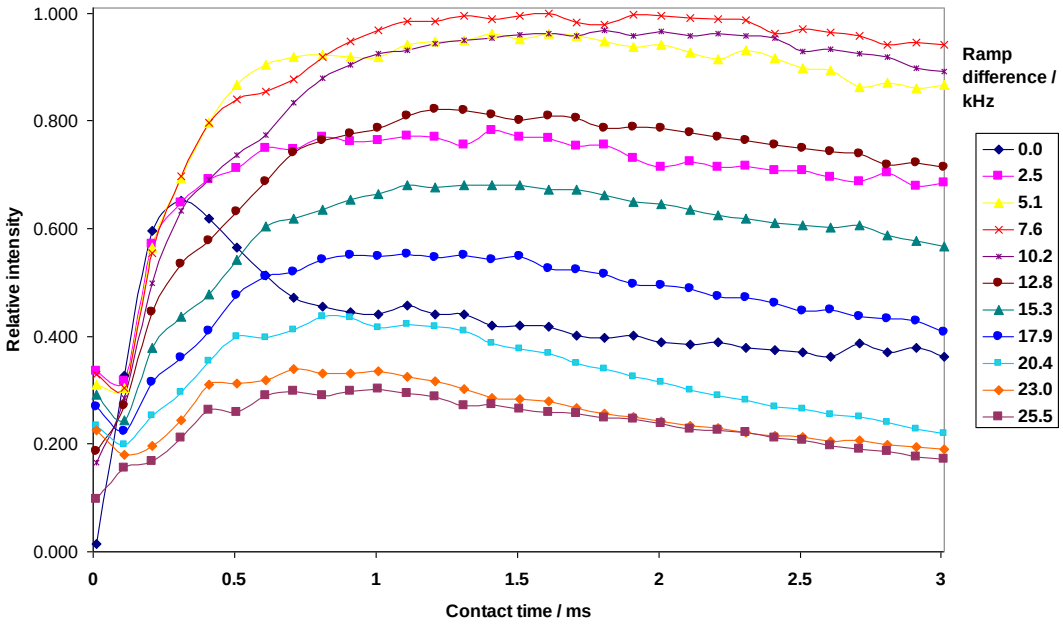

Figure 15 Plot showing effect of varying ramp difference on CP efficiency for sideband -1, for ^{15}N labelled alanine. From the plot an increase in sensitivity can be seen by increasing the ramp difference, until a maximum is reached (7.6 kHz). Increasing the ramp difference further results in a reduction in sensitivity as the matching condition is swept through too quickly and adiabaticity is lost.

The matching sideband that is used will also have an affect on the profile due to the different powers used. To limit this effect all the work is performed at constant MAS rates (22 kHz) and the -1 spinning side band used, unless otherwise stated.

From the results, it is clear to see that as the ramp difference is increased from zero, a gradual increase in sensitivity is seen. The sensitivity of the CP signal reaches a maximum when the ramp difference is 8 kHz, on increasing the ramp difference further leads to a decrease in signal. This is due to the matching condition being swept through too quickly, and less efficient CP occurs. The contact time can not be extended to allow for a more gradual sweep through the matching condition, as there would be no increase in signal due to $T_{1\rho}$ becoming more of an issue. Also for larger ramp differences it means the potential to sweep through two matching conditions is increased. If two sidebands are swept through this means that magnetisation will be transferred from ^{15}N and back onto the ^{1}H resulting in loss of signal.

Another interesting observation from the graph is the variation in the profile of the build up curves with respect to time. For when there is no ramp, the build up curve is comparable to that of a well defined two spin system as seen in **Figure 16**. When no ramp is applied the magnetisation oscillates between the two nuclei and this is seen by an oscillation in the magnetisation signal.

When a ramp is applied, the build up curve becomes smoother and significantly different to that for no ramp. This is due to the CP efficiency varying throughout the rotor with respect to time, as the RF amplitude is varied. Also as mentioned previously (see section 4.2) the application of ramps during CP allows complete transferral of magnetisation as opposed to oscillation between the two nuclei. The profile of the magnetisation build up for when a ramp is applied is in fact the sum of the magnetisation transfer occurring throughout the rotor with respect to time.

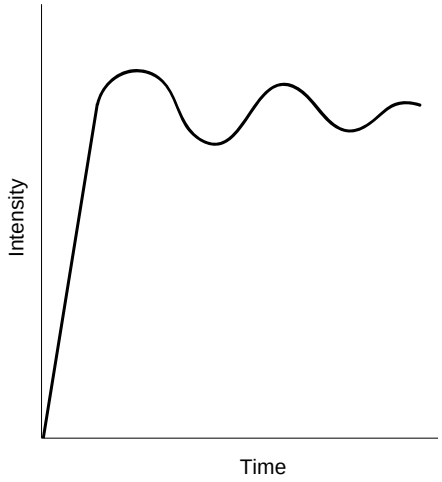

Figure 16 Magnetisation build up curve for Hartmann-Hahn CP for a isolated 2 spin system.

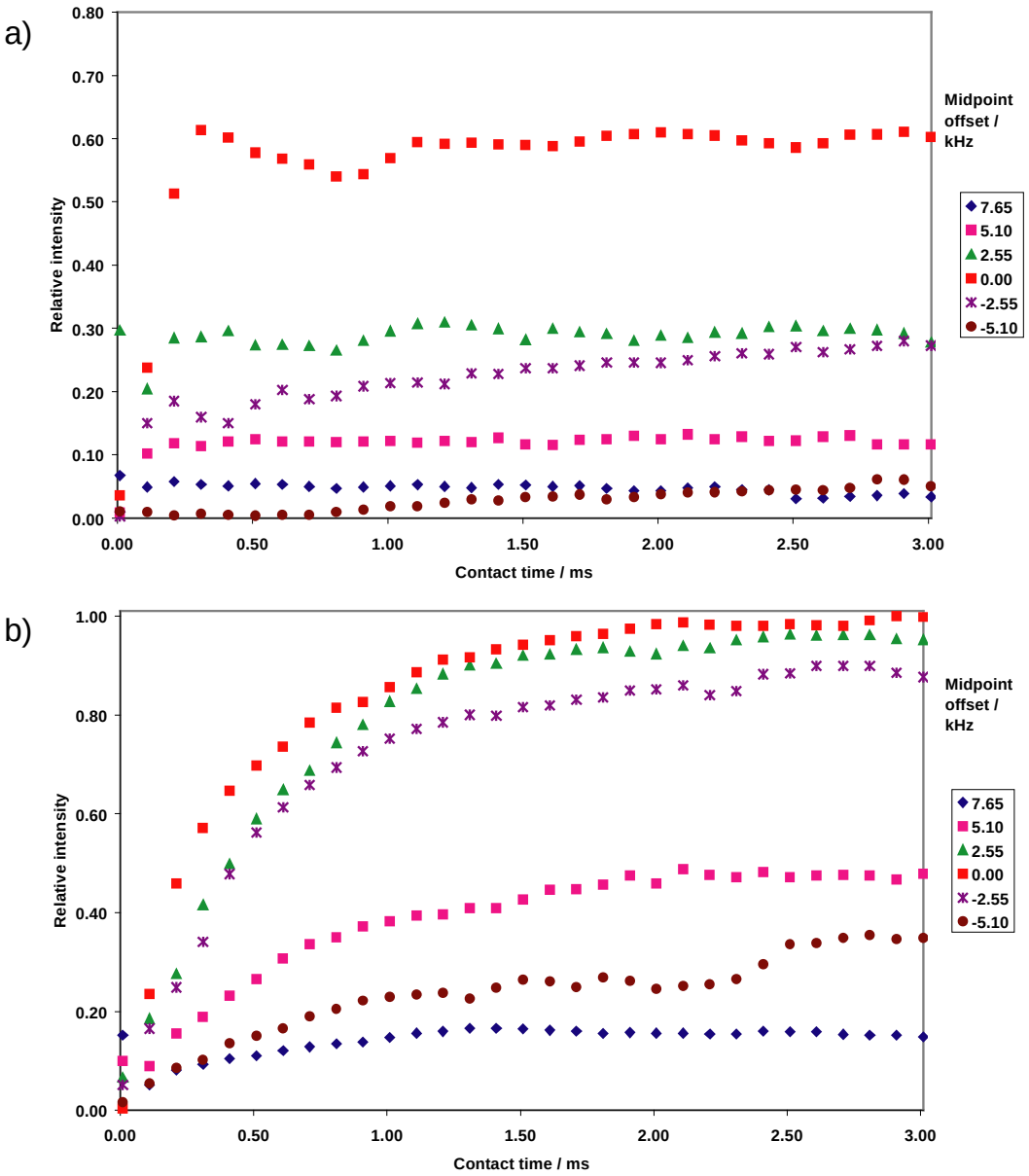

Figure 17 a) Plot comparing CP when there is no ramp on the ^{1}H channel. Any variation from the matching condition results in a sudden loss in signal b) showing how the addition of a ramp makes the CP more robust and less sensitive to variation in the matching conditions, all intensities are relative to optimum CP conditions.

In **Figure 17 a)** it is clear to see that when there is no ramp used for the CP process the sensitivity is greatly reduced for any small variation from the matching condition. Combined with the sensitivity enhancement brought about by the addition of ramps, it is routine for CP to utilise variable RF powers.

In comparison, the same experiment was performed with an optimum ramp (8 kHz) on the ^{1}H channel (see **Figure 17 b)**) and a substantial increase in sensitivity has been achieved (63%) in

comparison to non ramped CP. Varying from the optimum matching conditions does still result in a decrease in sensitivity, however the effect is greatly reduced.

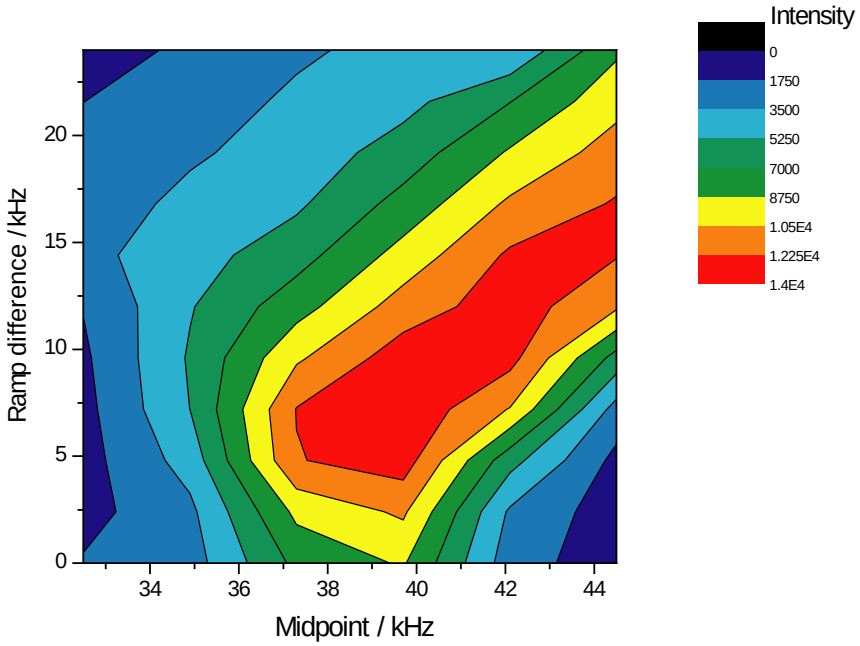

Figure 18 CP efficiency with respect to variation in midpoint of ramp as well as variation in ramp difference. For larger ramp differences there is a shift in the midpoint of the ramp producing the optimum CP conditions.

Combining the effect of increasing the ramp difference and the midpoint of the ramp gave **Figure 18**. From the 2D plot, it is clear to see a shift in the optimum midpoint when the ramp difference increases. The optimum ramp difference is around 8 kHz, and on increasing the ramp difference results in a gradual decrease in signal. The shift in the maximum intensity for larger ramp differences is independent of which side band is used (-1 or +1).

The shift in the optimum midpoint with larger ramp differences is because of an inhomogeneous applied RF field (see section 4.3). As described in the experimental section (see section 4.2.1) normal sample volumes were used. Therefore, at the edge of the rotor RF inhomogeneity is more of an issue, which can be compensated by the application of ramped RF powers. As a result, as the midpoint is varied it allows more efficient CP to occur for different areas within the coil.

4.2.3 Conclusions

The use of ramped CP for ^{15}N at fast MAS is able to make the process far more efficient and robust than CP where no ramps are used. The sensitivity of CP is improved by the addition of ramped RF

pulses as it allows for inhomogeneity of the RF field (which is explained in more detail later on in this chapter).

The variation of the RF powers also allow for any differences in the matching condition, i.e. spinning is not stable, making ramped CP a more robust technique. The build up curves are able to provide subtle information into how the sensitivity improvements are brought about. As the RF amplitude are varied it allows different areas within the rotor to undergo CP at a specific time, where previously only the sample towards the centre of the coil was signal detected.

The ramp investigation also shows that ^{15}N CP at fast MAS behaves as expected, where on the addition of ramps leads to an increase in intensity where a maximum is reached. After this, the addition of larger ramp differences results in loss of signal due to loss of adiabaticity.

4.3 RF inhomogeneity

For traditional HHCP the RF inhomogeneity has little impact, since the precession rates of the two nuclei vary together, as such the CP efficiency will be symmetric about the midpoint. The inhomogeneous RF field has a much greater influence when CP is performed at fast MAS, where the precession rates of the two nuclei are separated by an integer of the MAS rate. The result is that the difference in the precession rate for the two nuclei varies throughout the rotor, and is no longer an integer of the MAS rate (see **Figure 19**). This means that the CP efficiency drops off towards the edge of the rotor due to the RF fields no longer fulfilling the side band match criterion. The area in pink indicates where RF inhomogeneity is largest. Additional spacers can be placed within the rotor so the majority of the sample is contained within the centre of the coil to reduce inhomogeneity. This however will have the undesirable effect of reducing the sensitivity of the experiment. This is seen as undesirable for insensitive for nuclei such as ^{15}N.

A major problem with performing CP at sideband matching is the susceptibility of the experiments to RF inhomogeneity. The solenoid coil is designed so that the RF pulses are approximately uniform across the middle of the coil, but the degree of uniformity is much less than the B_0 field. It is thought this RF inhomogeneity is causing the asymmetric in the CP efficiency seen previous in **Figure 18**. There has been some work in trying to "map" the RF inhomogeneity by the use of discs of sample at varying positions within the rotor[22]. The inhomogeneity is measured by the variable chemical shift of the ^{19}F due to the Bloch-Siegert shift. The main limitation of this technique is that it is only appropriate for lower field spectrometers. No attempts have been made to measure the RF inhomogeneity of any of the probes, as it would be very time consuming and only specific to that particular probe. Instead a qualitative model of the inhomogeneity has been developed (see

Figure 20), to see if this accounts for the shift in optimum ramp conditions for larger ramps. In this case, it has been assumed the RF inhomogeneity is independent of the RF frequency studied.

In order to explain the asymmetry in the results for the ramp investigation, a simulation was performed, to see how the CP efficiency was affected by the RF inhomogeneity. The simulation was for an idealised two spin system, where initially there was no RF inhomogeneity present. The efficiency of the CP process was plotted as a function of the midpoint of ramp (see **Figure 21**) and the ramp difference.

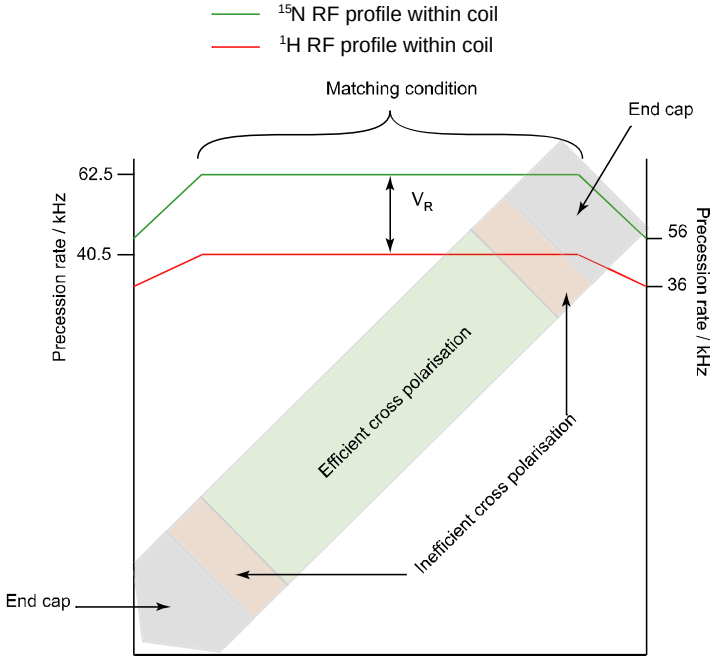

Figure 19 Schematic diagram showing RF field inhomogeneity within the coil at fast MAS CP. The precession rate is separated by the spinning speed (22 kHz) at the centre of the coil. If the precession rate for both nuclei decreases say by 10% at the edge of the coil, the difference in the precession rates is no longer an integer multiple of the MAS rate.

The results of the simulation overall compare well to the experimental data, as when a small ramp is used this leads to a narrow matching condition (~4 kHz) but with a significant increase in sensitivity (~ 20%). Further increasing the ramp leads to a much broader match but with a drop off in intensity.

One major difference in the simulated CP efficiency without RF inhomogeneity taken into consideration and the experimental data is that the simulations are symmetric about the matching condition. In comparison, the experimental data (see **Figure 18**) had a definite shift in the CP efficiency with increasing sweep range. This asymmetric pattern is significantly different to the simulations; one possible explanation for this shift could be a non uniform RF field across the coil.

As the RF power is varied, the effect is that specific areas within the rotor will have the CP conditions met at some point in the experiment. This results in a series of matching conditions occurring throughout the rotor for each RF power used, as seen in **Figure 21 a)**. These new matching profiles can be combined together to simulate the sweep in RF power.

The model used for the inhomogeneity is shown in **Figure 20**. The profile of the RF field will be determined by its distance from the centre. The centre of the coil will have a homogeneous RF power and only decreasing after 30% of the overall distance of the coil is reached. For simplicity sake the RF field decreases linearly from the stated power (100%) to the reduced value (90%).

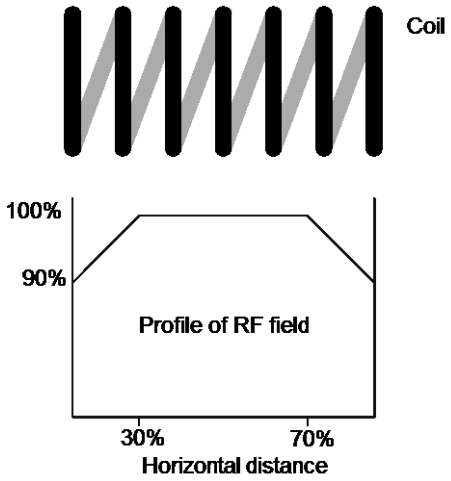

Figure 20 RF profile used to model the RF inhomogeneity.

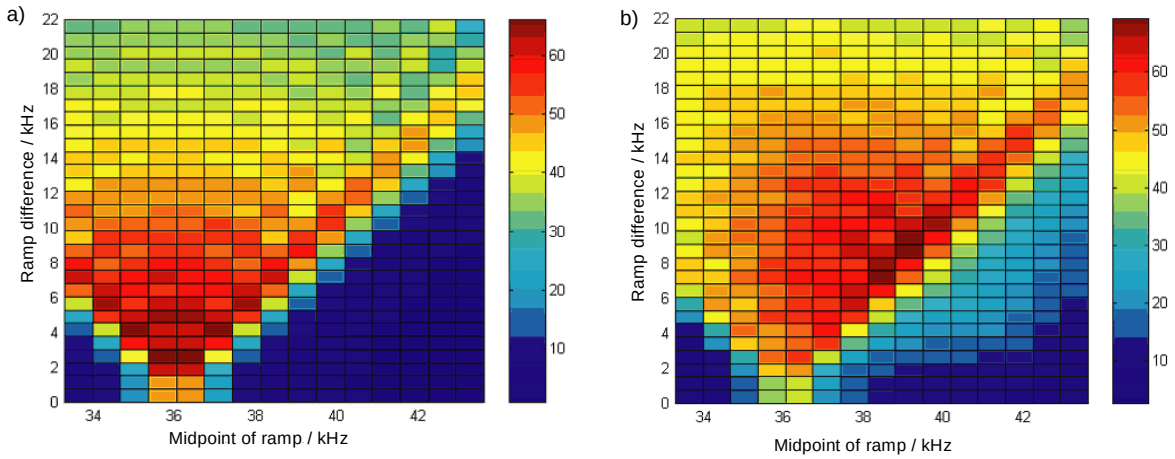

Figure 21 Simulation of CP efficiency where a) is for when RF inhomogeneity is not taken into consideration and is symmetric about the matching condition (36 kHz), b) is for when RF inhomogeneity is accounted for and a shift in signal is seen as for experimental. (see Appendix 7 for Matlab script used).

Using the model system as shown in **Figure 20** gave an asymmetric 2D plot of CP efficiency (see **Figure 21**). This plot clearly shows the same qualitative trend as to the experimental data of **Figure 18**. Although the trend is not identical to the experimental data, it is sufficient to show that the shift in the optimum conditions is because of the RF inhomogeneity. The main reason the experimental and simulated data do not directly compare is due to the simplicity of the model of RF inhomogeneity used. As the purpose of this investigation was to understand qualitatively the RF inhomogeneity, this basic model is shown to be suitable.

4.4 Tangential ramps

Work has been performed showing that using tangential ramped Hartmann-Hahn cross polarisation to be more efficient than traditional linear ramped CP[18-21,23]. Tangential ramps are thought to be more efficient as areas away from the matching condition are swept through rapidly, allowing for any extremes in RF inhomogeneity. The ramp becomes more gradual near the matching profile, resulting in a more efficient transfer of magnetisation.

The main problem with tangential ramps is trying to set up suitable parameters to define the tangential function. Due to the nature of the tangential function, it could be very easy to exceed the maximum power settings of the probe. It was decided that the safest way to define the tangential ramp was with three variables (see **Figure 22**). A brief investigation was setup to measure the efficiency in the magnetisation transfer using the tangential ramped CP. To aid the optimisation it was essential that a macro be created (see Appendix 5) to quickly and efficiently produce experimental parameters, reducing the risk of human error. The macro needs to be flexible so a wide range of experimental parameters can be produced.

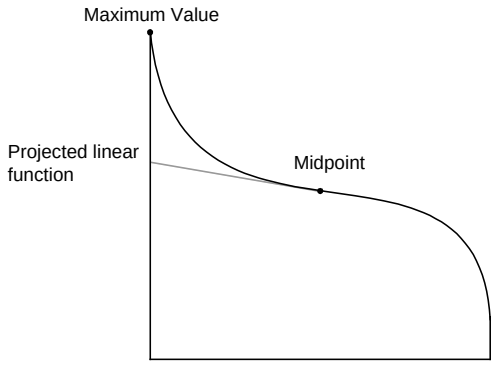

Figure 22 Schematic diagram of tangential pulse. The tangential function is defined with three variables, maximum value, midpoint and projected linear point. To define a linear ramp the projected linear function is defined as the maximum also, i.e. we can easily compare tangential to linear ramps.

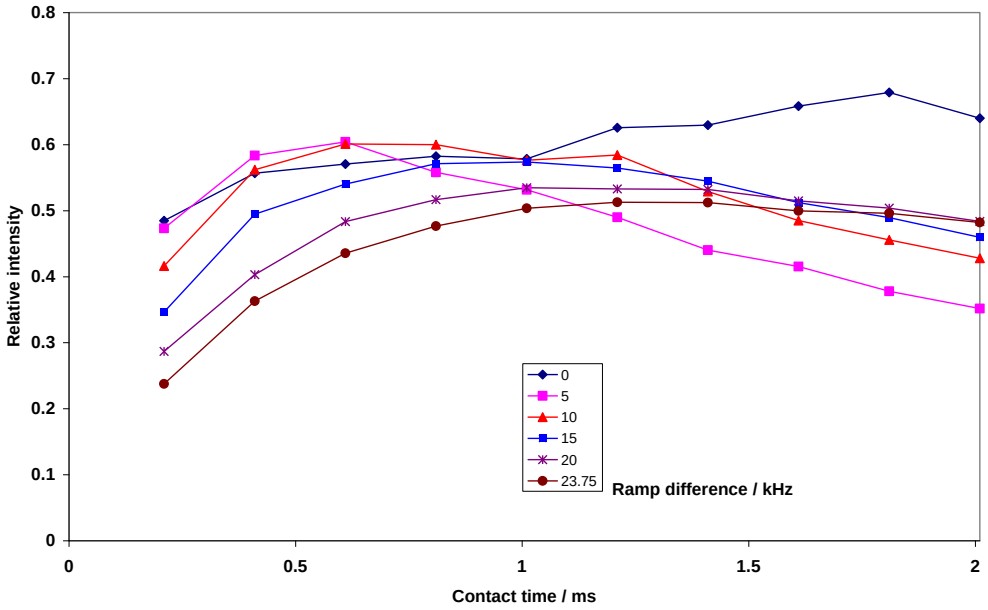

Figure 23 Representative data set comparing tangential function on CP efficiency. Experiments used ^{15}N labelled alanine with varying linear projections and tangential functions. The matching condition was set to the midpoint of the ramp. The optimum condition for each experiment was shown to be basic ramped CP for all experiments.

From the graph (see **Figure 23**) it is clear to see that there is no obvious gain in applying a tangential ramp, as the optimum condition was for linear ramped CP, where the linear projections in this case related to a difference of 8 kHz. The experiment was repeated for a number of tangential ramps and no increase in sensitivity was seen. This just highlights the problem with tangential ramped CP being the difficulty in the optimisation of the process. It is also important to note that previous workers had stated a 50% increase in signal[20], which is comparable to the sensitivity improvement seen by optimising the linear ramped CP. Therefore the tangential ramped CP was not investigated any further due to the additional variables required to optimise for efficient CP.

4.5 Choice of model compound

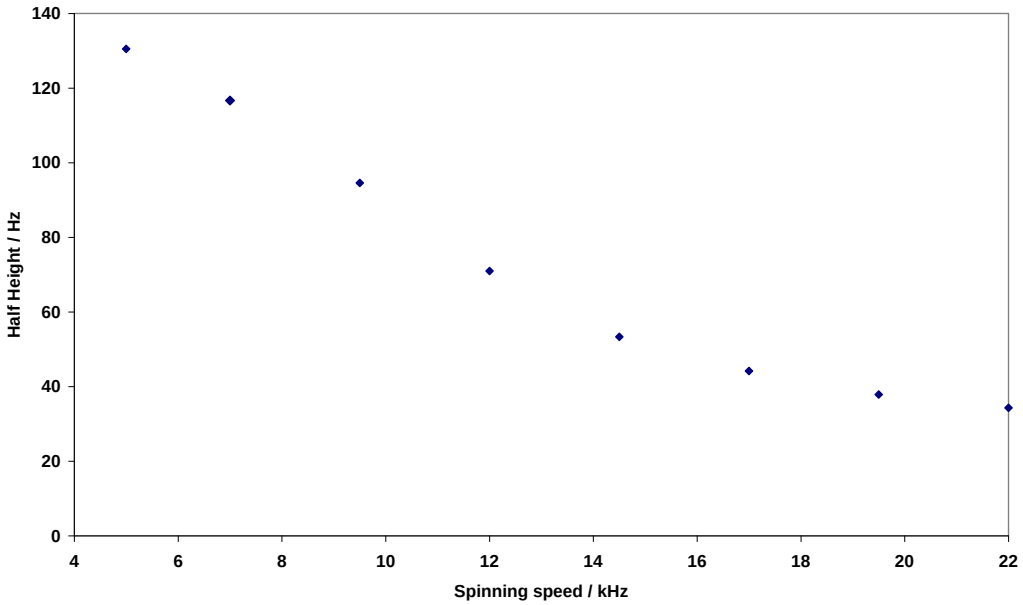

Figure 24 Comparison of ^{15}N peak width as a function of spinning speed. As the MAS rate is increased there is a significant reduction in peak width.

Although initial work used alanine as a model compound, this proved less suitable for subsequent quantitative work. As shown in **Figure 24**, the ^{15}N linewidth varies significantly with the MAS rate, complicating the comparison of sensitivity at modest spin rates (direct detection) and fast spin rates (indirect detection). This is unusual for rare spins, (e.g. ^{13}C, ^{15}N), where peaks widths tend to be constant (or even increase) at faster spinning speeds. This may be related to the rotation about a NH_3 bond interfering with the MAS. As the spinning rate is increased the temperature increases due to frictional effects, which will affect the NH_3 bond rotation, and narrower lines are seen. This makes comparing the efficiency of the CP process at a fast and slow MAS near impossible.

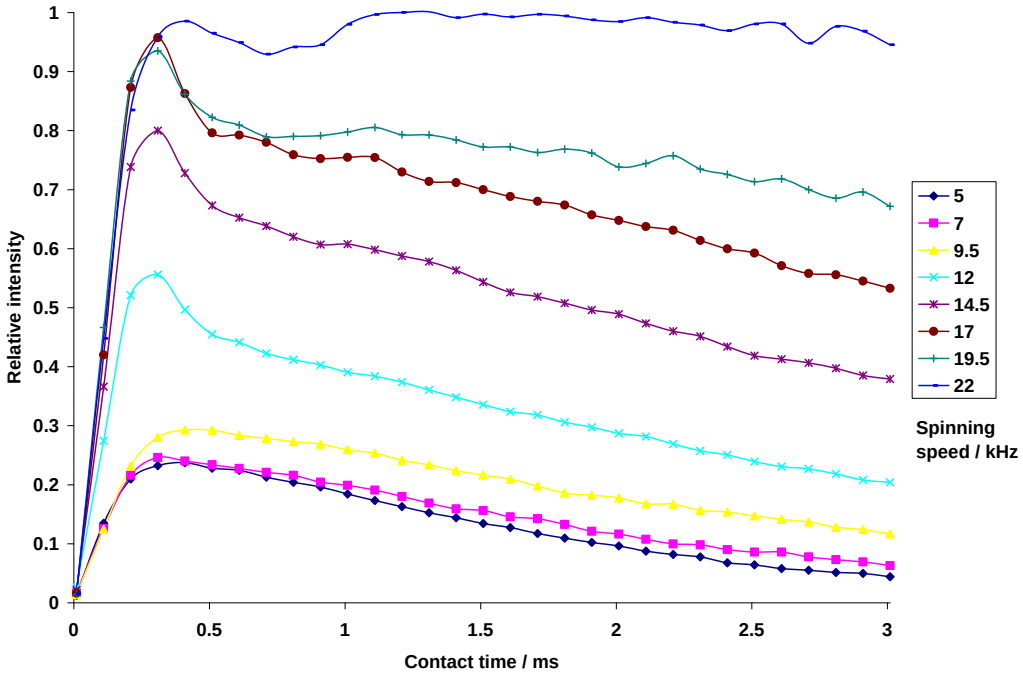

Figure 25 ^{15}N CP build ups curves ^{15}N labelled alanine as a function of spinning rate.

Figure 25 shows CP build up curves at eight different spinning speeds, with the cross-polarisation optimised at each speed. $T_{1\rho}$ is clearly strongly dependent on the spinning speed (the intensity fall off is much slower at high spinning speeds). Experiments at a constant MAS rate and a variable temperature showed that $T_{1\rho}$ is strongly temperature dependent i.e. this behaviour is largely the result of different degrees of frictional heating with MAS rate. The rate of build up is also strongly MAS rate dependent, increasing at faster MAS rates, which is unusual. This complex and atypical behaviour made alanine unsuitable for further quantitative studies.

Proline was initially investigated as an alternative model compound, as the N site should be relatively immobile, but the draw back of having limited motion within the solid is the associated long pulse delays (~120 s) required, due to the long T_1 value of the ^{1}H's. Further work used double ^{15}N labelled asparagine, **Figure 26**.

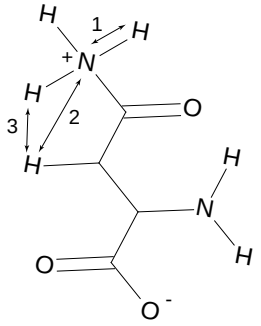

Figure 26 Structure of asparagine with important distances highlighted[24]. Distance 1 shows the length of the N–H bond which is 0.995Å and corresponds to a coupling of 12.36 kHz. Distance **2**

is the distance between the ^{15}N and the second closest ^{1}H and is 2.076Å, corresponding to a coupling of 1.36 kHz. Finally distance **3** is the distance the two ^{1}H's are apart and is 2.240 Å. The coupling between them is 10.68 kHz.

4.6 Indirect detection

The indirect detection consists in essence of five steps; the first is transfer of magnetisation from the protons onto the nitrogen via CP, the remaining magnetisation on the protons is then suppressed with de-phasing pulses. The magnetisation is allowed to evolve on the nitrogen to be able to distinguish between different sites, e.g. chemical shift, before the magnetisation is then transferred back onto the protons and acquired.

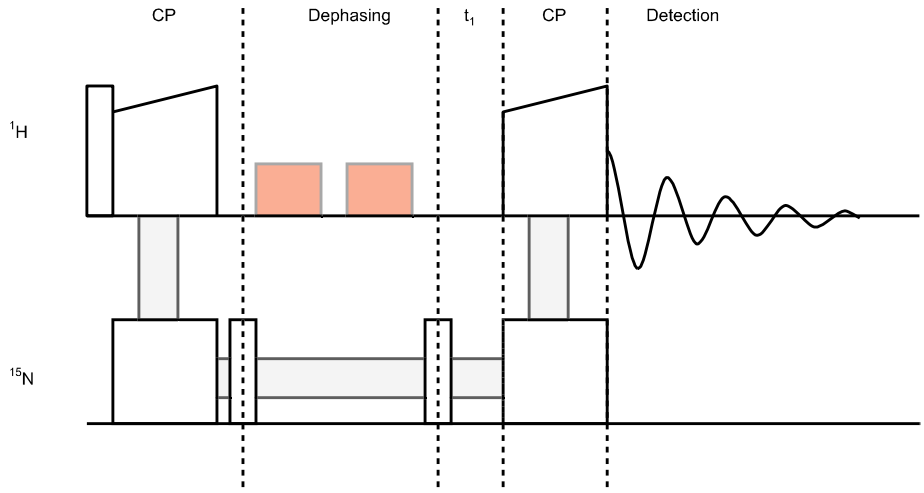

Figure 27 Pulse sequence for indirect detection. Initial magnetisation is transferred from ^{1}H to ^{15}N via CP pulse. Magnetisation is temporarily placed into z plane and the remaining proton magnetisation is dephased. ^{15}N magnetisation is then placed back into xy plane and allowed to evolve on ^{15}N during t_1, before being transferred back onto the ^{1}H and detected. Experimental conditions used for these results are a ^{1}H 90º pulse of 3.2µs, with a contact time of 1 ms used with a acquisition time of 51.2ms in the direct dimension. A spectral width of 100,000Hz in the direct dimension and 8333.3 Hz in the indirect dimension was used. A pulse delay of 16 s was used with 8 acquisitions recorded for every row.

4.6.1 Magnetisation transfer during indirect detection

For short contact times the magnetisation is predominantly transferred to the X nucleus from the closest ^{1}H only[25]. As the contact times are increased this allows the magnetisation to transfer within the ^{1}H network, where it can then be transferred onto the X nuclei from the neighbouring ^{1}H. Although in principle magnetisation could be transferred directly via long-range ^{15}N,^{1}H dipolar couplings, the rapid "spin diffusion" in the ^{1}H coupling network means that magnetisation from more distant spins is mostly transferred in a "relay" fashion towards the closer spins, and then onto the ^{15}N.

When the magnetisation transfer is reversed as in the case of indirect detection, the magnetisation will initially be transferred onto the ^{1}H in closest proximity. As the magnetisation is only on one ^{1}H environment this will result in a relatively sharp ^{1}H line, meaning that suitable signal to noise can be achieved in fewer number of scans. For longer contact times the magnetisation will 'mix' within the ^{1}H network, meaning the signal will be distributed across a number of ^{1}H environments, leading to broader lines. This broadening of lines for longer contact times may limit the effect in the sensitivity improvement, as larger number of scans will be required to get suitable signal to noise.

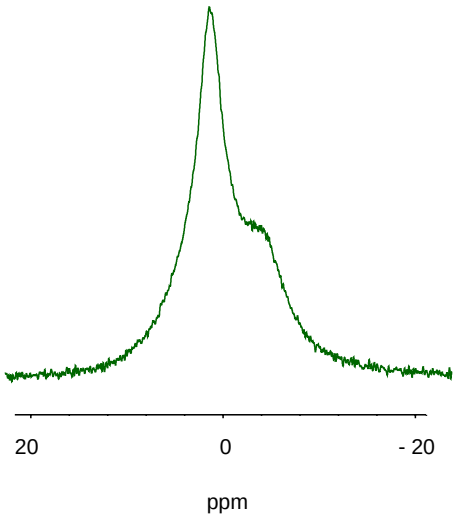

Figure 28 ^{1}H spectrum of indirectly detected ^{15}N asparagine at 22 kHz MAS.

Once the indirect detection had been optimised, a reference was recorded to compare against CP performed at modest MAS rates (~5 kHz) so that to see if there was any improvement in sensitivity. One complication however is the inability to resolve the two nitrogen sites, due to the broad lines and small chemical shift range of ^{1}H. From **Figure 28** it is clear to see that there are two distinct signals detected, however it is not possible to resolve them. It is therefore necessary to perform 2D experiments if there is more than one ^{15}N environment present.

4.6.2 Proton suppression

One significant problem associated with indirect detection of natural ^{15}N abundance is suppression of the ^{1}H signal not associated with ^{15}N. Workers have used filters previously to remove the unwanted ^{1}H signal, with a large amount of success, with around 99% of unwanted ^{1}H signal suppressed[26,27]. However, the remaining proton signal is still often much greater than the signal associated from the ^{15}N, and must be removed by phase cycling[26].

However, if the "background" ^{1}H signal that has not being involved in the ^{15}N CP is still large, this creates a "dynamic range" problem in trying to detect the weak signal of interest. Care has to be taken when setting the sensitivity of the detector (the signal gain). Too high of a value and the signal will be outside the digitiser limits, too low and the signal associated with the ^{15}N will be below the digitiser threshold. Even if the gain is set appropriately, relying on phase cycling to suppress a large background signal makes the experiment very sensitive to small variations in the background. This will result in large amounts of "t_1 noise". This background ^{1}H signal arises from ^{1}H magnetisation in the sample which has not passed through the ^{15}N CP, but also probe background ^{1}H signals in the equipment e.g. rotor end caps.

Two forms of filters have been suggested to suppress the ^{1}H signal, where the first is a resonance recoupling (RR) filter first proposed by Oas *et al*[28] and later used in the indirect detection method by Ishii *et al*[6]. The RR filter is a train of relatively long pulses (~400μs) which saturates the ^{1}H signal. The RR filter has been briefly investigated, and has been shown to be efficient at removing proton signal due to probe background as well as the sample. When the RR filters were investigated it was found the total time the RR filters were applied to be important, as opposed to the individual pulse length.

Z-filters[29-33] are also used in indirect sequences, which were first discussed for liquid state applications. Z-filters store the magnetisation of interest, in this case the signal associated with the ^{15}N along the z-axis, where the magnetisation is said to be 'parked', while the ^{1}H signal in *xy* plane decays due to T_2. After a sufficient time, around 1ms for ^{1}H, the magnetisation has completely decayed and then transferred back in to the Z-plane. The ^{15}N magnetisation is then restored onto the *xy* plane where it is allowed to precess during t_1. We found the z filter to be particularly good at removing signal from the sample, but not as efficient at removing probe background signal. As a result, we choose to combine both filters as shown in **Figure 27** to ensure maximum suppression of the ^{1}H signal.

4.6.3 Asparagine results

As mentioned previously in the chapter, indirect detection is composed of two CP steps. To ensure that the CP conditions from ^{15}N to ^{1}H were comparable to that of standard CP it was decided to optimise the CP while detecting on ^{1}H. The optimum CP conditions for the indirect detection method in theory should be the same regardless of the direction of the transfer of magnetisation. A brief investigation was performed to verify this.

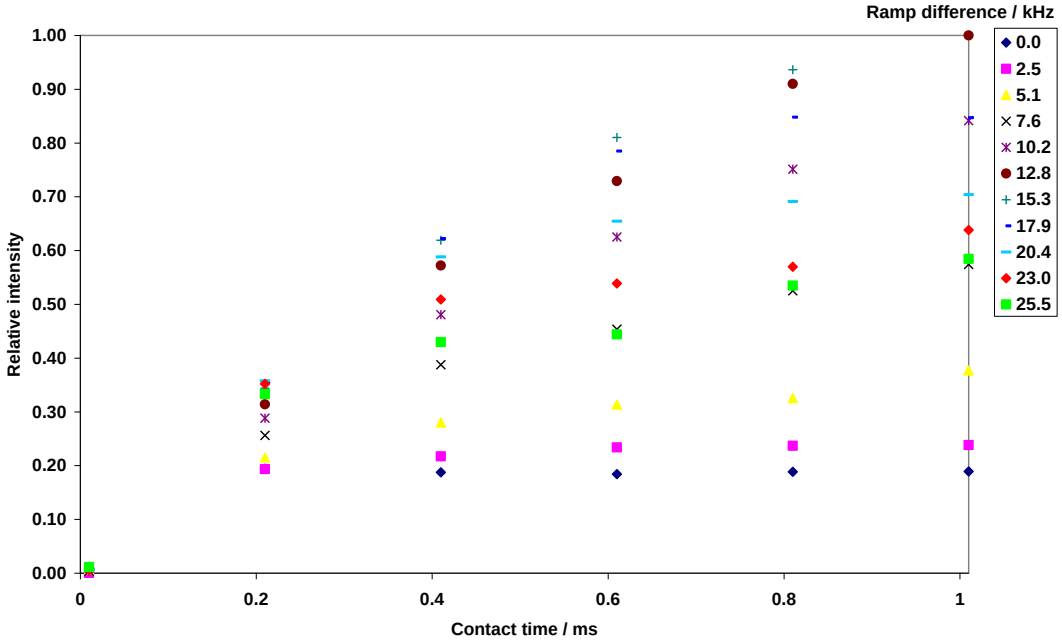

Figure 29 Plot showing magnetisation build up for ^{15}N labelled asparagine using traditional CP detection at 22 kHz and measuring intensity of peak at -361 ppm. As previously noted, the addition of a ramp increases the efficiency of the CP.

From the plot (see **Figure 29**) a similar build up curve can be seen to previous CP experiments. Short contact times were used to make a fair comparison, as the $T_{1\rho}$ of the 15N site at -287 ppm was considerably shorter than that at -361 ppm. As the signal was detected on the ^{1}H channel, it was not possible to distinguish between the two sites, due to the poor resolution.

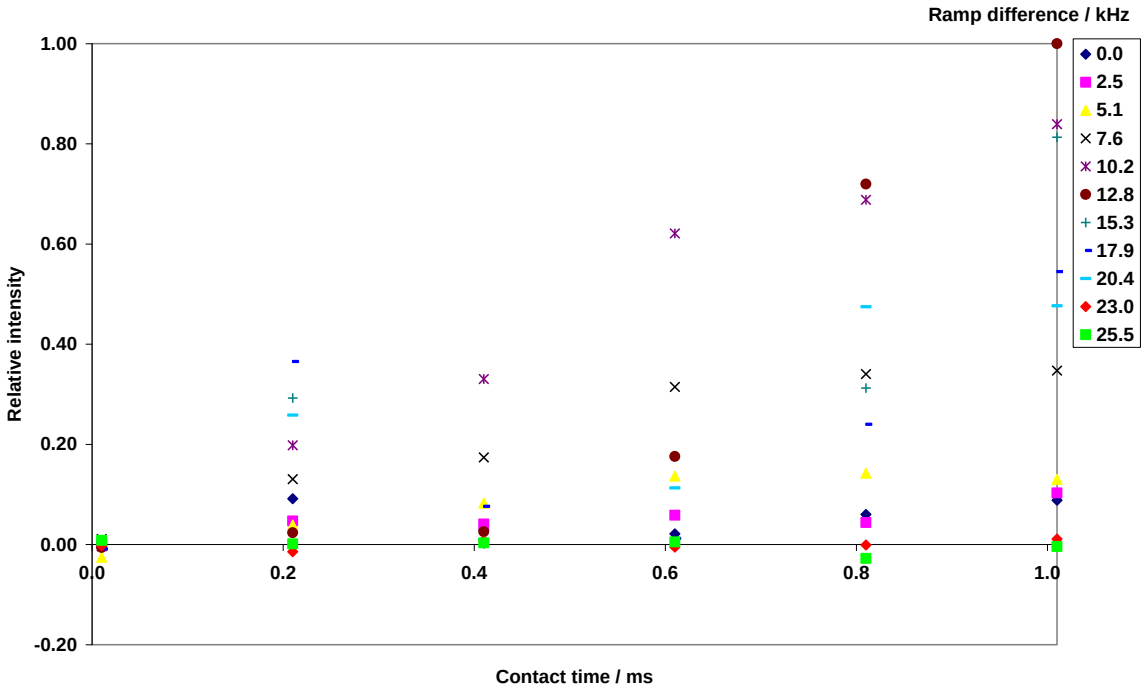

Figure 30 Plot of magnetisation build up with respect to ramp difference for indirect detection. It is important to note that both ^{15}N sites are included within the ^{1}H signal.

When comparing the magnetisation build up for indirect detection (see **Figure 30**) it is clear to see the similarities to that of basic CP. In particular, the optimum ramp difference for CP and indirect detection is the same (13 kHz). This value is slightly different from the initial CP work (8 kHz) which was performed on a different probe. (Using a different probe will produce different optimum ramped CP conditions, due to differences in the RF profiles.)

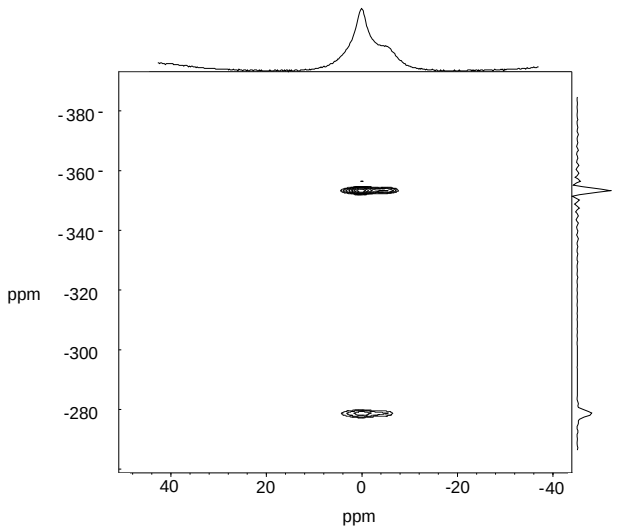

Figure 31 2D indirect spectrum of indirectly detected asparagine. The different ^{15}N environments are now fully resolved and can be quantified.

From the 2D indirectly acquired spectrum of ^{15}N labelled asparagine (see **Figure 31**) it is possible to resolve the peaks fully. As the work was with ^{15}N labelled asparagine the signal to noise for both experiments exceeded the quantifiable limit (1000) for the spectrometer. It was therefore not possible to state the sensitivity enhancement moving from CD to indirect detection. It was therefore necessary to use a more realistic system to measure the sensitivity improvement.

One method was to 'dilute' the labelled system with unlabelled asparagine to reduce the concentration of ^{15}N present. A more interesting problem involved trying to quantify the ratio of compounds present in a partially labelled chitin/chitosan compound (~10%).

4.6.4 Chitin/chitosan results

To determine the efficiency of indirect detection, a more realistic system needed to be investigated. The system that was decided upon was a mixture of chitin and chitosan. Chitin is the second most abundant occurring polysaccharide in nature (after cellulose), and can be found in cell walls of fungi and the exoskeletons of anthropoids. Chitosan is produced by the deacetylation of chitin using strong basic conditions (see **Figure 32**). This deacetylation does not occur at all the sites, and the ratio can be quantified by ^{15}N and solid-state NMR[34].

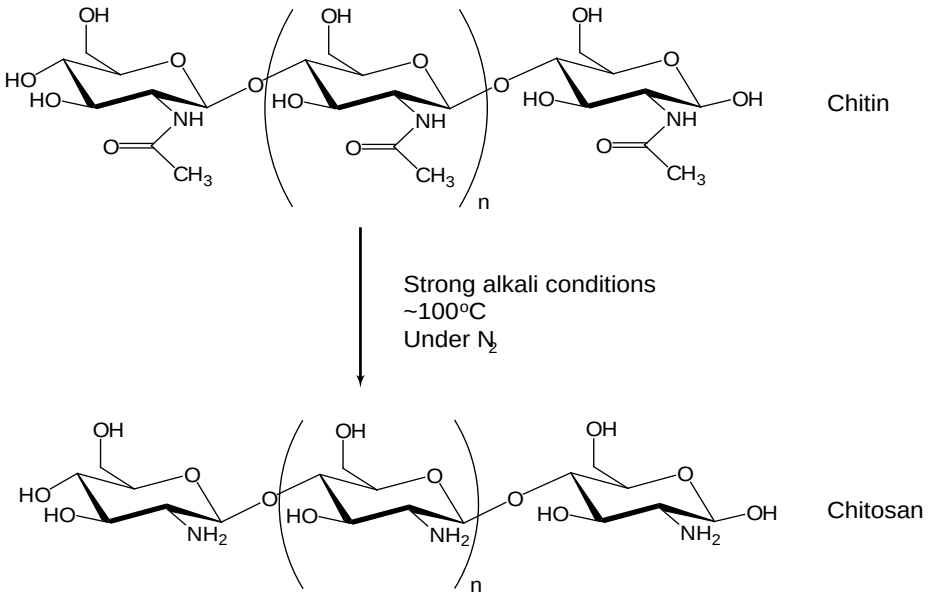

Figure 32 Structure of chitin, and how this can be used in the production of chitosan

As these compounds are produced by micro-organisms, it is relatively easy to label the system with ^{15}N, and this was performed at Durham University by Helen Watson. The compounds are labelled with a concentration of around 10% of ^{15}N, making it possible to compare the sensitivity

improvement of indirect detection with respect to CP. In addition, the unknown ratio of chitin to chitosan makes this an interesting system, as the ratio of the two compounds can be quantified.

The signal to noise was used to compare the sensitivity of the direct vs. indirect detection methods in spectra obtained using the same contact time. The signal to noise for CP was measured by taking the intensity of the peak at -273 ppm, after applying an approximately matched filter (100 Hz Gaussian) and comparing it to the standard deviation of the noise. The matched filter optimises this signal-to-noise ratio. The same approach was used in the indirectly detected spectrum, which is now a 2D. A matched filter will be applied in both dimensions and the signal to noise calculated from the intensity of the 2D peak at -273 ppm relative to the standard deviation of the noise within a sample region.

There is a modest increase in the signal to noise (around 150%), but nothing like what is stated by previous workers. One of the main reasons why the signal to noise improvement is not comparable to previous work, is the typically broad lines for chitin and chitosan. The ^{1}H linewidths for these compounds are broader due to the disorder within the system (~5 kHz). This highlights the major problem with indirect detection, which is the typically broad ^{1}H linewidths. Only compounds with sufficiently narrow ^{1}H lines are suitable to detect insensitive NMR nuclei via indirect detection.

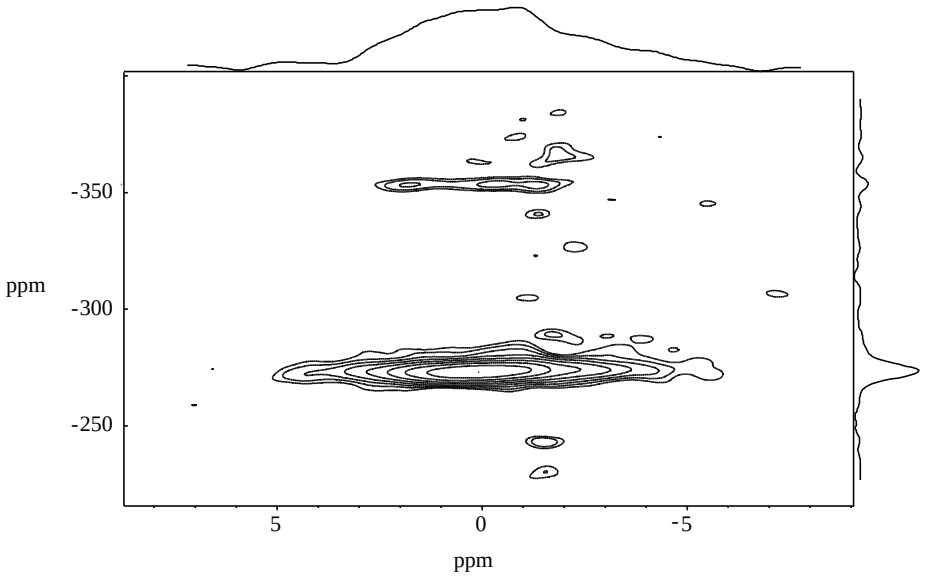

Figure 33 Inverse detection of chitin/chitosan mixture at 22 kHz with a short contact time of (0.4 ms), 512 acquisitions and 24 t_1 increments of 120μs, resulting in a time of 2.88 ms acquisition time in the indirect dimension. A line broadening function was added in both the direct and indirect (400 Hz Gaussian and 100 Hz Gaussian respectively). For peak at -273.6 gave a S/N of around 16 for a experimental time of 400 minutes.

The spectrum also highlights the difficulty in the setup of efficient 2D experiments. The spectral width needs to be sufficiently large to prevent folding of peaks, but not so large that any

improvement in sensitivity is lost due to exceptionally long experiment times. In this case, it took 400 minutes to acquire the 2D spectrum of chitin/chitosan.

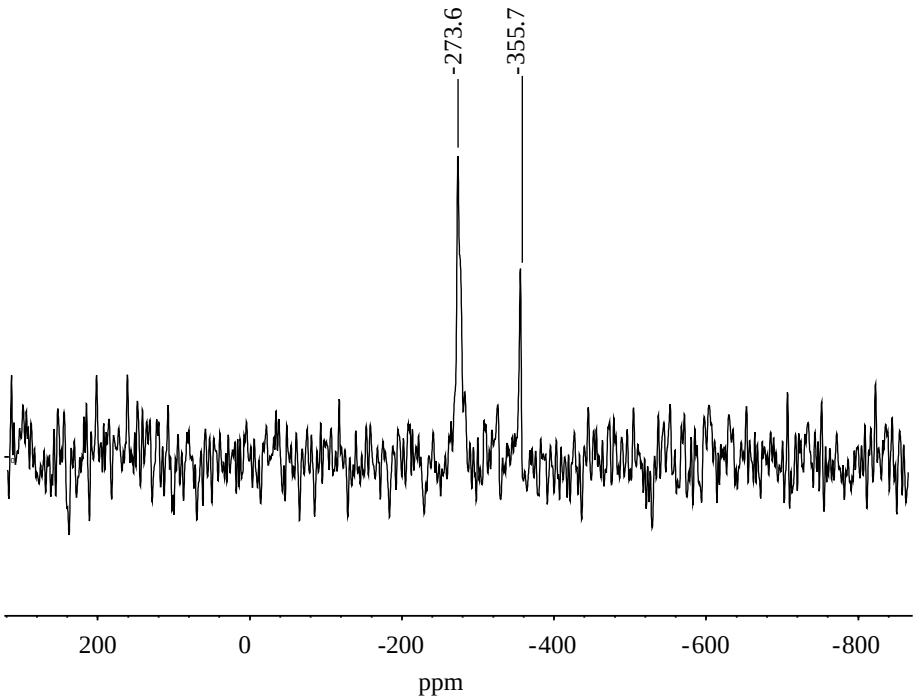

Figure 34 CP of chitin/chitosan mixture, with a short contact time (0.4 ms), and 1024 acquisitions, with a matched line-broadening (100 Hz Gaussian) gave a signal to noise of 2.9 for peak at -273.6 ppm for a 30 minute experiment.

From the results achieved there was a increase in signal to noise, compared to CP. However this increase in signal to noise is somewhat less to some previous work, where increases of between five and ten times were obtained. Workers who stated such great increases in sensitivity had made direct comparisons with 2D experiments where the ^{15}N was detected via CP. This was a more appropriate form of comparison as the same 2D conditions can be used and a direct evaluation can be made with regards to signal to noise.

The main problem associated with indirect detection, is the poor resolution associated with the ^{1}H lines. Due to the poor resolution, the experiment has to be performed in a 2D form. These experiments are more complicated than for simple 1D experiments, and due to the experiments being in two dimensions tend to take longer. This means that there is a trade off between signal to noise and experimental time.

Another problem associated with detecting indirectly on the ^{1}H channel is the fast mixing of magnetisation that occurs within the ^{1}H network, meaning the signal will be dissipated over a number of ^{1}H sites. For nuclei with low gyromagnetic ratios, such as ^{15}N, it is necessary to have longer contact times due to the associated ^{1}H couplings being weaker, to ensure full transfer of

magnetisation occurs. As spin locking is applied it allows for spin diffusion to occur, and the resulting magnetisation is 'shared' over a number of ^{1}H sites. This leads the broadening of the ^{1}H lines as the signal is 'spread' over a number of ^{1}H environments, and hence an increase in the signal to noise is not seen. The contact time can not be reduced too far without significantly compromising the overall sensitivity.

4.6.5 Conclusions

Indirect detection is clearly not a viable replacement for 1D ^{15}N NMR under the conditions used here, as the overall sensitivity improvements are not large enough to justify the significantly increased complexity of setting up the required 2D experiment, including optimisation of sample-dependent CP parameters at fast MAS rates. Choosing the 2D parameters, such as spectral width, number of increments, will also be difficult for unknown samples.

Where inverse detection may be more useful is when 2D experiments are already being used i.e. swapping the dimensions to detect on ^{1}H vs. ^{15}N. Decreasing the ^{1}H linewidth e.g. via homonuclear decoupling would boost the advantage of the indirect experiment (although this would involve combining direct detection with the ^{1}H homonuclear decoupling). Similarly if only small sample volumes are available, and so small diameter rotors are being used, indirect detection may be a useful alternative. In cases of samples with a small number of known sites, such as the chitin/chitosan example above, is it possible to set up a "compact" 2D experiment with a very limited number of increments in the indirect dimension. This may be another situation where indirect detection becomes viable.

We have also shown that RF in-homogeneity is an important factor in CP experiments at fast MAS rates, but that appropriate use of RF ramps can lead to CP efficiencies which are comparable to those obtained at more modest spin rates.

4.7 References

(1)Martin, G. E.; Crouch, R. C. *Journal of Natural Products* 1991, *54*, 1.

(2)Bosman, L.; Madhu, P. K.; Vega, S.; Vinogradov, E. *J. Magn. Reson.* 2004, *169*, 39.

(3)Lesage, A.; Sakellariou, D.; Hediger, S.; Elena, B.; Charmont, P.; Steuernagel, S.; Emsley, L. *J Magn Reson* 2003, *163*, 105.

(4)Vinogradov, E.; Madhu, P. K.; Vega, S. *Chem Phys Lett* 2002, *354*, 193.

(5)Hong, M.; Yamaguchi, S. *J. Magn. Reson.* 2001, *150*, 43.

(6)Ishii, Y.; Tycko, R. *J. Magn. Reson.* 2000, *142*, 199.

(7)Schnell, I.; Saalwaechter, K. *J. Am. Chem. Soc.* 2002, *124*, 10938.

(8)Khitrin, A. K.; Fung, B. M. *J. Magn. Reson.* 2001, *152*, 185.

(9)Ishii, Y.; Tyesinowski, J. P.; Tycko, R. *J. Am. Chem. Soc.* 2001, *123*, 2921.

(10) Parella, T.; Belloc, J. *Magn. Reson. Chem.* 2002, *40*, 133.

(11) Paulson, E. K.; Martin, R. W.; Zilm, K. W. *J. Magn. Reson.* 2004, *171*, 314-323.

(12) Fu, R. *Chem. Phys. Lett.* 2003, *376*, 62-67.

(13) Hartmann, S. R.; Hahn, E. L. *Phys. Rev.* 1962, *128*, 2042-2053.

(14) Stejskal, E. O.; Schaeffer, J.; Waugh, J. S. *J. Magn. Reson.* 1977, *28*, 105-112.

(15) Metz, G.; Wu, X.; Smith, S. O. *J. Magn. Reson. Ser. A* 1994, *110*, 219-227.

(16) Peersen, O. B.; Wu, X.; Kustanovich, I.; Smith, S. O. *J. Magn. Reson. A* 1993, *104*, 334.

(17) Rossum, B.-J. v.; Förster, H.; Groot, H. J. M. d. *J. Magn. Reson.* 1997, *124*, 516-519.

(18) Baldus, M.; Geurts, D. G.; Hediger, S.; Meier, B. H. *J. Magn. Reson. Ser. A* 1996, 140-144.

(19) Rovnyak, D.; Baldus, M.; Itin, B. A.; Bennati, M.; Stevens, A.; Griffin, R. G. *J Phys Chem B* 2000, *104*, 9817.

(20) Tomaselli, M.; Hediger, S.; Suter, D.; Ernst, R. R. *J Chem Phys* 1996, *105*, 10672.

(21) Hediger, S.; Meier, B. H.; Ernst, R. R. *Chem Phys Lett* 1995, *240*, 449.

(22) Vierkotter, S. A. *J. MAgn. Reson. A* 1996, *118*, 84.

(23) Baum, J.; Tycko, R.; Pines, A. *Phys. Rev. A* 1985, *32*, 3435-3447.

(24) Flaig, R.; Koritsanszky, T.; Dittrich, B.; Wagner, A.; Luger, P. *J. Am. Chem. Soc.* 2002, *124*, 3407.

(25) Muller, L.; Kumar, A.; Baumann, T.; Ernst, R. R. *Phys. Rev. Lett.* 1974, *32*, 1402.

(26) Fischbach, I.; Thieme, K.; Hoffmann, A.; Hehn, M.; Schnell, I. *J. Magn. Reson.* 2003, *165*, 102.

(27) Schnell, I.; Langer, B.; Sontjens, S. H. M.; Van G Enderen, M. H. P.; Sijbesma, R. P.; Spiess, H. W. *J. Magn. Reson.* 2001, *150*, 57.

(28) Oas, T. G.; Griffin, R. G.; Levitt, M. H. *J. Chem. Phys* 1988, *89*, 692.

(29) Brereton, A. M.; Crozier, S.; Field, J.; Doddrell, D. M. *J. Magn. Reson.* 1991, *93*, 54.

(30) Hurd, R. E.; John, B. K. *J. Magn. Reson.* 1991, *91*, 648.

(31) Hurd, R. E.; John, B. K.; Plant, D. J. *J. Magn. Reson.* 1991, *93*, 666.

(32) John, B. K.; Plant, D. J.; Heald, S.; Hurd, R. E. *J. Magn. Reson.* 1991, *94*, 664.

(33) John, B. K.; Plant, D. J.; Hurd, R. E. *J. Magn. Reson. A* 1993, *101*, 113.

(34) Varum, K. M.; Anthonsen, M. W.; Grasdalen, H.; Smidsrod, O. *Carbohydr. Res.* 1991, *211*, 17.

5 Understanding resolution in ^{19}F containing compounds

5.1 Introduction

There is great interest in improving resolution of ^{19}F solid-state NMR in the pharmaceutical industry. ^{19}F is a very useful NMR nucleus as it is highly receptive due to its 100% abundance and high gyromagnetic ratio, meaning that it can be easily detected even when in dilute concentrations. Another reason why ^{19}F NMR is useful is that ^{19}F is often present in the active compound, while not in the inactive excipient. As a result, the active drug can be detected in the final formulated blend even in very small quantities.

One drawback with ^{19}F NMR is that the linewidths are often large, often in the region of 800 Hz. In order to improve the resolution and sensitivity of ^{19}F in solid-state NMR a better understanding of what contributes to the linewidth is required. In proton NMR linewidths are dominated by the strong homonuclear dipolar couplings. The situation is less clear for ^{19}F, where dipolar couplings are weaker and CSAs are larger, and also ^{1}H decoupling is often a factor. In order to understand the factors affecting linewidths, the breakdown into homogeneous and inhomogeneous linewidths needs to be systematically compared for different types of fluorine containing compounds.

The ^{19}F containing compounds were classed into one of five groups.

1. Systems where ^{19}F-^{19}F dipolar couplings dominate and contain no aromatic rings, such as inorganic fluorides. Compounds such as potassium fluoride (KF) and calcium fluoride (CaF_2) form crystal structures with cubic symmetry. The anisotropy of the bulk magnetic susceptibility (ABMS) is then negligible.
2. Systems where ^{19}F-^{19}F dipolar couplings dominate and contain aromatic rings. Here there will be significant ABMS contributions associated with stacking of aromatic rings.
3. Systems dilute in ^{19}F with aromatic rings. Here there will also be ^{19}F-^{1}H dipolar coupling.
4. Systems dilute in ^{19}F without aromatic rings
5. Samples with the fluorine present as a CF_3 group. These have their own separate group due to the rapid motion about the carbon bond. This rapid motion will mean that the dipolar couplings, both homo and heteronuclear, observed by each ^{19}F nucleus will be strongly averaged.

5.2 Homogeneous versus inhomogeneous linewidth.

The homogeneous linewidth can be defined in terms of the "T_2" measured by fitting the decay of the magnetisation in a spin echo experiment to an exponential decay. If the lineshape is not

exactly Lorenztian, this will not be perfect, but the trends obtained should be still be meaningful. The homogeneous linewidth is related to T_2 by the following equation:

$$\text{Homogeneous full width at half height} \quad = \quad 1/\pi T_2$$

Equation 8

The inhomogeneous linewidth is termed as the linewidth that is non-refocusable in spin-echo experiments, and makes up the remainder of the measured linewidth. Unlike the homogeneous linewidth this will not be averaged out by MAS and will still have a contribution at infinite spinning rate. The two main factors that lead to inhomogeneous line broadening are chemical shift distributions, and the anisotropy of the bulk magnetic susceptibility (ABMS) which is discussed in more detail later in this chapter.

5.3 Bloch-Siegert shifts

One complication with acquiring ^{19}F NMR spectra in the presence of ^{1}H decoupling is the similarity of the gyromagnetic ratio in comparison to ^{1}H (~94%). This similarity of NMR frequencies can result in significant "Bloch-Siegert shifts"[1]. This is an apparent shift of the acquired nucleus resonance frequency, when an RF field is being applied at a different, but similar frequency. The exact Bloch-Siegert shift can be determined from the following equation

$$\Delta = \frac{\left(\gamma_{obs} B_1\right)^2}{\left(\omega_0^2 - \omega^2\right)}$$

Equation 9

where γ_{obs} is the gyromagnetic ratio of the observed nucleus, B_1 is the decoupling field, ω_o is the Larmor frequency of the observed nucleus (angular frequency units), and ω is the Larmor frequency of the decoupled nucleus[2]. **Equation 9** shows that the Bloch-Siegert shift is proportional to the square of the decoupling field, B_1 and inversely proportional to the difference between the squared Larmor frequencies of the observed and decoupled nuclei. The equation shows that Bloch-Siegert shifts could be significant for ^{19}F while decoupling ^{1}H, in comparison to other nuclei such ^{13}C, due to the similarities in their NMR frequencies.

The Bloch-Siegert effect can be highlighted by varying the power of the ^{1}H decoupling applied (see **Equation 9**), with the ^{19}F signal detected. The difference in the chemical shift is represented by Δ, and is negligible (0.1 ppm) on the 500 MHz spectrometer. For lower field spectrometers this can be a larger problem and high power decoupling can in fact create broader lines. The reason

that the Bloch-Siegert effect leads to broader lines is that as mentioned previously (section 4.3), there is RF inhomogeneity across the rotor. As such the efficiency and hence power of the ^{1}H decoupling will vary through the rotor, meaning the Bloch-Siegert effect will vary depending the position of the sample within the coil. This variable effect will result in the broadening of the lines.

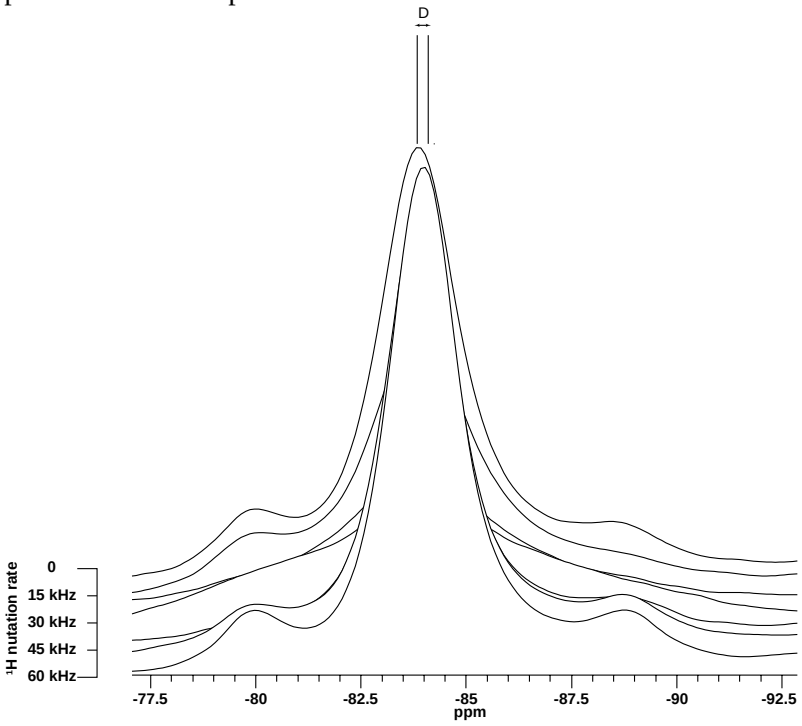

Figure 35 Arrayed fluorine spectrum of AZ6474 compound, with varying ^{1}H decoupling powers applied. We can see that there is a very small shift in the NMR frequency from no power to full power decoupling. Linewidths also get broader for low power decoupling.

Compare this shift (**Figure 35**) with a comparative experiment run on the 300 MHz spectrometer here in Durham. On the 500 MHz spectrometer the overall shift due the Bloch-Siegert effect was around 0.1ppm, while on the 300 MHz the shift was around 0.8ppm with similar decoupling powers.

5.4 Anisotropy of the bulk magnetic susceptibility (ABMS)

ABMS is a contributing factor to the inhomogeneous linewidth, and cannot be removed by fast MAS. Aromatic compounds tend to have larger ABMS values due to the induced magnetic fields created from π-π stacking. The induced magnetic field is not uniform as it is dependent upon the crystal orientation within the applied magnetic field. This results in a shift of the NMR frequency which depends on the crystallite orientation. As discussed in Chapter 5, the ABMS effect can be estimated using *ab initio* calculations of the magnetic susceptibility tensor.

The ABMS contribution has been discussed previously[3] for ^{13}C, including ways in which to reduce the effect. One method was to dilute the compound in a sample that tends to have low ABMS[4]. Previous workers used hexamethylbenzene mixed in adamantane with around a 50:50 mixture. The theory is that the 'solvent' compound surrounds the 'solute' on the molecular level and reduces the interaction from neighbouring 'solutes'. The mixing can be achieved by manual grinding of the sample. This means that the particle size is nowhere near the molecular dilution needed to remove the ABMS contributions completely. However, if molecular mixtures were to be investigated these would no longer correspond to the original materials.

What is important is that the ABMS effect can be reduced by diluting the sample. This could mean that it is actually beneficial for the pharmaceutical companies to work with drug blends. Our initial thought was that this would be difficult due to the insensitive nature of NMR. Due to its high sensitivity in NMR this effect may be useful when working with samples dilute in ^{19}F, i.e. formulated drug products.

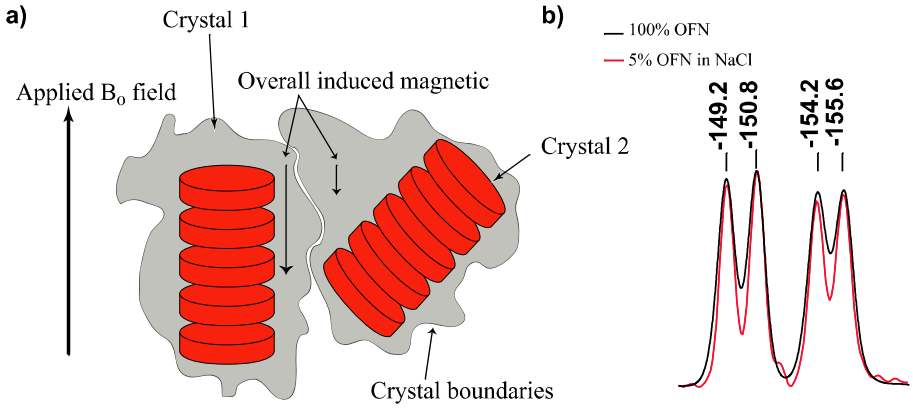

Figure 36 a) Schematic diagram representing how orientation of the crystals within the applied magnetic field affects the bulk magnetic field, where crystal 1 which is parallel with respect to applied magnetic field has a larger induced magnetic field relative to crystal 2. b) Shows how the linewidth for octafluoronaphthalene (OFN) is reduced with the addition of NaCl, which has a low ABMS value.

5.5 Dependence of ^{19}F linewidths on MAS

To determine the contribution to the linewidth that the network of dipolar coupling provides in samples containing fluorine a MAS[5,6] investigation was performed. The homogeneous linewidth due to dipolar coupling is inversely related to spinning speed[7], so at infinite spinning the linewidth theoretically would consist only of an inhomogeneous contribution. For per-fluorinated compounds, where ^{1}H is not an issue, the linewidth should therefore be very dependent upon MAS rate.

A broad sample range of compounds were investigated to see how the inhomogeneous contribution varies from compound to compound. Compounds that have a high inhomogeneous contribution will have a significant difference in between the natural linewidth in comparison to the homogeneous linewidth. To ensure a good understanding of the linewidth the sample range will contain compounds with varying amounts of inhomogeneous contribution.

5.5.1 CaF_2

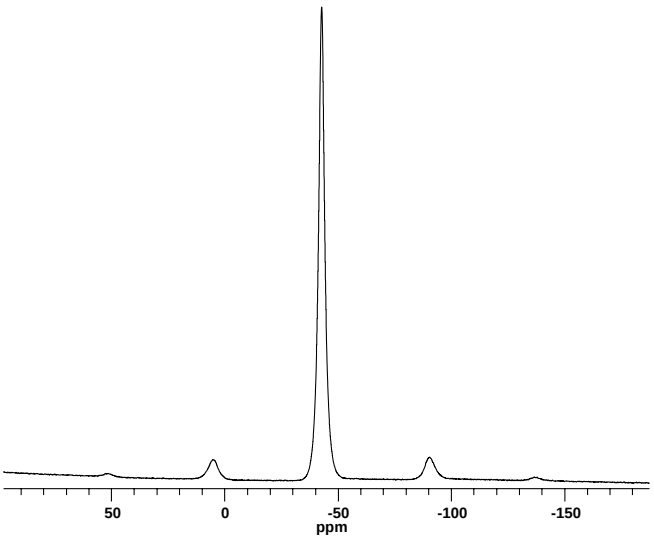

Figure 37 Fluorine spectrum of CaF_2. Due to the symmetry within the compound, there is little to no CSA contribution present, resulting in the spinning side band pattern being symmetric about the central band.

This sample was investigated as it is expected to have a low inhomogeneous contribution due to its high crystallinity (lack of disorder) and high symmetry (negligible ABMS). Note that it has a high density (3.18×10^3 kg/m^3), and so reduced MAS (22 kHz) rates were used to limit the possibility of rotor explosion. The T_2 values are also short (due the strong dipolar couplings), and so along with the reduced spin-rate this made it difficult to accurately measure the value of T_2 as only a small number of points could be taken for the echo before the magnetisation had fully decayed.

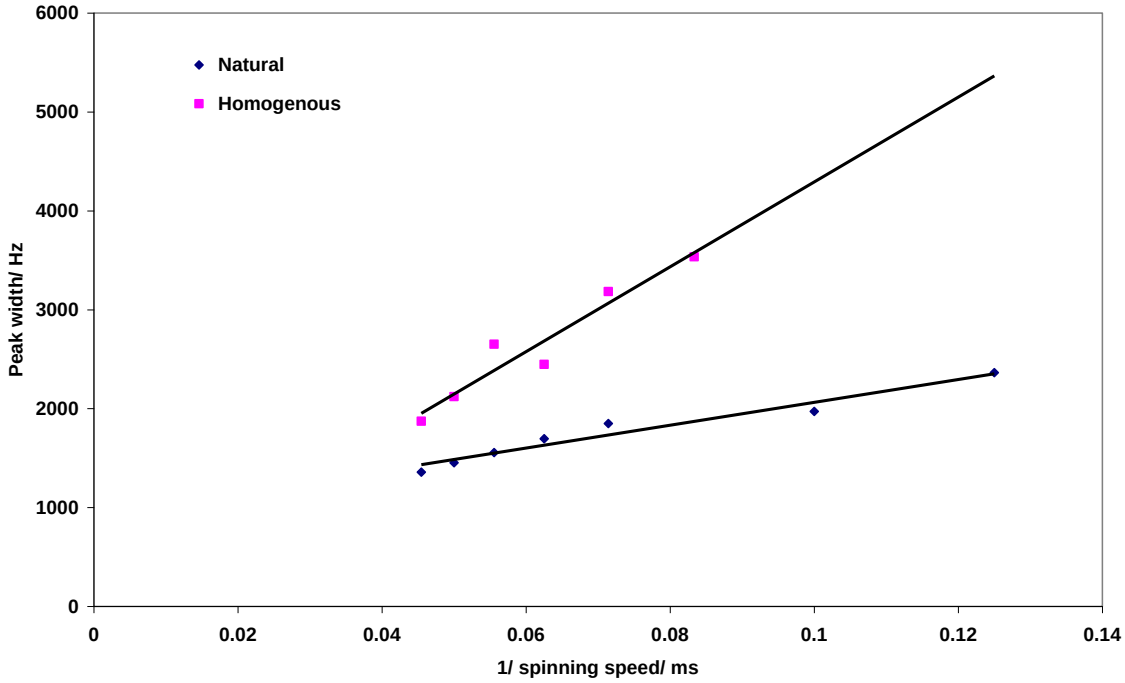

Figure 38 Comparison of 'natural' and homogeneous linewidth with varying MAS rates for CaF_2.

Figure 38 compares the homogeneous linewidth to the 'natural' linewidth with varying spin rates for CaF_2. As mentioned previously the homogeneous linewidth is inversely related to the spin rate and tends toward zero at infinite spinning speed.

There are, however, a number of unexpected features. Firstly the "homogeneous linewidth" is *broader* than the natural linewidth, and secondly the natural linewidth does not obviously tend to zero. This is partly a consequence of the limitation in maximum MAS rate, which makes extrapolation difficult. In addition, the NMR decay is dominated by the dipolar coupling network and is expected to deviate strongly from a simple exponential. This means that the exact "T_2" values (and resulting linewidths) are not particularly meaningful, although the qualitative trends are reasonable.

5.5.2 Teflon

Teflon, which consists of a chain of CF_2 groups was expected to have a large inhomogeneous contribution due to subtle differences in chemical environments for each fluorine site, as is generally the case for disordered materials such as polymers (see **Figure 39**).

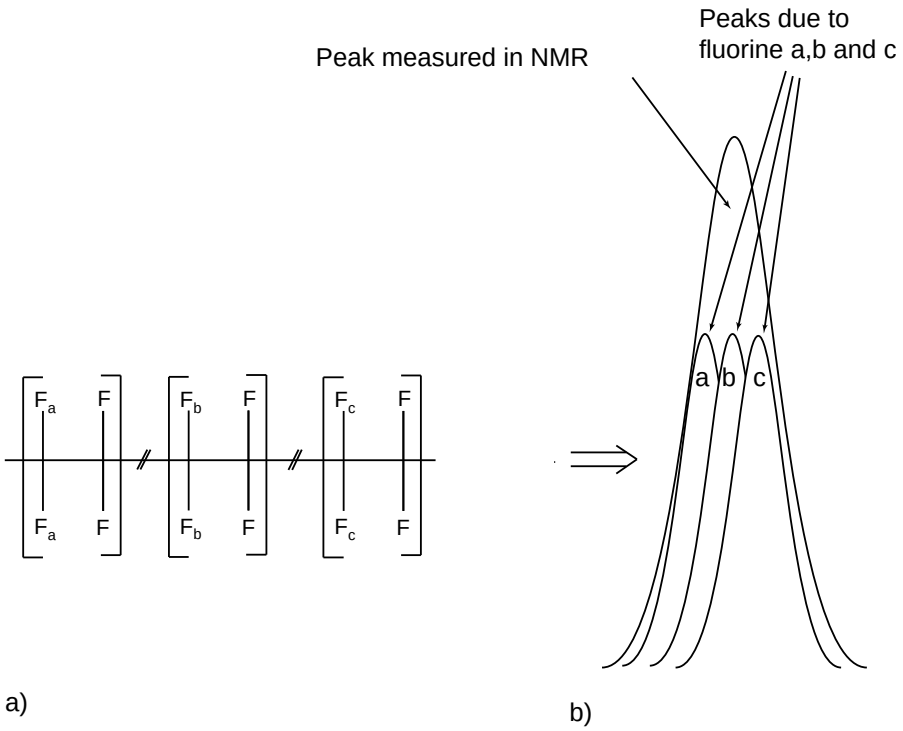

Figure 39 a) Schematic structure of Teflon, representing the disorder within the system, with three sites highlighted for illustration b) shows how these three different sites are subtly different, leading to broadening of the lines.

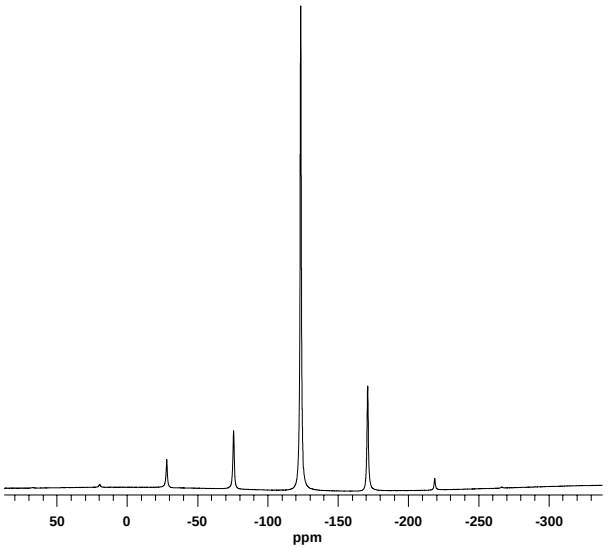

Figure 40 Fluorine spectrum of Teflon. This has a high CSA due to the asymmetric nature of the C-F bond, as can be seen by the asymmetric spinning side band pattern, compare with **Figure 37**

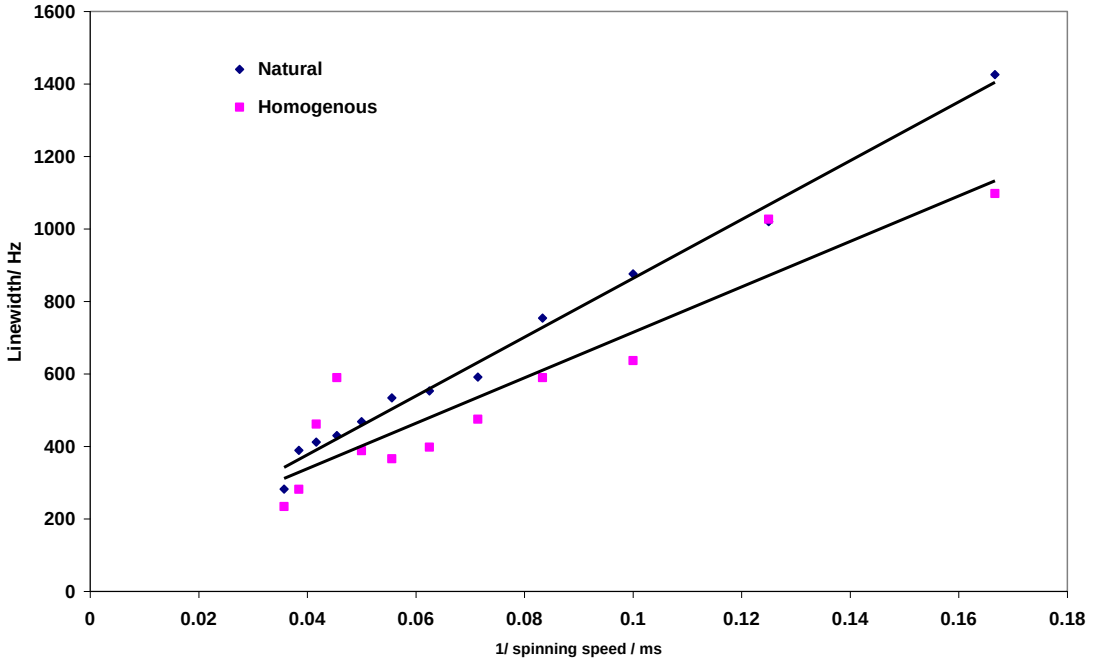

Figure 41 Comparison of homogeneous and natural linewidth for Teflon at varying MAS rates

When it came to measuring the homogeneous and natural linewidth for Teflon an unexpected result was discovered (see **Figure 41**). As mentioned previously it was expected that there would be a significant in-homogeneous contribution present due to the disorder within the system. From the graph it is possible to see that at slow MAS rates there is a significant inhomogeneous contribution of around 400 Hz. For fast MAS (28 kHz) there is now only a small inhomogeneous contribution of around 50 Hz. The inhomogeneous contribution should be unaffected by varying the MAS rate as only dipolar couplings are reduced. One explanation is that as the rotor is spun faster the sample is heated as a result due to friction. This increase in the temperature results in a more rapid motion of the solid, which averages out the chemical shift variation and reduces the inhomogeneous contribution. As for all homogeneous measurements there are the errors associated with fitting the decay, which complicates matters further.

It is obvious, however, that the homogeneous linewidths due to the homonuclear dipolar couplings are the dominant factor, and so resolution improves steadily with increasing MAS rate.

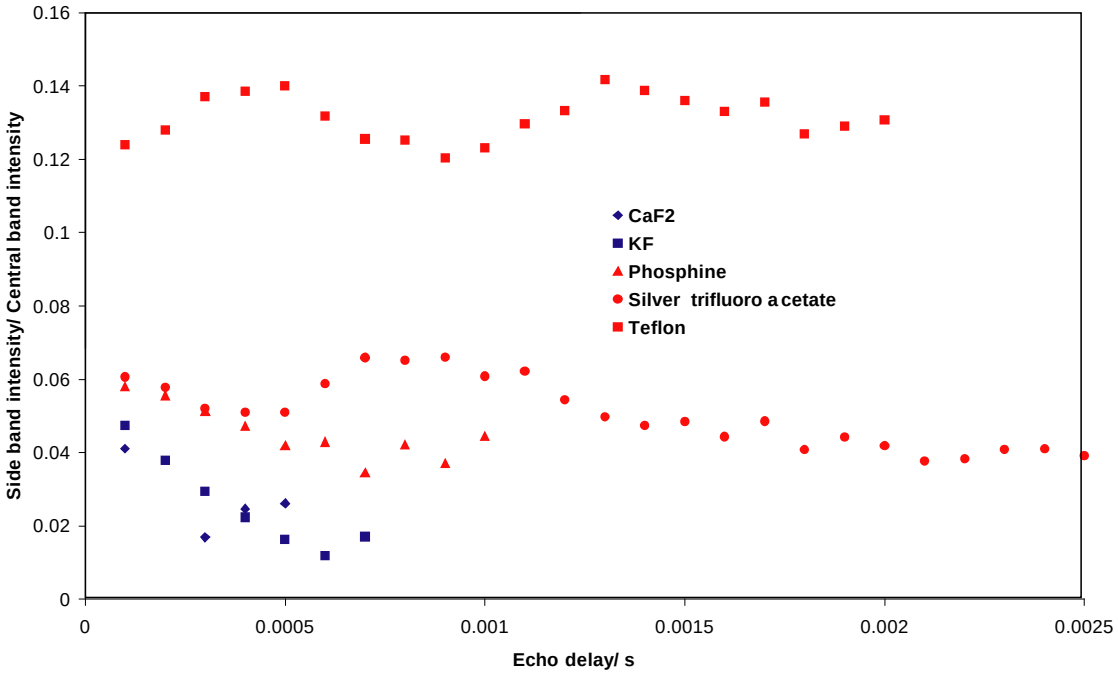

Figure 42 Comparison of spinning side band intensities with respect to the central band in a spin echo experiment for a series of compounds. The oscillation in the echo in particular for the Teflon molecule is a consequence of not using a fully optimised 90º pulse.

The CSA, however, is a very important contributor to the spinning sideband intensities (in comparison to the inorganic fluorides). **Figure 42** shows the relative intensity of sideband to centreband for systems where the CSA is large e.g. Teflon and small e.g. KF. Where the CSA is important, the sideband to centreband ratio tends to be approximately constant. Where sidebands are dominated by the homonuclear couplings, the sidebands tend to decay more quickly than the centreband and so the sideband/centreband ratio tends to decrease steadily with increasing echo time.

5.5.3 Octafluoronaphthalene (OFN)

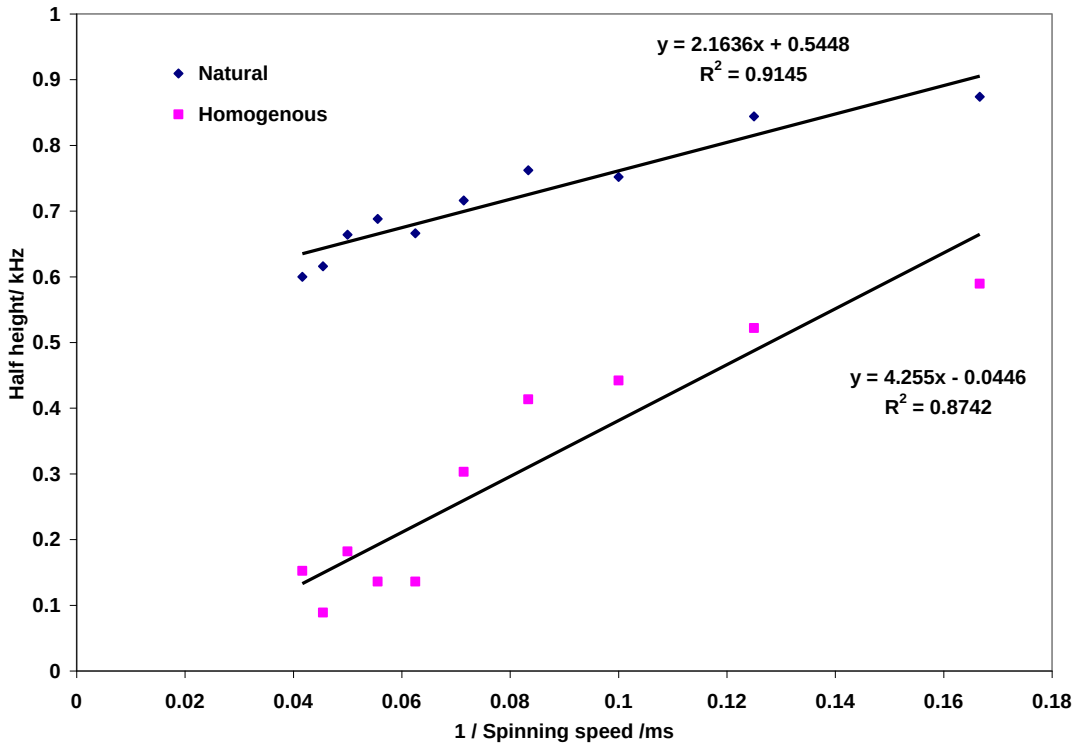

Figure 43 Comparison of 'natural' and homogeneous linewidth for OFN.

Compounds with aromatic rings tend to have a larger inhomogeneous contribution due to the ABMS. This can be clearly seen for OFN in **Figure 43**, where the measured linewidth is far greater than the homogeneous contribution. Even with very fast MAS the linewidths are typically broad (~600 Hz) due to the inhomogeneous contribution. This can not be averaged out with spinning and hinders resolution, especially when the peaks have similar chemical shifts and overlap as in the case of OFN.

As already noted in **Figure 36** (b) the linewidth for octafluoronaphthalene (OFN) can be reduced by the dilution with a compound with negligible ABMS. A series of concentrations of OFN in NaCl were made up and the resulting linewidths were recorded (see **Figure 44**).

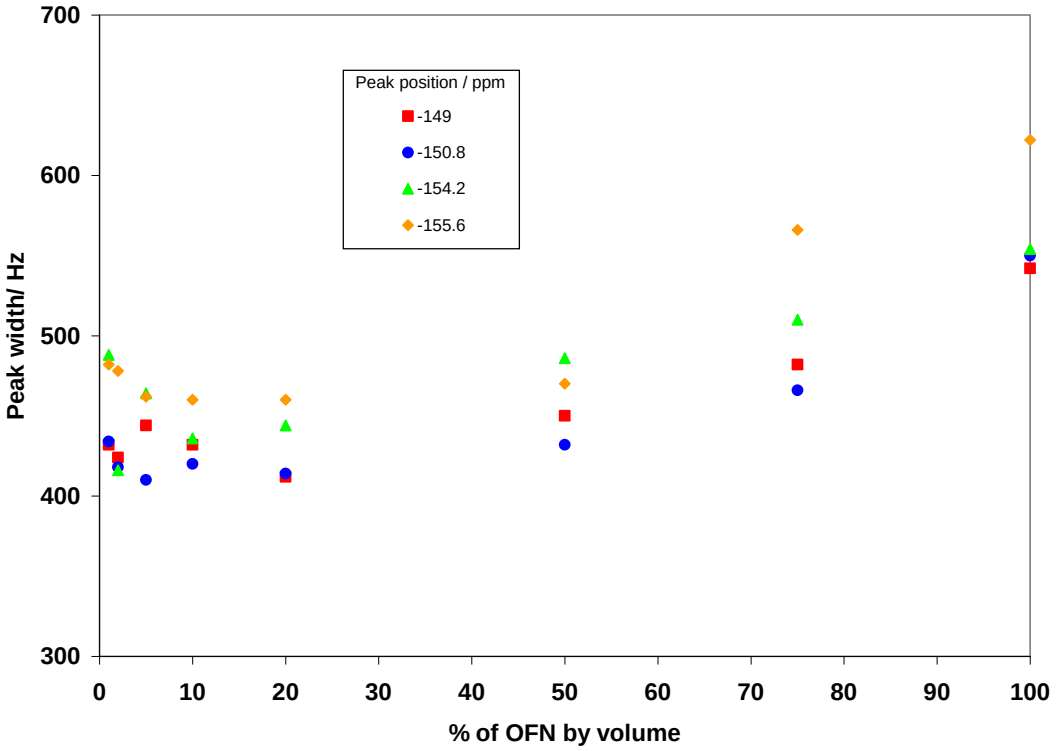

Figure 44 Plot of dependence of linewidth upon OFN concentration. The linewidth reduces as the OFN content is reduced until a plateau is reached at around 50%.

From the plot of the measured linewidth and concentration of OFN present, it is possible to see that as the OFN concentration decreases, a significant reduction in linewidth is seen (~150 Hz). The linewidth gradually decreases on addition of NaCl until a plateau is reached at around 50%. This clearly shows that the effect of the ABMS on the overall linewidth can be reduced significantly by the addition of a sample with a low ABMS value. There is apparently a small increase in the measured linewidth at low OFN concentrations. This may be due to poor signal-to-noise ratio at the low concentrations.

One explanation for linewidth reaching a plateau at the lower concentrations of octafluoronaphthalene is that the samples were mixed with manual grinding, meaning large crystal boundaries are still present, which contribute to ABMS. As noted above, molecular level dilution would avoid this residual broadening, but fundamentally changes the structure of the material.

5.5.4 Tris (p-trifluoromethylphenyl) phosphine

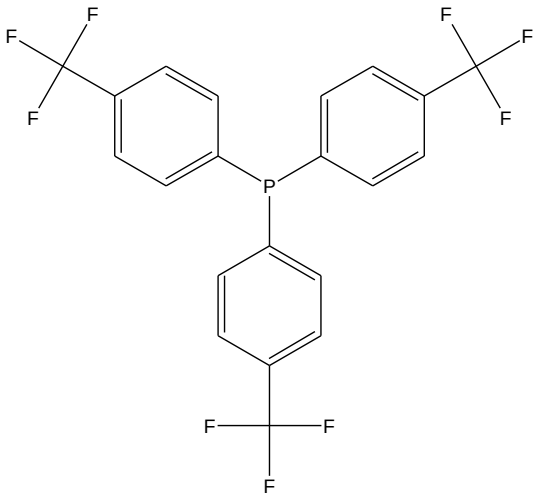

Figure 45 Structure of Tris (p-trifluoromethylphenyl) phosphine

Not all aromatic compounds have a large inhomogeneous contribution however, as it also depends on their crystal packing; the ABMS contribution is large if the aromatic rings are systematically layered within the crystal as for OFN. An example of an aromatic containing compound with a low ABMS contribution is tris (p-trifluoromethylphenyl) phosphine (see **Figure 46**). The molecule is relatively bulky which hinders effective π–π stacking of the aromatic rings, reducing the ABMS.

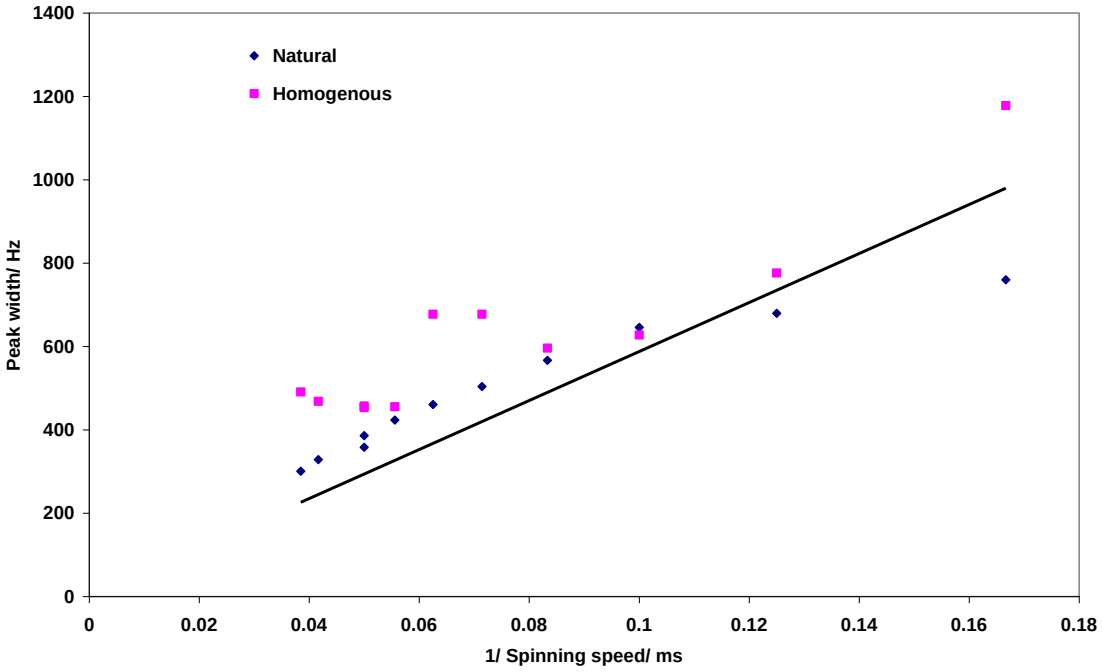

Figure 46 Comparison of homogeneous and natural linewidth for tris (p-trifluoromethylphenyl) phosphine.

As for CaF_2 the homogeneous linewidth for tris (p-trifluoromethylphenyl) phosphine tends to be broader than the natural linewidth (see **Figure 46**), which suggest there is a negligible inhomogeneous contribution for this system. Again the limitations of fitting the magnetisation decay in the spin-echo to a simple exponential may explain why the homogeneous linewidth often appears to be greater than the overall natural linewidth.

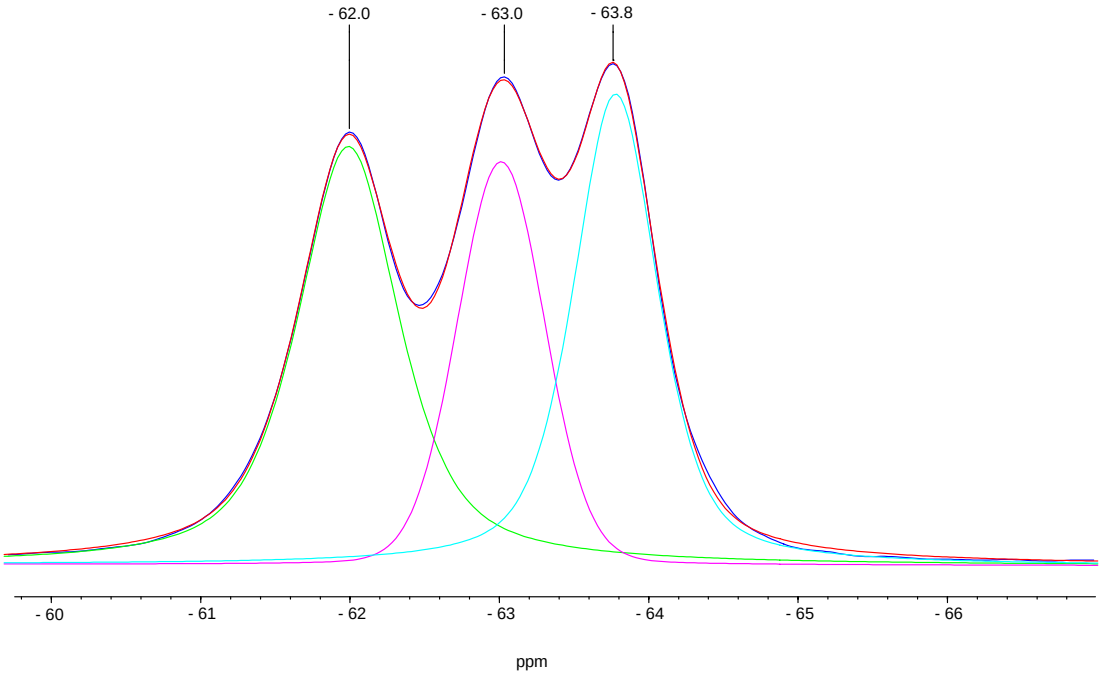

Figure 47 Spectrum of tris (p-trifluoromethylphenyl) phosphine at 26 kHz, even at fast MAS the peaks are not fully resolved and makes measuring the linewidth more complicated.

The line fitting is more complicated for tris (p-trifluoromethylphenyl) phosphine as the peaks are not fully resolved (see **Figure 47**). The peak width had to be measured with a suitable deconvolution package. By doing so the Lorenztian/Gaussian ratio can also be measured, in this case it was around 50% for each peak. This explains why the decay of intensity in a spin-echo experiment does not fit a single exponential in this case.

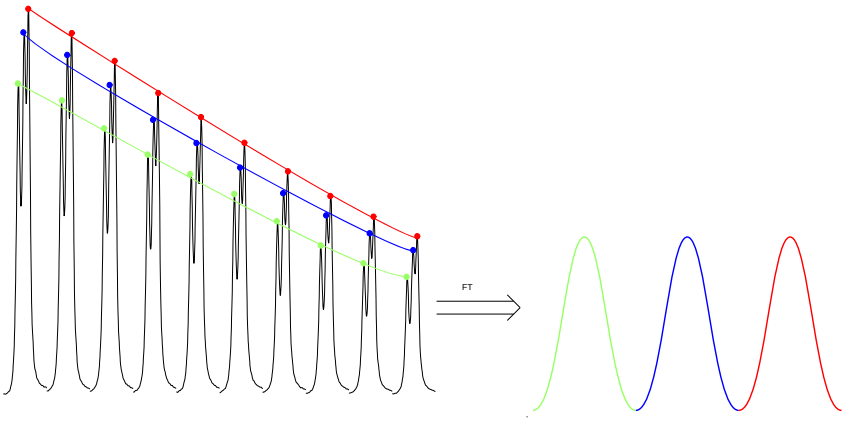

Figure 48 Diagram to explain how the echo is Fourier transformed. First the intensities for each peak at each time are measured and the resulting decay is Fourier transformed to give a single peak. The width of this peak gives to the homogeneous linewidth.

Performing a Fourier transform would allow for the lineshape having a composite function as opposed to a single function, see **Figure 48**. In practice, however, the linewidths of the Fourier transform of the spin echo were comparable to that of the fitted exponential. Even though the linewidth is slightly broader for the homogeneous than the measured linewidth the point is that this compound has little to no inhomogeneous contribution. On the addition of NaCl the natural linewidth remained unchanged even when the compound was present in very small amounts. The reason the overall linewidth remained unchanged was that the ABMS was making little or no contribution in this case. Addition of the NaCl only reduced the sensitivity of the system and no increase in the resolution was seen.

5.5.5 Silver trifluoroacetate

There was one case where there was a significant inhomogeneous contribution even though there were no aromatic rings present. The compound in question was silver trifluoroacetate (see **Figure 49**) and there was constantly around 700 Hz of inhomogeneous contribution at all spinning speeds.

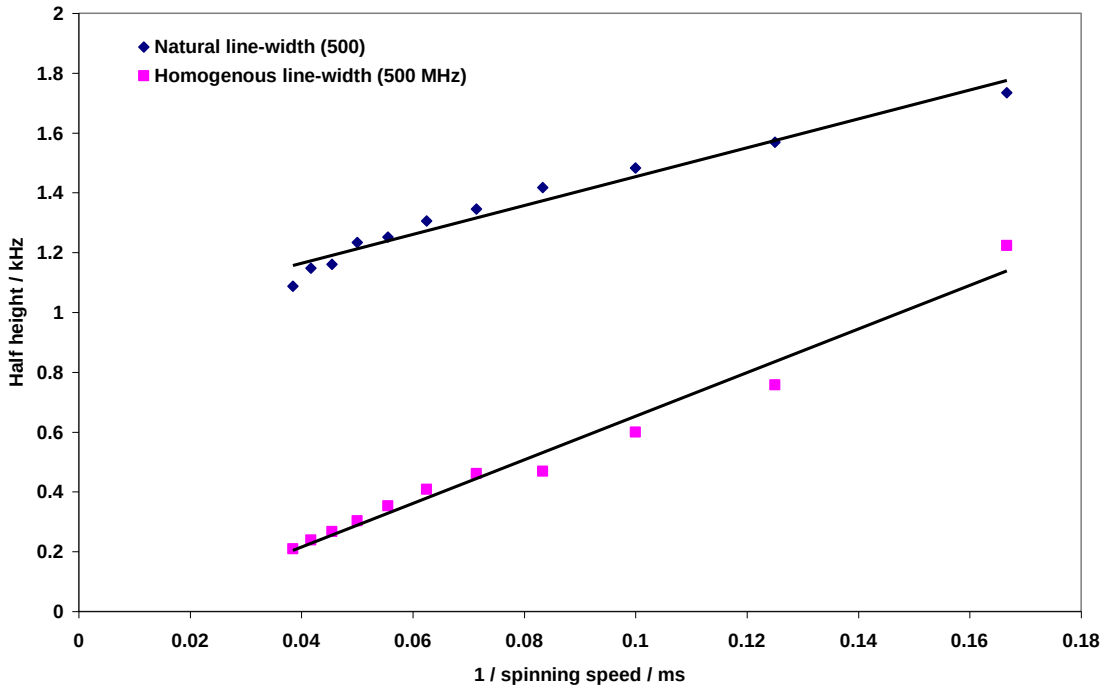

Figure 49 Comparison of homogeneous and measured linewidth for silver trifluoroacetate

It is unclear why there is such a large inhomogeneous contribution for this compound, no further work was performed to investigate this effect due to the atypical nature of the compound and lack of pharmaceutical relevance.

5.5.6 Dependence of ^{19}F linewidths on MAS: Conclusions

The results for the per-fluorinated systems showed that for systems with large homogeneous contributions, the most efficient method to reduce linewidths is by fast MAS. This is similar to ^{1}H NMR where the resolution of the lines are only limited to the maximum MAS rate of the probes and indirectly the strength of the applied magnetic field.

The work on the per-fluorinated systems also highlighted how the inhomogeneous contribution varied for compound to compound. The inhomogeneous contribution in general remains constant for all MAS rates and can not be removed with MAS alone.

The strong sample dependence of ABMS is shown in **Figure 50**, where the ^{13}C linewidth was investigated as a function of concentration of NaCl (data supplied by Dr. David Apperley of Durham). Once again the linewidth was reduced as for OFN however this time the linewidth dropped off rapidly at low concentration. If the ^{13}C spectrum had been taken for OFN, it is expected the reduction in linewidth would be the same as for the fluorine case. This was not

possible due to the need to decouple the ^{19}F, and also the poor sensitivity of ^{13}C in comparison to ^{19}F.

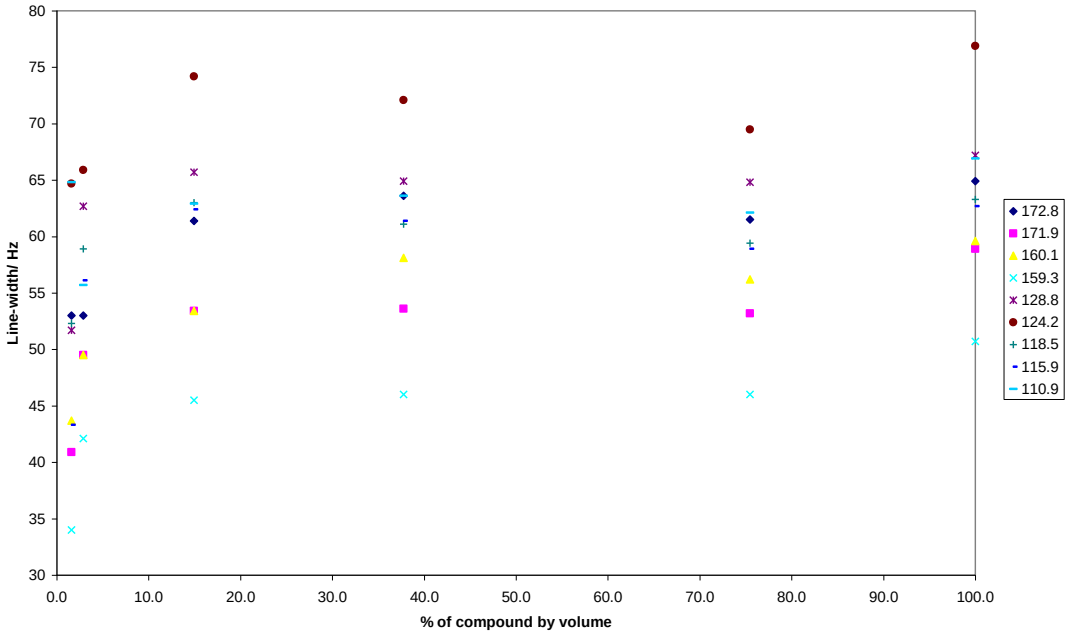

Figure 50 Effect on linewidth when diluting a steroid sample with NaCl

5.6 Field dependence on linewidth

Experiments were performed on two different spectrometers, a 200 MHz spectrometer as well as a 500 MHz spectrometer. This is to see how the inhomogeneous and the homogeneous linewidth are affected by different fields. The homogeneous linewidth is expected to remain constant as it is due to dipolar coupling and should not be affected by the applied magnetic field. The inhomogeneous linewidth is expected to be directly proportional to the applied magnetic field. This should result in an increase of around 150% for the inhomogeneous contribution on the 500 MHz spectrometer.

Only per-fluorinated compounds will be investigated on the 200 MHz spectrometer, as there are no probes that can be tuned to both ^{19}F and ^{1}H simultaneously. The 2.5mm probe from the 500 MHz was used and the fluorine will be detected on the X channel. This makes it impossible to apply ^{1}H decoupling to the system while detecting ^{19}F.

Two of the per-fluorinated compounds were run on the 200 MHz spectrometer as a comparison. These compounds were silver trifluoroacetate, and Teflon. These two compounds were used as they exhibit significantly different chemical characteristics.

Below is a graph (**Figure 51**) summarising the data acquired for silver trifluoroacetate on both the 200 MHz and 500 MHz spectrometer. On both occasions the 'natural linewidth as well as the homogeneous linewidth were measured. In order to make a fair comparison the overall linewidth had to be measured due to the reduced resolution at low field and low MAS rates. As a result the inhomogeneous linewidth is the overall contribution for all three ^{19}F sites.

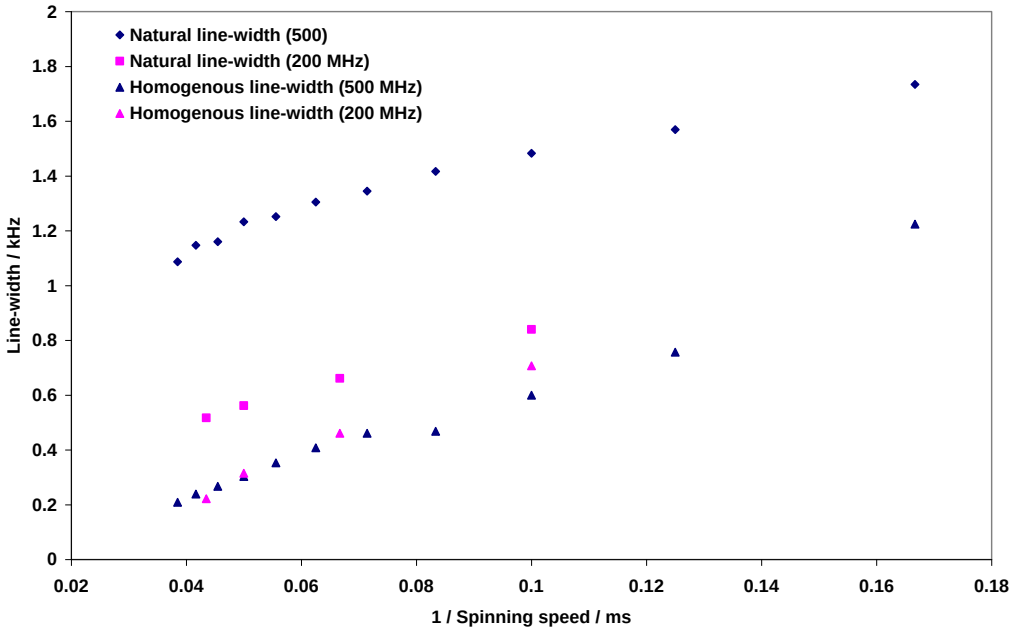

Figure 51 Comparison of the 'natural' and homogeneous linewidth, when acquired on spectrometers with varying applied magnetic field strength for silver trifluoroacetate.

From the graph it is clear to see that the homogeneous linewidth as expected is the same at both field strengths. What is different is the inhomogeneous contribution for the two spectrometers. For the 200 MHz spectrometer there is an inhomogeneous contribution of around 300 Hz (1.6ppm), at the faster spinning rates, which in comparison to 800 Hz (1.7 ppm) for the 500 MHz spectrometer. Although there is a significant difference in the inhomogeneous contribution, the linewidths are comparable in the ppm scale.

The ratios of the inhomogeneous contribution for the two spectrometers are also comparable to the ratio of their field strengths as expected. In order to confirm this, the same experiment was performed for a system with a low inhomogeneous contribution (Teflon). In this case the natural linewidth using the two spectrometers was very similar.

5.7 Decoupling investigation

In order to be able to fully understand the effect of the linewidth upon both the homogeneous and the measured linewidth an investigation into ^{1}H decoupling needs to be under taken. The understanding of the contributing factors to measured linewidths are only partially understood for cases where NMR signals are acquired in the presence of ^{1}H decoupling[8,9]. The influence of ^{1}H decoupling on ^{19}F spectra is even less well understood, providing the motivation for the current study.

Decoupling of ^{1}H while acquiring on ^{19}F is complicated by the similar gyromagnetic ratios of the nuclei. In order to overcome this problem probes have special circuitry which enables good isolation between the two channels. This is usually termed a 'trap' and needs to be optimised before any experiment. The technique is complicated further by the Bloch-Siegert[1,2] effect, which tends to be more of an issue for low field work.

The most basic form of decoupling is CW, where a constant RF power is applied to the ^{1}H channel. The ^{1}H magnetisation precesses at a constant rate dependent on the RF power. For continuous wave (CW) decoupling only the power can be varied, and it is expected that the linewidth will reduce as decoupling power is increased. Problems may arise when the MAS rate is a multiple of the nutation rate of the ^{1}H decoupling[9].

Decoupling efficiency is limited by the probes specifications on the maximum powers that can be used without causing breakdown ("arcing"). To improve the decoupling new pulse sequences have been developed, where the phase of the decoupling is modulated at a constant rate throughout the decoupling sequence. Significant increase in resolution and hence signal to noise are usually seen.

Two other decoupling methods will be investigated, both involving phase modulations. One decoupling method involves the phase being modulated at regular intervals (TPPM)[10-12] (see **Figure 52**). The second decoupling method involves a more complex modulation pattern (SPINAL-64)[13]. In SPINAL-64 decoupling (see **Figure 53**) there is only one variable that can be investigated, the tip angle. Previous work[14] has shown that a tip angle of about 170° proves to be optimal. As for TPPM decoupling, the tip angle will be varied to see how this affects the spectrum.

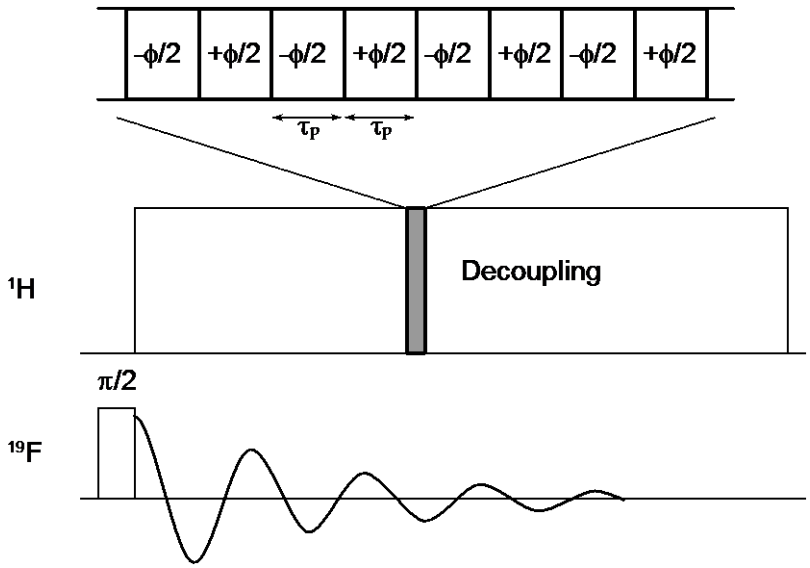

Figure 52 Pulse sequence for TPPM decoupling. The phase of the ^{1}H decoupling RF is flipped at regular intervals (τ), by constant angle (ϕ).

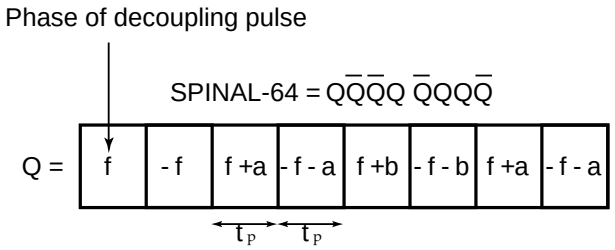

Figure 53 As for TPPM, SPINAL-64 decoupling involves a phase modulation. Unlike in TPPM decoupling, the phase switch for SPINAL-64 is more gradual and improves the resolution even further

Another method of decoupling for use at high spinning speeds (greater than 20 kHz) is X inverse X (XiX)[15] decoupling. As for TPPM and SPINAL, XiX decoupling involves phase modulation in the applied decoupling pulse. There are two significant variations between XiX and other phase modulated decoupling sequences. For XiX decoupling the modulation is far greater than for decoupling sequences such as TPPM, as a phase modulation of 180º is used in comparison to around 15º for TPPM. The time between the frequency modulation, i.e. the tip angle is far greater for XiX in comparison to TPPM decoupling. The time between the modulations are in the region of milliseconds, with the length being correlated with the MAS rotor period.

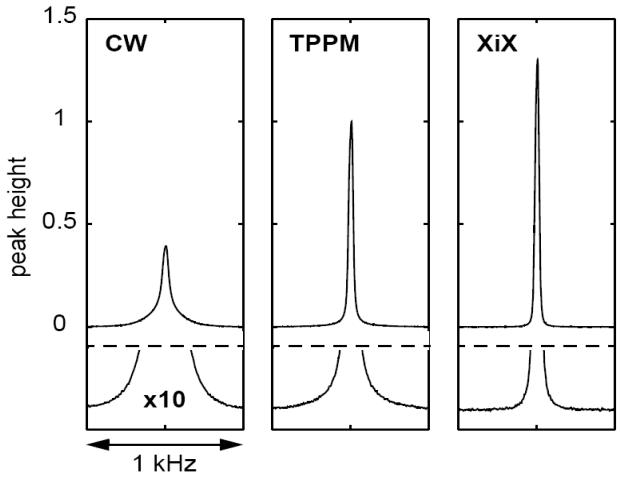

Figure 54 Comparison of optimised decoupling forms for crystalline alanine with ^{1}H decoupling 150 kHz and MAS rate of 30 kHz[9]

In general the signal to noise of the system is improved for XiX in comparison to TPPM and SPINAL at fast MAS (see **Figure 54**). The resolution however is not improved greatly, and the linewidth at half height remain fairly constant. The improvement in intensity comes about by the variation of the lineshape[8], with the peaks having less of a 'tail' in the 1D spectrum. The main advantage of XiX over TPPM is there is only one variable, the tip angle, this makes it easier when it comes to optimise the process. The problem though is we need to use the 4 mm probe as this is the only probe with separate ^{19}F and ^{1}H channels, as a result fast spinning is not an option and XiX can not be used.

To investigate the decoupling, both the measured linewidth and the homogeneous linewidth will be investigated. It is hoped that the effect of the re-focused linewidth is better understood in its contribution on the measured linewidth. The effect of varying the TPPM parameters will be investigated by incrementing both the tip angle and the phase of the decoupling. The efficiency of the decoupling will be measured by recording the peak intensity for each parameter set. The homogeneous linewidth will be optimised within a spin-echo by having a sufficiently long τ value and trying to maximise the signal for that τ value. Once a maximum has been found a full spin-echo will run and the T_2 value can be measured. Form here it will be possible to see how the homogeneous and inhomogeneous linewidth is affected by variable TPPM decoupling parameters.

5.7.1 Simulation of ^{1}H decoupling while acquiring ^{19}F spectra

To get a better understanding of how ^{19}F linewidths behave on the application of decoupling they were compared to ^{13}C lines, both experimentally and in simulations.

The simulations were performed on an in-house simulation program, pNMRsim. The program relies on a periodically repeating system to speed up the calculations. We are using this approach as a way to deal with large spin systems and the details of the simulations are not directly relevant. For a more in-depth description of the simulation methodology see Refs 16 and 17. The chosen "unit cell" contained one fluorine and two protons (see **Figure 55**). The distances and angles apart are determined from the crystal structure. The distance the cells are apart is again determined by the distance the fluorine nuclei are apart. There are only three cells, containing in a total of 9 spins needed for accurate calculation as periodic boundary conditions reduces "edge effects". This cuts down calculation times down by an order of magnitude and has shown to produce good agreement with experimental data[16,17].

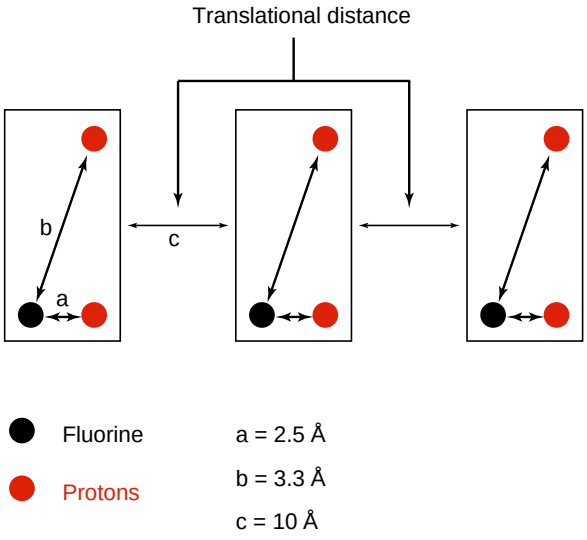

Figure 55 Schematic diagram showing setup of simulation of crystal structure for a fluorine containing compound.

In order to get a better understanding of the important factors when applying ^{1}H decoupling, the simulations were also repeated for ^{13}C. The setup for the simulation was the same as for ^{19}F, only this time the distances and angles were measured from the ^{13}C to the ^{1}H. This would show whether it was theoretically more difficult to decouple ^{1}H when acquiring on ^{19}F as opposed to ^{13}C. When calculating the heteronuclear dipolar couplings for both ^{13}C and ^{19}F it was apparent that couplings between ^{19}F and ^{1}H were considerably smaller than those between ^{13}C and ^{1}H. Even though ^{19}F has a gyromagnetic ratio around four times as great as ^{13}C, the average ^{19}F-^{1}H distances are far greater.

The simulations were plotted in a 2D format and the results can be seen below (see **Figure 56**).

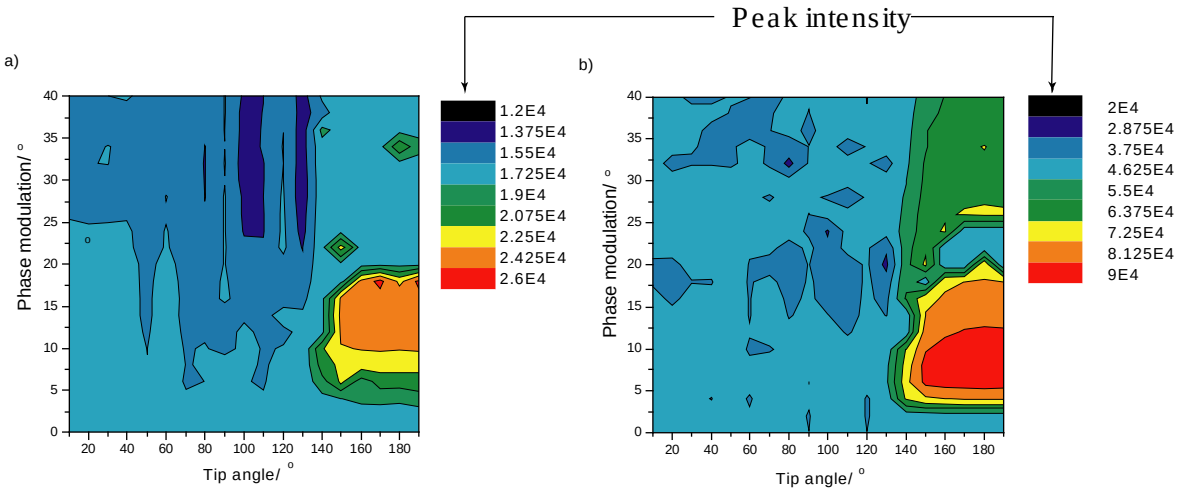

Figure 56 Plot of peak intensity with respect to variable TPPM conditions for a) ^{13}C detection with ^{1}H decoupling b) ^{19}F detection with ^{1}H decoupling, where the key indicates the peak intensity for each decoupling combination.

From the simulations (see **Figure 56**) it is possible to see how efficient TPPM decoupling is in comparison to CW decoupling. This can be seen when the phase angle is zero, which corresponds to CW decoupling. The simulations also show very clearly the relatively small area where efficient decoupling is obtained. In simulation a), maximum intensity is obtained for a phase shift of 15º and a tip angle of ~170º, which agrees with previous work[14].

The overall structure and decoupling efficiencies shown in (a) and (b) are very similar. This shows that ^{1}H decoupling is no more difficult for ^{19}F than for ^{13}C, and the optimal parameters in the two cases are very similar.

5.7.2 Betamethasone-17-valerate

The model compound must have little or possibly no aromaticity, to reduce the contribution due to ABMS. Initial work investigated the compounds supplied by AstraZeneca, which showed a small improvement on application of ^{1}H decoupling, but this was not sensitive enough to the variation of the TPPM parameters. The reason there was only a marginal improvement in switching decoupling schemes was that the ^{19}F was present in a CF_3 group. As mentioned earlier CF_3 groups will have relatively weak ^{1}H-^{19}F dipolar couplings, due to the rotation about the carbon bond and the distance between the two nuclei.

In the end the compound that was used to investigate the decoupling was betamethasone-17-valerate, due to it having very little aromaticity and the ^{19}F present as a simple fluorine bonded onto a cyclic ring. The only problem is due to the limited motion within the compound the T_1 value is relatively long, leading to pulse delays of 300 s.

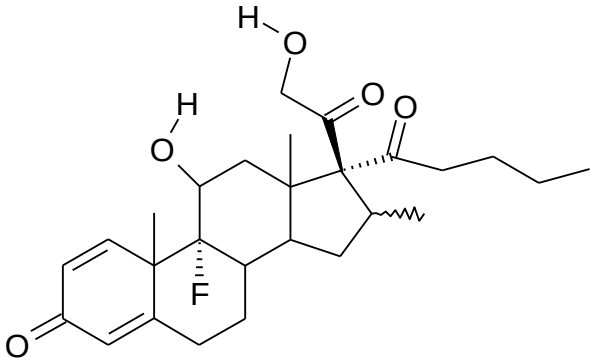

Figure 57 Structure of betamethasone-17-valerate

This molecule was used to investigate and compare the three main types of decoupling available at moderate MAS, with CW, TPPM and SPINAL-64 decoupling. Previous work[18] has shown that the linewidth is sensitive to the decoupling parameters selected, and also shown that ^{1}H decoupling is important for observation of ^{19}F signal for this compound. This compound is sensitive to the ^{1}H decoupling applied as there are nine ^{1}H's within close proximity (around 4 Å) of the fluorine nucleus, which relates to a total dipolar coupling of around 8kHz, which is more comparable to that of the couplings present in a ^{13}C-^{1}H bond.

Due to the relatively large heteronuclear dipolar couplings between the ^{1}H-^{19}F it is essential that ^{1}H is applied. When no decoupling is applied the ^{19}F linewidth is exceptionally broad (~2600Hz), but is reduced significantly to 450 Hz with relatively modest ^{1}H decoupling (62.5 kHz). When the power was arrayed from high to low, the peak width gradually increased from 450 Hz to a maximum of around 6 kHz, on further reduction the linewidth then reduced slightly to 2.6 kHz. Arraying the power on the ^{1}H decoupling did result in a slight variation in the chemical shift due to the Bloch-Siegert effect as mentioned previously.

In order to make a fair comparison of all the decoupling methods it was necessary to optimise the TPPM method, both the phase modulation as well as the tip angle. It was decided not to try to optimise the phase shifts for SPINAL, and focus on the tip angle as this is a more efficient use of time. Other workers[13,14] have optimised the phase shift parameters for SPINAL and these optimal values will be used for the decoupling investigation.

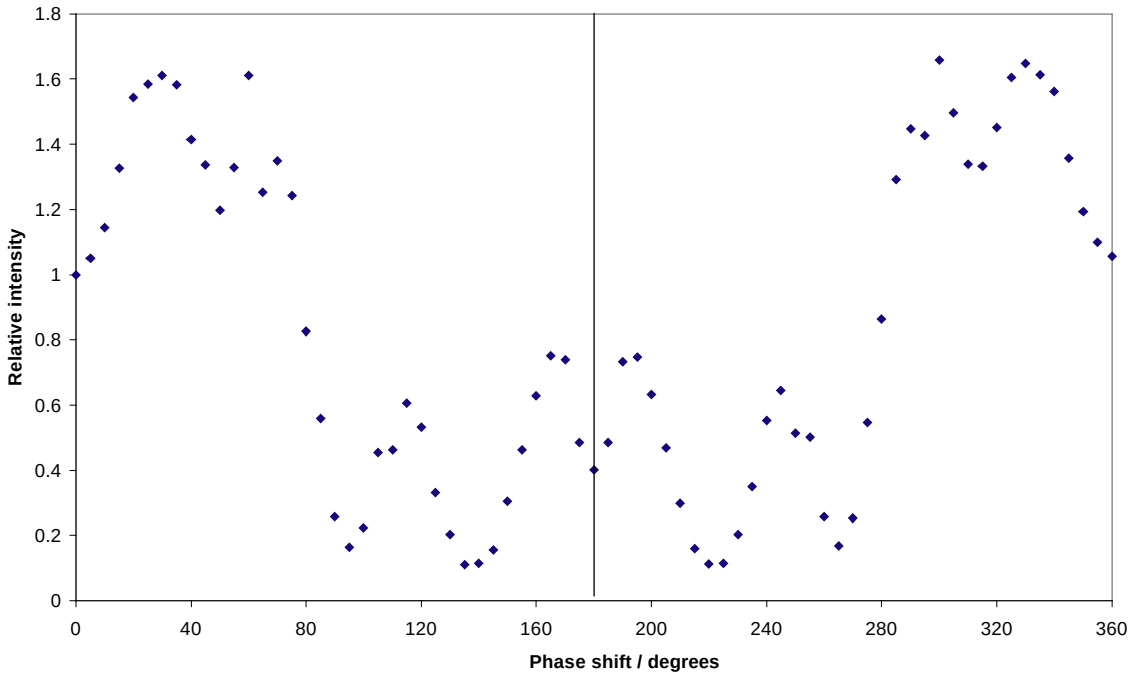

Figure 58 Effect of varying the phase angle for TPPM at 14 kHz MAS and 62.5 kHz ^{1}H decoupling, the intensity is plotted relative to CW decoupling.

Using the betamethasone-17-valerate compound initial testing focused on optimising the TPPM decoupling. A tip angle of 170º was used as previous work[13] has shown this to be a suitable value. A large array was performed in order to map out the effect of varying the phase modulation.

From the results where the TPPM efficiency is plotted relative to CW decoupling (see **Figure 58**) a very clear pattern can be seen. There is almost a factor of two increase in intensity in comparison to CW for this compound. The decoupling pattern is symmetric about 180º, where a minimum in intensity is observed. Although there is a minimum when the tip angle was 180° it was not unexpected as the conditions used were not suited for XiX decoupling. The decoupling sequence had been set up for TPPM decoupling, which is significantly different than for XiX. Also the MAS rate used was 14 kHz, which is far from the fast rates that are required for XiX.

The symmetry about the tip angle of 180° was expected, as in essence the phase shift will be the same. The results do clearly show that for TPPM it is worth spending the time optimising the conditions, as otherwise the decoupling could be far poorer than basic CW decoupling. Once the decoupling had been optimised these conditions can be used for any compound assuming the same RF powers are used for the ^{1}H decoupling.

Now that the TPPM phase modulation has been optimised, it was necessary to compare the efficiency with respect to SPINAL-64 decoupling. As mentioned previously only the tip angle will

be investigated for SPINAL-64 decoupling, with the phase modulation set to parameters used by previous workers[13].

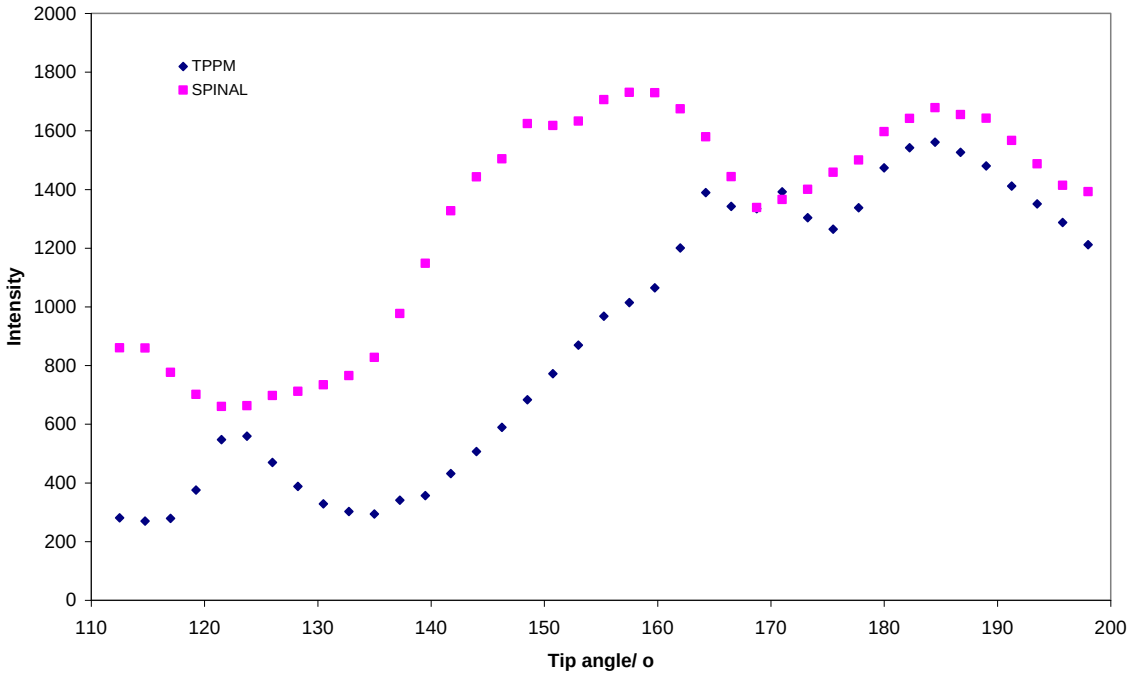

Figure 59 Comparison of decoupling performance for TPPM and SPINAL decoupling on betamethasone-17-valerate.

From the results (see **Figure 59**) it is clear to see that SPINAL-64 decoupling has a constantly better performance compared to TPPM. Not only is it able to increase the intensity in comparison to TPPM decoupling, it is less sensitive to variation of the tip angle. Varying the tip angle from 143º to 193º results in little variation in the intensity. While for TPPM moving away from the optimum conditions results in a rapid tail of in the intensity.

Not only is SPINAL-64 more efficient at decoupling than TPPM is easier to setup also. The ease of optimisation not only means that experiments are shorter when using SPINAL-64 but the time taken setting up experiments is also reduced in comparison to TPPM.

5.7.3 Effect of decoupling on non-refocusable linewidth

The term homogeneous linewidth can no longer be used when decoupling is applied, as it is not fully understood what the spin echo experiments now measures. Instead, the term is substituted for "non-refocusable linewidth".

a)

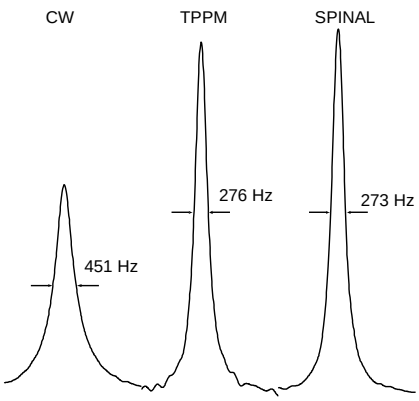

b)

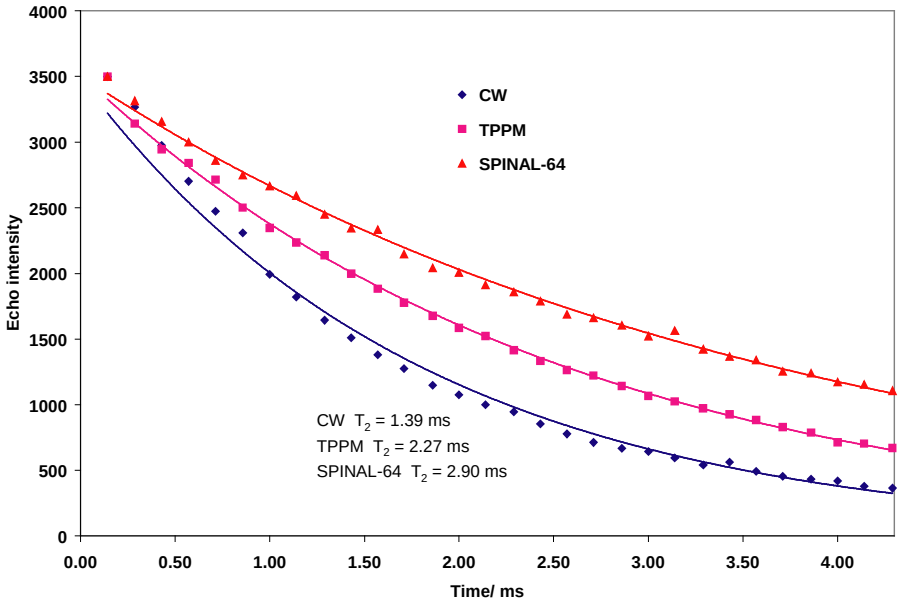

c)

	Natural	Nonrefocusable	Difference
CW	451	229	222
TPPM	276	140	136
SPINAL-64	273	109	164

Figure 60 a) ^{19}F spectrum of betamethasone-17-valerate using three different decoupling schemes, b) spin echoes of all three decoupling methods with decoupling optimised conditions. The results are summarised in c).

Visually the ^{19}F spectra is significantly different (see **Figure 60 a)**) between basic CW decoupling, and the more advanced phase modulation forms. What is interesting is there is little variation in between the sensitivity and resolution of TPPM and SPINAL decoupling, where there is a considerable increase in the T_2' value going from TPPM to SPINAL(see **Figure 60 c)**), which is consistent with previous work performed on $^{13}C^{19}$. This shows that experimentally that ^{19}F behaves similar to that of ^{13}C on the application of ^{1}H decoupling.

What is unclear is what is being reduced when switching to more complicated decoupling forms. As it is clearly shown in **Figure 60** the 'homogeneous' and 'inhomogeneous' contribution varies

for the decoupling sequences investigated. The T_2' values for TPPM and SPINAL decoupling should be similar due to the peak width at half height being comparable. The experiment shows that the measured T_2' values are measurably different for TPPM and SPINAL.

This highlights why it can be misleading to define the linewidth measured in a spin echo when decoupling is applied to be the homogeneous linewidth. Instead it is more common that the term refocused and non-refocused to be used. Previous workers[19] have had similar difficulties in trying to understand how the decoupling process works. They also had the problem of the refocused linewidth increasing when the natural linewidth decreased.

The experiments do highlight the need to optimise the decoupling in the experiment that you are interested in. Examples of where the need to optimise the decoupling sequence within that particular experiment are REDOR experiments, where longer dephasing times of the signal may mean more accurate measurements can be taken. Examples are discussed in reference 2.

The measured linewidth consists of three parts: true T_2 relaxation; decay due to incomplete decoupling from the ^{1}H network and inhomogeneous distribution of NMR frequencies e.g. ABMS. As the true T_2 relaxations are typically small and the inhomogeneous contributions will be refocused in the spin-echo experiments, it is the decay due to incomplete decoupling from the ^{1}H network that is varying in the spin-echo experiment. It is unclear what is being refocused during the spin-echo experiment. Work has been performed which highlights the complex theory on the application of two pulse modulation decoupling sequences[20], and highlights why it is difficult to predict decoupling efficiency.

What was interesting to note that the refocused contribution were around four times as great for ^{19}F linewidths in comparison to that for the ^{13}C linewidths seen for polycrystalline glycine[19]. The refocused linewidth should be proportional to the gyromagnetic ratio. This shows once again that decoupling for ^{19}F is no different than for ^{13}C or any other nucleus. The major difference compared to ^{13}C NMR is that the ^{19}F are not directly bonded to any ^{1}H, meaning weaker heteronuclear couplings.

The optimum decoupling conditions were similar to that of ^{13}C although the optimum phase shift for ^{19}F was around twice that of ^{13}C. The sensitivity of the intensity of the ^{19}F signal with respect to the decoupling was then compared against a series of carbon sites within betamethasone-17-valerate. These sites will have a varying number of directly bonded hydrogen's to see which site is most similar to the ^{19}F signal.

5.8 Comparison of decoupling for ^{13}C

In order to make a comparison it was necessary to perform a similar investigation into the ^{13}C linewidths with respect to the decoupling. In a typical organic system there are three ^{13}C types present, CH, CH_2 and CH_3. Of the three groups the CH_2 are the more difficult to decouple due to the two large dipolar couplings, and the limited motion about the bond. As all three sites can be acquired simultaneously in the betamethasone sample (using the assignment by previous workers[18]), it would be logical to see how the decoupling efficiency varies with respect to the phase shift and tip angle as performed on ^{19}F.

Comparing the two main decoupling forms for each carbon environment, it is hoped that a comparison can be made to ^{19}F, although the reduced sensitivity of ^{13}C with respect to ^{19}F makes it more difficult to perform a thorough investigation.

5.8.1 Experimental

In order for a fair comparison to be made in the two decoupling forms the parameters were optimised. A proton decoupling power of 50 kHz was applied during acquisition of ^{13}C, and a tip angle of 155°was found to be optimum for both the SPINAL and TPPM sequences.

As it was not necessary to reduce the homonuclear dipolar couplings as in the case for ^{19}F, all the work was performed at modest MAS rate (4.3 kHz) ensuring that CP could be performed on the HH condition. To ensure it is possible to compare the effect of the decoupling parameters for all peaks the intensity for each ^{13}C were plotted relative to the optimum peak intensity for that particular peak

5.8.2 Results

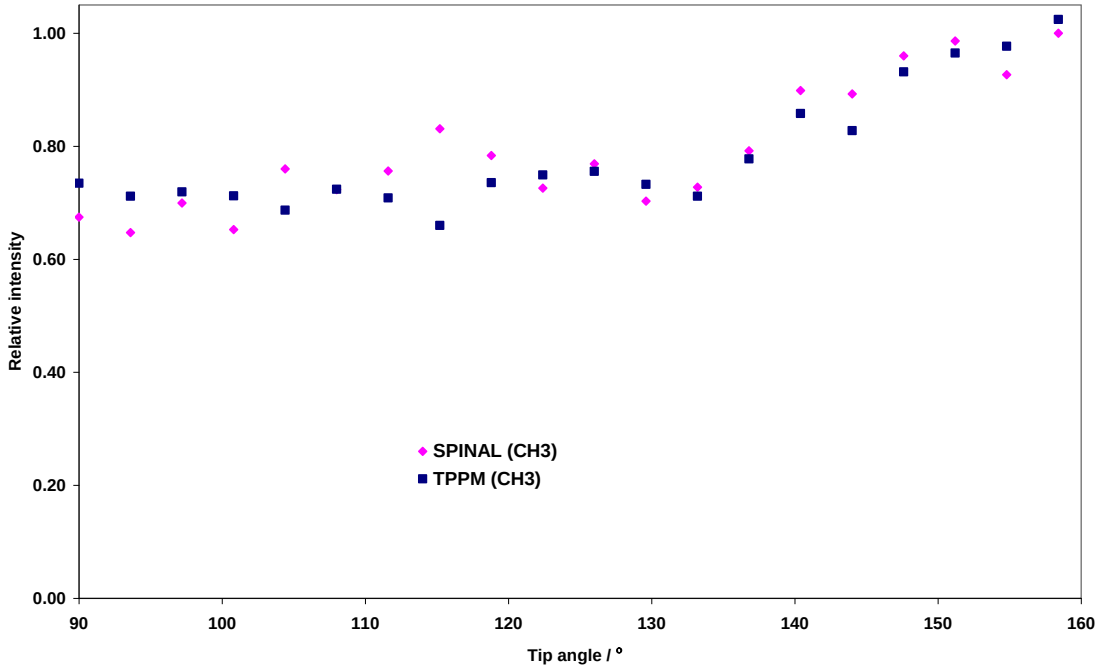

Figure 61 Comparison of SPINAL decoupling and TPPM decoupling on the effect of the overall intensity for a CH_3 group.

As can be seen from **Figure 61** the CH_3 groups are relatively insensitive to the tip angle for either TPPM or SPINAL decoupling sequence. The overall intensity of the peak varies only slightly when the tip angle is arrayed, also the two decoupling methods produce comparable results. The CH_3 groups tend to be relatively insensitive to the decoupling parameters as the couplings tend to be reduced by rapid motion about the carbon bond, resulting in only modest improvements in the decoupling efficiency.

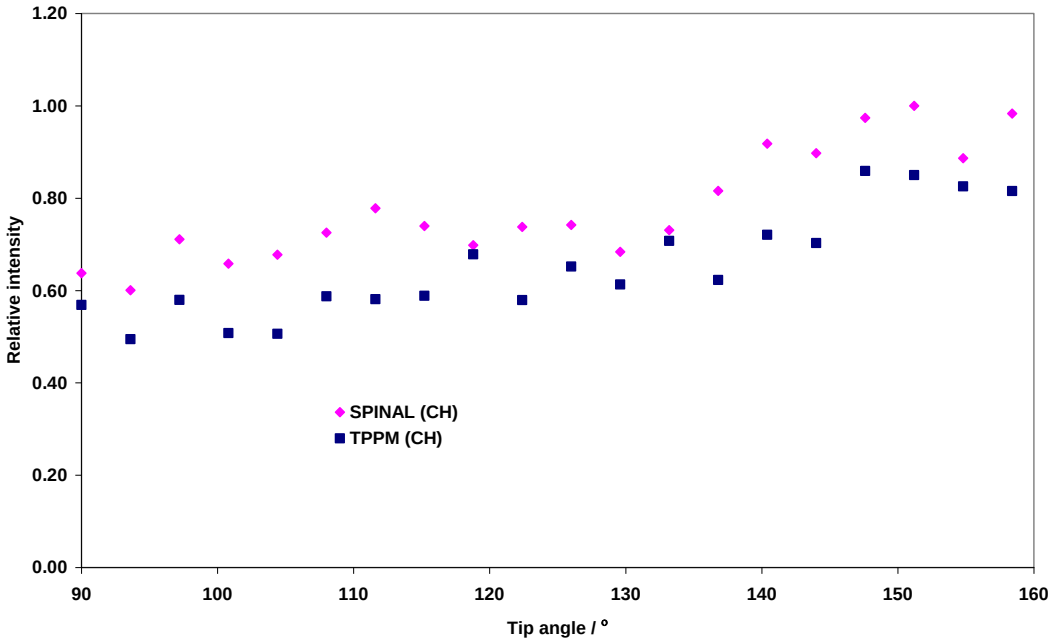

Figure 62 Comparison of the SPINAL and TPPM decoupling on the intensity of a ^{13}C with one ^{1}H directly bonded.

From **Figure 62** it is possible to see that the intensity of the peak, and hence the resolution of the peak is sensitive to the efficiency of the decoupling. There is an increase in sensitivity of around two when going from a tip angle of 90° to the optimum value of 155°. Also for all tip angles the SPINAL sequence constantly performs better than the TPPM sequence, which compares well to the decoupling data for ^{19}F.

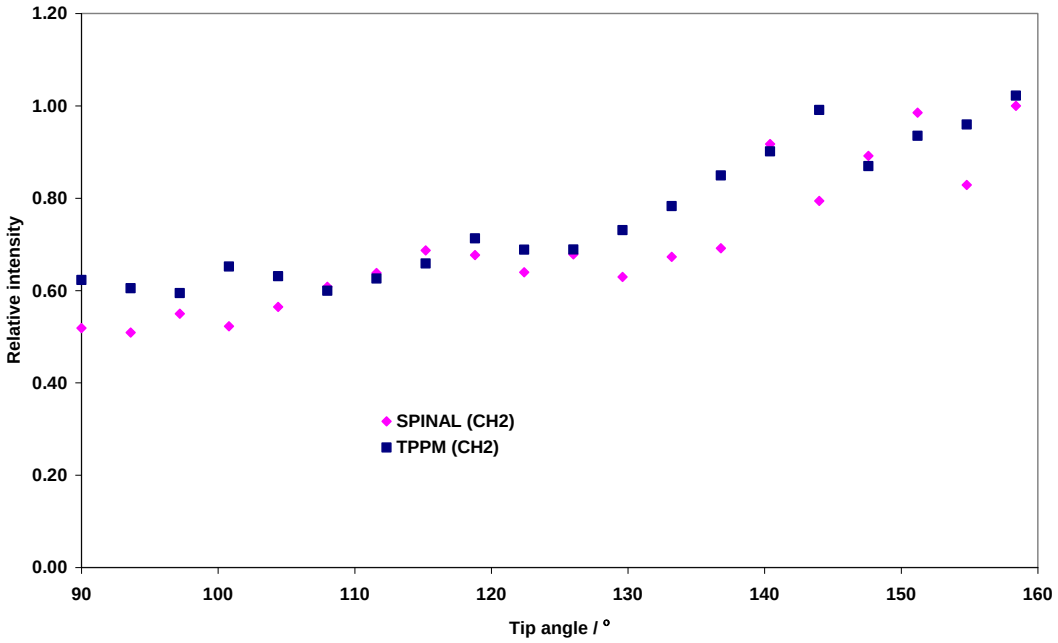

Figure 63 Comparison of SPINAL and TPPM decoupling sequences for the CH_2 group which is the most challenging carbon environment to decouple.

The final ^{13}C environment to investigate are the typically most difficult to decouple, the CH_2 groups. It is very hard to decouple these groups as the ^{13}C is strongly coupled to two ^{1}H's, and unlike the CH_3 groups there is no motion about the bond to reduce the couplings. From the investigation it is clear to see that the peaks are sensitive to the decoupling tip angle (see **Figure 63**). However there is not the noticeable difference in sensitivity for the two sequences as seen for CH groups.

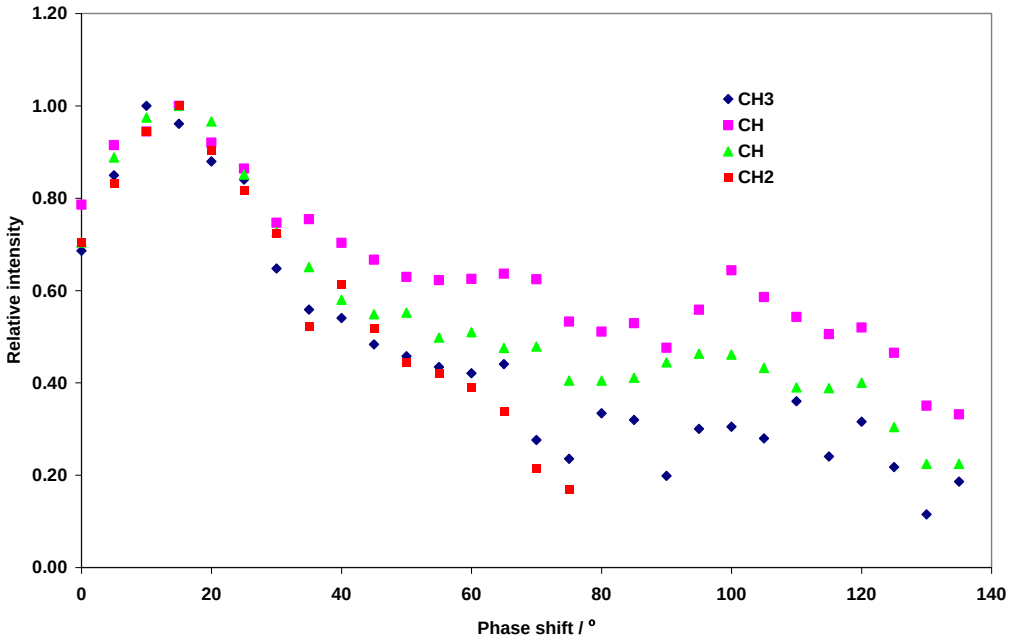

Figure 64 Phase shift investigation for all four ^{13}C environments using optimised TPPM decoupling, with a 50 kHz ^{1}H decoupling for a duration of 8.4μs before the phase is switched, corresponding to a tip angle of 151°

In **Figure 64** represents how the peak intensity is affected by varying the phase shift for the TPPM decoupling sequence. Switching from CW decoupling, where there is no phase shift to optimum TPPM decoupling results in a significant improvement in intensity of the peaks for all ^{13}C environments, where a maximum is seen for a phase shift of 15°. For phase modulations greater than 15° results in the peak intensities gradually decreasing for larger phase shifts.

For phase modulations greater than 140° it was not possible to measure the intensity of the peak as it had become too broad to be measured. The exception was for the CH_2 peak where the peak intensity was far more sensitive to the phase shift and the signal became un-measurable at lower phase shifts (> 80°)

The typical ^{13}C linewidth for this compound is in the region of 60-70 Hz, which is around four times narrower than for ^{19}F. This shows good agreement as any inhomogeneous contribution within this system will be scaled by the ratio of the gyromagnetic ratios, which in the case of $^{19}F/^{13}C$ is around an order of four. As efficient ^{1}H decoupling effectively removes all dipolar couplings for ^{13}C the dominant linewidth is due to inhomogeneous contribution.

In conclusion the decoupling investigation for ^{19}F is comparable to that of ^{13}C. The major problem is finding a ^{19}F compound that is sensitive to any variation to the decoupling. Once a suitable compound was discovered the increase in resolution and hence signal intensity from switching

between CW, TPPM and SPINAL-64 produces results comparable to that for ^{13}C. The only difference being is that it is more complicated setting up the experiments for ^{19}F, due to the similarity of the NMR frequencies of the two nuclei.

5.9 Conclusions

The work contained within this chapter gives a better understanding of ^{19}F linewidths, and as a result provides insight into how to reduce linewidths for specific cases.

Fluorine containing compounds cannot be classed as a singular group due to the wide range of possible systems. On the one extreme there are per-fluorinated compounds where homonuclear couplings are dominate, which are is similar to that of ^{1}H NMR. For systems that are dilute in ^{19}F the technique is now more comparable to that of ^{13}C NMR as homonuclear coupling proves to be less of an issue.

These next few sections explain how the optimum resolution can be achieved for the whole sample range of compounds studied.

5.9.1 Linewidth dominated by ^{19}F-^{19}F dipolar couplings

These cases are compounds that are rich in ^{19}F such as perfluorinated compounds e.g. octafluoronaphthalene and Teflon, and also inorganic fluorides. It has been shown that compounds containing CF_3 groups can be included in this category due to linewidths being dominated by ^{19}F-^{19}F dipolar couplings. For these compounds to gain the best possible resolution fast MAS is largely sufficient, as the resolution is not significantly affected by ^{1}H decoupling.

5.9.2 Samples containing ^{1}H and dilute in ^{19}F

These compounds will have more pharmaceutical applications as ^{19}F containing active pharmaceutical ingredients tend to be dilute in ^{19}F, while containing large numbers of ^{1}H. The AstraZeneca compound investigated was relatively insensitive to any variation in the decoupling form applied, due to the relatively weak ^{1}H-^{19}F interactions.

When switching to betamethasone-17-valerate, the importance of optimising the decoupling sequence became more obvious. It also showed the efficiency of the SPINAL sequence in comparison to both CW and TPPM. The optimum conditions are also very similar to those used when acquiring on ^{13}C. To save time both experimentally and taken optimising the decoupling it is

recommended to use SPINAL-64 decoupling in all cases when decoupling is required, as it is never worse than TPPM decoupling.

The overall linewidth of ^{19}F with a low inhomogeneous contribution is comparable to that of ^{13}C. The lines are generally broader but that is to be expected due to the inhomogeneous contribution scaling by the gyromagnetic ratio of a system.

5.9.3 Compounds with large ABMS contribution.

Sometimes simple fast MAS will not produce sufficiently good resolution, such as the case for OFN. Due to there being no ^{1}H's present there would be no gain in using SPINAL decoupling at all. In these cases there may be a benefit in 'diluting' the compound in a sample with a low ABMS value such as NaCl. This reduces the ABMS within the system and hence the 'natural' linewidth. This may be of benefit to pharmaceutical compounds when detecting on ^{19}F. Due to its high sensitivity and abundance ^{19}F can be detected in very small concentrations, even in formulated drug blends. Working with formulated drug blends may in fact improve resolution (but not sensitivity) due to the reduction of the inhomogeneous contribution.

5.9.4 Achieving the best possible resolution in ^{19}F NMR

The overall conclusion from this chapter is that to achieve the best resolution for a specific sample an assessment needs to be performed first of the sample. If the sample is per-fluorinated or the ^{19}F is present as a CF_3 group, then optimum resolution can be achieved by fast MAS alone. If the linewidths for the sample are still relatively broad at fast MAS this hints that there is a large inhomogeneous contribution present, which is difficult to reduce. One possibility is the use of the dilution experiment although this does tend to be sample specific.

For more pharmaceutical applicable compounds, that is systems dilute in ^{19}F, then the need to ^{1}H decouple is essential at the highest magnetic field available. In order to gain the largest improvement in resolution and sensitivity it is always advised to use SPINAL decoupling over TPPM and CW. A flow chart has been produced to enable to most efficient technique can be found for a specific sample (see **Figure 65**).

If there is going to be a lot of ^{19}F work with ^{1}H decoupling performed it may also be advantageous to invest in a 2.5 mm HF probe. By using the 4 mm probe for our HF work it has not always been beneficial to apply ^{1}H decoupling due to the far lower spinning rates compared to the 2.5 mm probe. Only a small volume of sample is needed due to the high sensitivity of the ^{19}F nuclei, and if decoupling was applied at the very fast MAS rates of the 2.5 mm probe then significant increase in

resolution may be achieved. Also higher RF powers can be applied for the smaller diameter probe, resulting in more efficient decoupling.

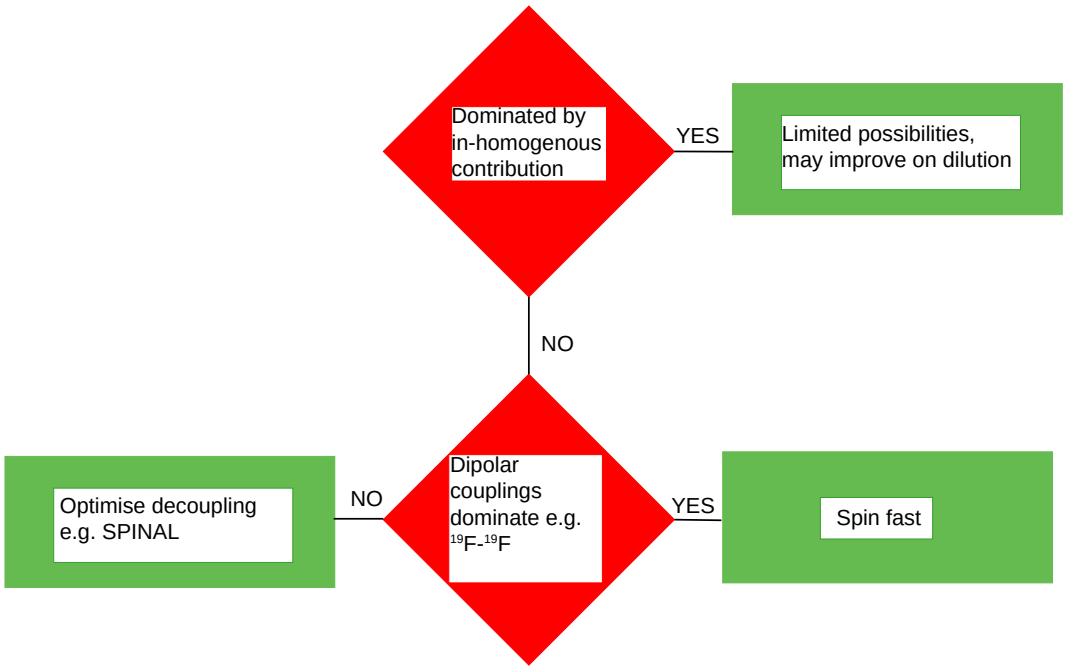

Figure 65 Flow chart showing how to decide what experiment will provide the optimum resolution for a specific sample.

5.10 References

(1) Bloch, F.; Siegert, A. *Physical Review* **1940**, *57*, 522 LP.

(2) Ramsey, N. F. *Physical Review* **1955**, *100*, 1191 LP.

(3) Vanderhart, D. L.; Earl, W. L.; Garroway, A. N. *J. Magn. Reson.* **1981**, *44*, 361-401.

(4) Garroway, A. N.; VanderHart, D. L.; Earl, W. L. *Phil. Trans. R. Lond. A* **1981**, *299*, 609-628.

(5) Pines, A.; Gibby, M. G.; Waugh, J. S. *Journal of Chemical Physics* **1973**, *59*, 569-590.

(6) Miller, J. M. *Prog. Nucl. Magn. Reson. Spectrosc.* **1996**, *28*, 255-281.

(7) Brunner, E.; Fenzke, D.; Freude, D.; Pfeifer, H. *Chemical Physics Letters* **1990**, *169*, 591-594.

(8) Paëpe, G. D.; Giraud, N.; Lesage, A.; Hodgkinson, P.; Emsley, L. *J. Am. Chem. Soc.* **2003**, *125*, 13938-9.

(9) Hodgkinson, P. *Prog. Nucl. Magn. Reson. Spectrosc.* **2005**, *46*, 197.

(10) Bennett, A. E.; Rienstra, C. M.; Auger, M.; Lakshmi, K. V.; Griffin, R. G. *J. Chem. Phys.* **1995**, *103*, 6951-6958.

(11) Khitrin, A. K.; Fujiwara, T.; Akutsu, H. *J Magn Reson* **2003**, *162*, 46.

(12) McGeorge, G.; Alderman, D. W.; Grant, D. M. *J. Magn. Reson.* **1999**, *137*, 138.

(13) Fung, B. M.; Khitrin, A. K.; Konstantin, E. *J. Magn. Reson.* **2000**, *142*, 97.

(14) Brauniger, T.; Wormald, P.; Hodgkinson, P. *Monatsh. Chem.* **2002**, *133*, 1549.

(15) Detken, A.; Hardy, E. H.; Ernst, M.; Meier, B. H. *Chem Phys Lett* **2002**, *356*, 298.

(16) Hodgkinson, P.; Sakellariou, D.; Emsley, L. *Chemical Physics Letters* **2000**, *326*, 515-522.

(17) Zorin, V.; Hodgkinson, P.; Brown, S. P. *J. Chem. Phys.* **2006**.

(18) Carss, S. A.; Scheler, U.; Harris, R. K. *Magn. Reson. Chem.* **1996**, *34*, 63-70.

(19) Paëpe, G. D.; Lesage, A.; Emsley, L. *J. Chem. Phys.* **2003**, *119*, 4833-41.

(20) Scholz, I.; Hodgkinson, P.; Meier, B. H.; ERNST, M. *Journal of Chemical Physics* **2009**, *130*, 114510.

6 Relating NMR chemical shifts and structure in ^{19}F NMR

6.1 Introduction

Octafluoronapthalene ($C_{10}F_8$) [or perfluoronapthalene] has been regularly used as a model system in the development of ^{19}F solid-state NMR. Initial work on octafluoronaphthalene (OFN) was performed by Mehring *et al*[1], they were able to resolve the two chemically distinct sites (i.e. α and β) by using multi –pulse ^{19}F homonuclear decoupling on a static sample. This work was extended by Harris *et al*[2], they were able to combine multi-pulse homonuclear decoupling with slow magic angle spinning enabling them to resolve the two signals into pairs of signals, corresponding to the four crystallographic distinct fluorine sites within the crystal structure (see **Figure 66 (b)**)

The structural chemistry of OFN at room temperature is intriguing as the structure is not well defined by current techniques. It is thought to adopt a similar structure as normal naphthalene (see **Figure 66 (b)**) above 281.5 K[3], but the extent of the diffuse X-ray scattering and the poor quality fit, indicates that there is a large amount of disorder within the system either static or dynamic. Work is currently underway to try to determine an accurate crystal structure of OFN. A better quality crystal structure has been calculated, which showed that there was disorder present in the orientation of the molecules. It is hoped that this new structure can be used for molecular dynamic calculations, which would give a better insight as to what is happening at the molecular level at room temperature.

NMR is a very sensitive technique to changes in the local environment[4]. One example of where solid-state NMR has been used to distinguish between polymorph forms is for finasteride[5], where the compound formed a series of solvates. Solid-state NMR was able to distinguish between all the solvates produced, but when submitted for powder XRD there were almost indistinguishable. Powder XRD had difficult in differentiating between the forms due to the associated motion, as finasteride forms channel solvates, where there is a high degree of mobility. This mobility did not prove to be a problem for solid-state NMR

Due to the degrees of symmetry present in OFN, it is a bit ambiguous to represent the ^{19}F sites as a typical 2D structure as there are four magnetically different ^{19}F sites and only two chemically different sites (see **Figure 66 (a)**). It is more informative that the molecule is stated within the crystal structures, where chemical equivalent sites now show to be magnetically different (see **Figure 66 b)** and **c)**).

This overall disorder appears to be dynamic on the basis of previous NMR studies[1], which showed a drop in the width of the static ^{19}F spectrum at 254 K with the suggestion that the molecules are re-orienting about the C_2 axis perpendicular to the molecular plane. This is consistent with the proposed X-ray structure in which fluorine sites related by the molecular centre of inversion are identical. Initial findings via molecular dynamics have shown that there is motion present, however it does appear to be more of a 'wobble' than a full flip. Of course molecular dynamics is only able to predict motion on a relatively short time scale, in comparison to that of NMR.

Fast magic angle spinning is routinely used for abundant nuclei such as ^{1}H and ^{19}F to improve the resolution by reducing the extensive dipolar coupling network[6]. As shown in **Figure 66 (c),** the fast MAS spectrum clearly resolves the four sites into two pairs corresponding to α sites (attached to carbons 1, 4, 5 and 8) and β sites (attached to carbons 2, 3, 6 and 7). These pairs can be assigned, as indicated, on the basis of solution-state shift values[2]. Unfortunately it is not possible to assign individual resonances to fluorine sites in the crystal structure on the basis of this NMR data in isolation.

Interestingly the chemical shift range for the liquid state (9.1 ppm) is greater than the chemical shift range for the solid state (6.3 ppm). Typically the chemical shift range is greater for solids than liquids as there is isotropic tumbling present in liquids, which in effects means that each molecule has no interaction with neighbouring molecules. In contrast, for solids the crystal packing effects such as anisotropy is expected to increase the range of environments, and hence the chemical shift range. Also, due to the isotropic tumbling in liquids means that there are only two magnetically different ^{19}F sites in comparison to the four in the solid case.

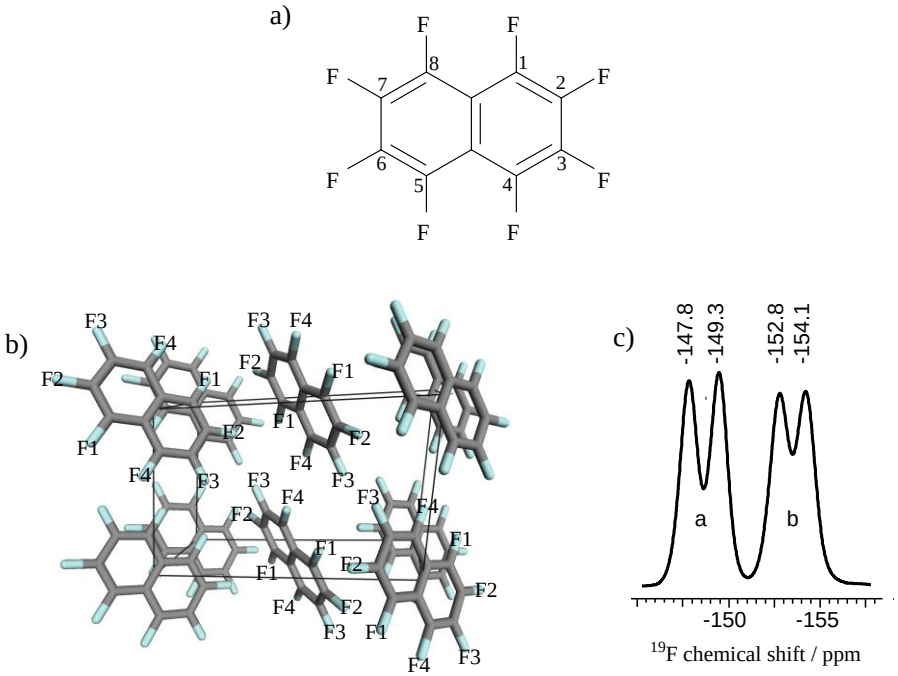

Figure 66. (a) Molecular structure of octafluoronaphthalene, (b) ambient-temperature crystal structure (reference code OFNAPH01 from the Cambridge Structural Database). (c) Ambient temperature ^{19}F MAS spectrum (MAS spin rate of 24 kHz and ^{19}F Larmor frequency of 470 MHz), showing four clearly resolved sites.

In this chapter, we extend the ^{19}F work performed previously to complete the assignment of the ^{19}F peaks for OFN using density functional theory (DFT) calculations. Combined with 2D NMR experiments these calculations are used to confidently assign all four peaks for each specific site within the crystal.

6.2 ^{19}F resolution under fast magic-angle spinning

As mentioned earlier (see section 3.3), rotation of samples about the magic angle (54.7°) with respect to the magnetic field axis effectively averages the dipolar couplings that are responsible for the broadening of the solid-state NMR spectra of abundant nuclei, such as ^{1}H or in this case ^{19}F. Particularly at high static magnetic fields (corresponding to ^{1}H NMR frequencies of about 400 MHz or higher) useful ^{1}H resolution can be obtained at spinning rates in excess of about 20 kHz[7].

As mentioned in section 5.2 the observed NMR linewidth can be split into two contributing factors, homogeneous and inhomogeneous linewidth. The homogeneous linewidth is dependent upon the dipolar couplings present at a specific MAS rate, and is reduced by fast MAS. The inhomogeneous linewidth is independent of the MAS rate [8] and is sample dependent.

OFN was selected for further investigation due the sample's relatively large inhomogeneous contribution, which was expected to be due to ABMS contribution. The ABMS value is expected to be large for this sample due to the aromaticity of the system. The ultimate aim is understanding the effect of ABMS broadenings, and try to reduce the effect. Any improvement in resolution will be easy to detect, as the peaks are not fully resolved, as in **Figure 66 (a)**.

MAS is only partially successful if the bulk susceptibility is anisotropic i.e. directionally dependent and so time dependent under MAS[6,9,10]. The effect, as mentioned earlier, can be quantified by the dimensionless parameter $\Delta\chi$ - anisotropy of the bulk magnetic susceptibility (ABMS) of the material. As the effect is only partially averaged under MAS, a single crystallite experiences an average bulk susceptibility under MAS, which will depend upon its orientation to the rotor axis, which will lead to broadening of the solid-state peaks.

The packing of the naphthalene structure in both $C_{10}F_8$ and $C_{10}H_8$ it is expected that the $\Delta\chi$ value to be typically large. These $\Delta\chi$ values can be extracted from the DFT where the magnetic susceptibility per volume is calculated. These values can then be compared for a number of compounds to get a better understanding of the influence this has for specific compounds. For OFN the $\Delta\chi$ value was $\Delta\chi >> 1.6\times10^{-7}$ in comparison to only 8.1×10^{-9} for the β form of testosterone.

Testosterone was used as a comparison as steroids tend to have low values for magnetic susceptibility due to there being no aromatic rings present. In general the linewidths in the steroid compounds tend to be far narrower than for compounds like OFN. These $\Delta\chi$ values are un-rationalised units and are of little use in the current state, when converted to a more meaningful form ($|4\pi\Delta\chi|$) the magnetic susceptibility for OFN is 2.0 ppm, compared to 0.1 ppm for testosterone. This shows why it is so difficult to gain high resolution in ^{19}F NMR in solids, as any inhomogeneous contribution will be scaled by around four times with respect to ^{13}C.

The ABMS broadening of the lines is typically inhomogeneous, depending upon crystals orientation within the magnetic field. The NMR frequency is shifted by the anisotropy of the bulk magnetic susceptibility for each crystal orientation. This results in broadening of the peaks in solids as the peaks are a sum of the overall NMR signal in all of the crystals orientations. Work has been performed on single crystals in NMR[11] with a five-fold reduction in linewidths. Attempts have been to acquire a spectra for OFN with a single crystal with no success. The main problem was the high MAS rates required for acquisition which resulted in the single crystal being damaged due to the high forces.

The magnetic susceptibility will be influenced by factors such as sample packing and crystal morphology. The sample packing will have an effect on the susceptibility, as if voids are present in the rotor, this will alter the magnetic environment of the sample, resulting in broadening effects. To reduce the effect, the sample is ground prior to packing to reduce the particle size and also helps to ensure more efficient packing.

The magnetic susceptibility will be directly proportional to final broadening of the linewidth, work has shown that these calculations do agree reasonably well with experimental work. Typically ^{19}F inhomogeneous contributions are in the region of 500 Hz for aromatic compounds, while the ^{19}F inhomogeneous contribution is around a quarter of that for betamethasone-17-valerate in chapter 4.

It was not possible to directly compare the ^{13}C linewidth to that of the ^{19}F linewidth for OFN due to the need to apply ^{19}F decoupling. As mentioned previously (see section 5.7.3) the application of decoupling results in the terms homogeneous and inhomogeneous[12] can no longer be used. Previous workers as a result have described the homogeneous linewidth as the refocused linewidth, while the inhomogeneous linewidth is stated as being the non-refocused linewidth.

A similar relationship has been seen with ABMS and linewidths when detecting via ^{13}C by VanderHart *et al*[6], where they recorded the linewidths of a material with a large ABMS (hexametylbenzene HMB) on addition to a sample with a low ABMS (adamantane). They recorded that the adamantane linewidths approximately doubled in a 50/50 mixture of HMB/adamantane, compared to pure adamantane. In contrast the HMB linewidths were not affected as greatly but there was a small decrease. More work on the ABMS experiments can be found in section 5.4 and 5.5.3, which discusses improving ^{19}F resolution.

6.3 2D lineshapes in correlation spectra

Recent work has shown that the linewidths for 2D correlation experiments are limited to the homogeneous linewidth alone and not the total linewidth. It is therefore possible to extract more information from inhomogeneously broadened lines than might be expected on the basis of 1D spectra[13]. As the frequency shifts due to ABMS at different sites in the same crystallite are perfectly correlated with each other, the peak shapes in 2D spectra should reveal the correlation between the frequencies in the two dimensions.

Having shown that for OFN there is a significant inhomogeneous contribution due to ABMS, a homonuclear correlation experiment was performed. This would provide valuable information that could be used to aid the assignment of the peaks to the specific site within the crystal. The

correlation spectrum should also show characteristic peak shapes expected from strongly correlated inhomogeneous broadenings.

2D ^{19}F homonuclear correlation spectrum were obtained of OFN using the EXSY/NOESY pulse sequence, with a relatively short mixing time used (2.3 ms). A short mixing time was used to ensure that only the strongest couplings are seen within the solid OFN form. The experiment is said to be both an EXSY and NOESY experiment, with is being able to detect both exchange of ^{19}F and through space correlation (nuclear Overhauser effect). Magnetisation transfer due to exchange can not really be distinguished from transfer due to NOE.

The presence of off diagonal peaks in **Figure 67 (a)** shows that magnetisation transfer has occurred between the two fluorine sites. The correlations between the α and β sites can not be due to physical motion, as this will not mix chemically distinct sites. This transfer must be due to spin diffusion via the dipolar couplings between close spins present within the system.

The couplings of adjacent α and β sites are significantly stronger than for remote α and β sites, even taking into consideration the intermolecular couplings. These are calculated by using the XRD crystal structure to compute the root sum square coupling between a given spin and all the surrounding spins of a given type[14]. As for the REDOR work, the weaker couplings will have little effect on the total couplings, as the effect is proportional to one upon the distance cubed. As a result the observed coupling will be dominated by the closest spin pair.

As a result the pattern of off-diagonal peaks between α and β resonances allows a clear connection to be made between peaks at –147.8 and –149.3 ppm, and also the peaks at –152.8 and –154.1 ppm. Hence, the magnetisation exchange experiment establishes a relative assignment of the four ^{19}F resonances. It does not however allow full assignment of the peaks to sites within the crystal structure, as it is not possible to distinguish between the two α sites and the two β sites. Note that similar proximity relationships could, in principle, be obtained using other 2D NMR techniques. For instance, radio-frequency driven recoupling (RFDR)[15] has previously been used study F–F proximity in fluoropolymers[16,17]. EXSY/NOESY[18] experiment was used in this case as the simple three pulse sequence avoids any RF pulses applied during the mixing time which would prevent any unwanted interaction between the molecular motion and the RF irradiation.

The correlation between frequencies in f_1 and f_2, expected from the ABMS shifts, is observable in **Figure 67 (a)** for the four diagonal peaks as a distinct elongation of the peak shape along the diagonal of the spectrum. This shape is obscured and it is difficult to be certain that this is fact a true result. Care was taken when plotting the 2D spectrum that the range of both dimensions were identical, to ensure that a non-square aspect ratio did not create a false appearance of correlation.

Even so, the correlation present does not appear to be very clear, particularly for the off diagonal peaks.

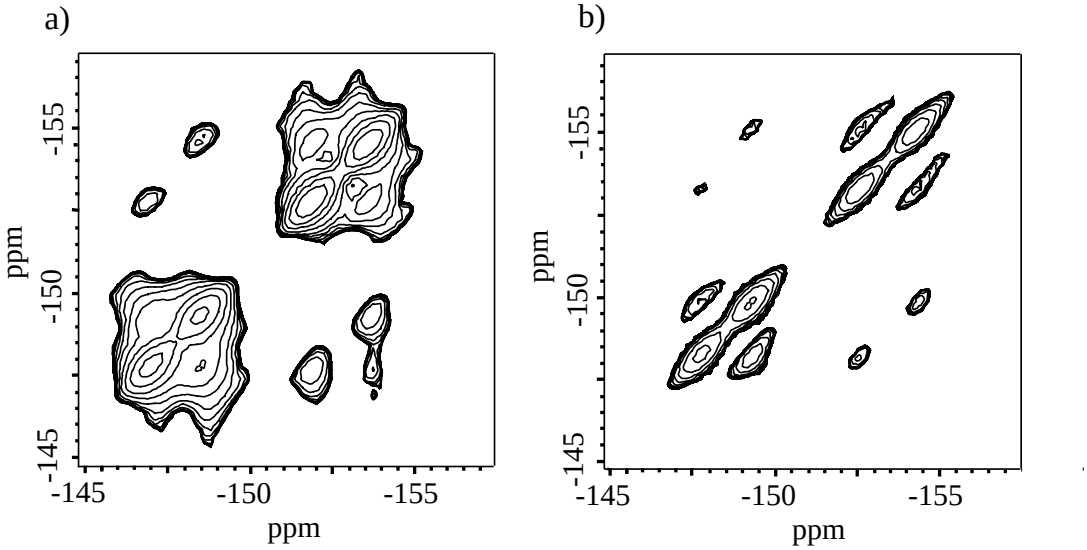

Figure 67 ^{19}F NOESY/EXSY spectra of octafluoronaphthalene using a short mixing time of 2.3 ms: (a) without lineshape transformation, (b) after Lorentzian-Gaussian transformation (subtracting 300 Hz of Lorentzian linewidth and adding 300 Hz of Gaussian line broadening). The experiments used a 4.5μs 90° pulse for ^{19}F with 48 time steps in the indirect dimension and a spectral width of 14.66 kHz in the indirect dimension. The sample was spun at 22 kHz and the recycle delay was 16 s.

The poor quality of the correlation as seen in **Figure 67 (a)** can be traced to two reasons: Lorentzian-like lineshapes, and t_1 ridges which obscure correlation for the weak off diagonal peaks. Lorentzian lines are similar in shape to Gaussian lines in simple 1D spectra, but there is a significant difference in the two when comparing them in the 2D spectrum. Lorentzian 2D lineshapes have a distinct 'star shape' cross-section, particularly towards the base of the peaks (see **Figure 68**). This lineshape makes detecting any correlation present very difficult as is seen in **Figure 67 (a)**, where the correlation is somewhat obscured by the lineshape. In contrast the typical Gaussian lineshape always has a circular cross section area (see **Figure 69**), meaning any correlation will resulting in a more clearly elliptical lineshape.

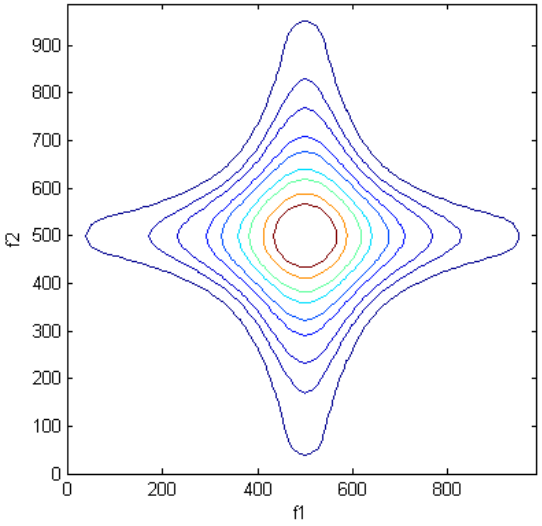

Figure 68 Calculated 2D Lorentzian lineshape with a width at half-height of 60 Hz. The 'star-shaped'2D peaks is a commonly seen for Lorentzian shaped lines, which can obscure any correlation present as seen in **Figure 70 (a)**

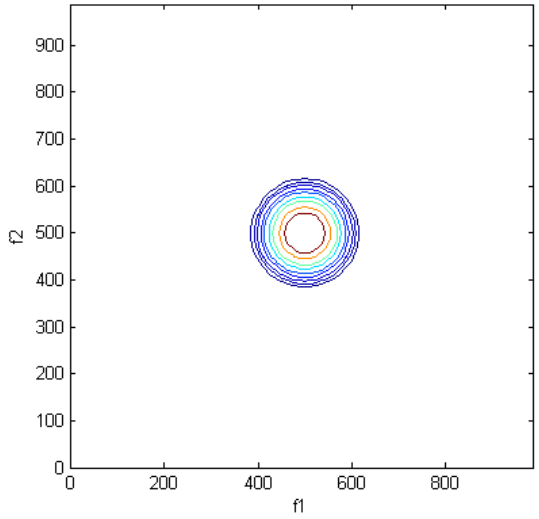

Figure 69 Calculated 2D Gaussian lineshape with a width at half-height of 60 Hz. The cross section of a Gaussian 2D line is circular, meaning any correlation present will form elliptical shaped peaks.

Figure 70 (a) and **(b)** illustrate how the lineshape affects the 2D spectrum, using a simulated magnetisation transfer. In the simulated magnetisation transfer in **Figure 70** the overall linewidth is a convolution of the homogeneous linewidth along with the inhomogeneous contribution. The inhomogeneous contribution is 100% correlated in the two dimensions (as is the case for ABMS) i.e. we expect to see a correlation along $f_1 = f_2$.

In **Figure 70 (a)** the underlying homogeneous linewidth is Lorentzian, and as **Figure 68** shows has a distinct star shape cross sectional area[19]. Looking closely at **Figure 70 (a)**, it is possible to see that there is a correlation present, but the star shaped peaks of the Lorentzian lineshape obscure this correlation.

The simulations of the magnetisation transfer were repeated and the homogeneous contribution was now given a Gaussian lineshape, and the difference is very clear. The correlation can be clearly seen as all four peaks are parallel along $f_1 = f_2$ (see **Figure 70 (b)**). Also the Gaussian lineshape decays more quickly to the baseline, meaning another increase in the resolution compared to a Lorentzian lineshape.

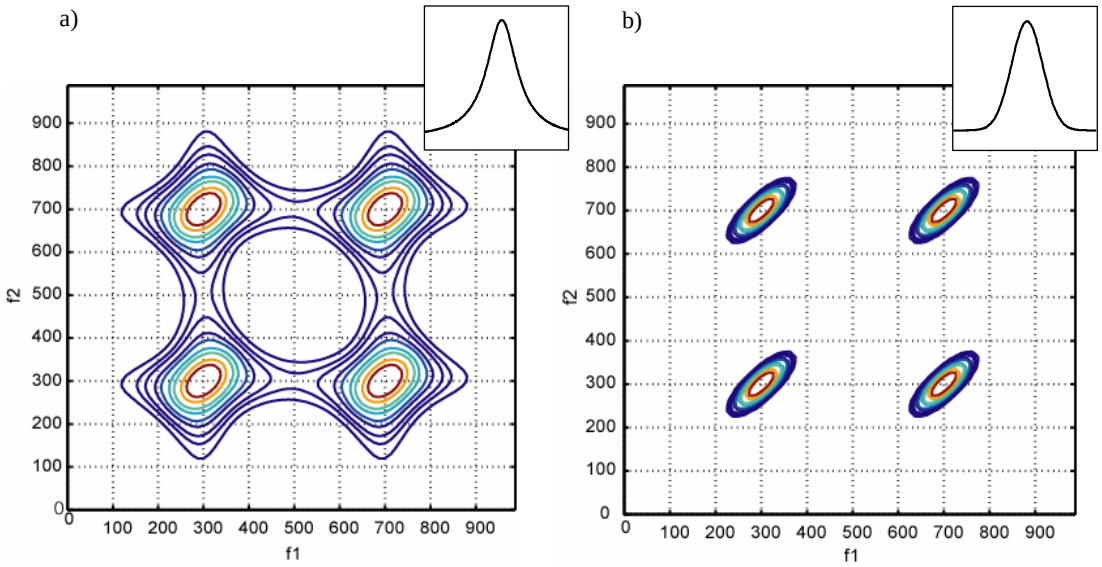

Figure 70 Calculated 2D magnetisation exchange lineshapes in which inhomogeneous broadenings between the two sites are perfectly correlated: (a) using a Gaussian lineshape with a width of 100 Hz to represent the inhomogeneous distribution of frequencies and a 30 Hz homogeneous (Lorentzian) fundamental lineshape, (b) as before, but with a 30 Hz Gaussian homogeneous lineshape. The peak shape now clearly reveals the underlying correlation between the inhomogeneous broadenings which is obscured by "star" profile of the homogeneous lineshape in (a). Insets show the respective 1D Gaussian and Lorentzian lineshapes (see Appendix 10).

It is possible in effect to transform the lineshape from one form to another by appropriate processing. By performing a Lorentzian to Gaussian transformation, (where the Lorentzian function was reduced and replaced with a Gaussian function prior to the Fourier transform,) it is possible to remove the unwanted star shaped peaks associated with the Lorentzian lineshape and replace it with the circular Gaussian lineshape.

Figure 70 (b) is the resulting spectrum after the transformation has been applied. To perform a Lorentzian to Gaussian transformation a suitable value, in this case 300 Hz of Lorentzian lineshape was 'subtracted' from the FID. Effectively this means multiplying the time domain (FID data) by a suitable rising exponential function. The transformation is completed by adding a suitable line broadening Gaussian function, in this case 300 Hz was added.

The transformation in this case replaces and is hence information preserving, meaning that there is no risk that unwanted artefacts are introduced. For optimum efficiency, the transformation value used should relate to the inhomogeneous linewidth. If too small of a value is used a correlation may not be seen as it is still obscured by the Lorentzian lineshape, too large and artefacts can be introduced, such as 'sinc wiggles' which could be misleading. The transformation value of 300 Hz relates roughly to the inhomogeneous contribution for OFN, as measured via spin echo experiments.

Comparing the two spectrum in **Figure 70 (a)** and **(b)** clearly show that **Figure 70 (a)** is a poor representation of the correlation, between line frequencies since this "correlation map" is obscured by the convolution with the natural lineshape. It is only when the appropriate processing is applied does this correlation become apparent.

Varying the added Gaussian linewidth will determine whether the overall effect of the lineshape transformation is to smooth the data set (and improve signal-to-noise ratio) or "enhance" the resolution[20]. However, the information-preserving nature of the lineshape transformation means that accurate estimations of homogeneous lineshape are not important, and suitable values for the transformation can be determined by eye.

The spectrum after the Lorentzian to Gaussian transformation (see **Figure 67 (b)**) shows a strong correlation for the inhomogeneous broadenings for all fluorine sites. This transformation also significantly narrows the anti-diagonal peak cross section. This improvement is essentially cosmetic, however; poorly-resolved features will be easier to distinguish[13] after "resolution enhancement", but it will not be possible to resolve features that are not distinct in the one-dimensional spectrum.

Comparing **Figure 67** (a) and (b), it is noticeable that the orientation of the cross-peaks between the α and β sites seems to have shifted, with the peaks in (b) now being aligned along the diagonal, as expected. Close inspection of a stack plot of the original data (see **Figure 71**), shows that initially the diagonal peaks are not aligned along the diagonal due to t_1 ridges[21]. These are reduced, but not entirely eliminated, by adjusting the scaling of the first point scaling prior to Fourier transformation of the direct acquired dimension. Sharpening the peaks by lineshape

transformation increases the size of the off-diagonal peaks relative to the ridges, reducing the latter's distorting effects. This leads to the "correct" correlation pattern observed in Fig. 3 (b).

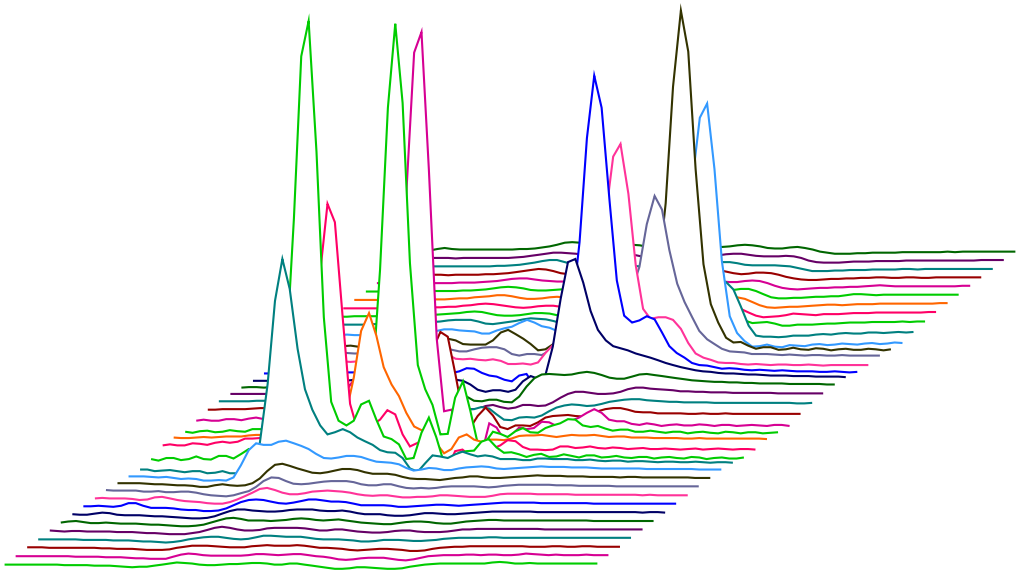

Figure 71 Stacked plot of OFN showing how the effect of t_1 ridges can obscure data for when small amount of signal present

The same correlation experiment was repeated, but this time a much longer mixing time was used (23 ms). The longer mixing time will allow for the weaker couplings to transfer magnetisation which will be shown in the EXSY/NOESY experiment (see **Figure 72**). Also the longer mixing time would allow for any physical exchange occurring for the ^{19}F sites, although it would not be possible to distinguish from magnetisation transfer via dipolar couplings.

The correlation spectrum shows that in this case all the peaks are correlated with one another. The cross peaks that were present in **Figure 67** are now much stronger, due to increased mixing time as more efficient magnetisation transfer has occurred. It is also possible to see small peaks present due to F_1-F_3 and also F_2-F_4 magnetisation transfer. It is also clear to see that the cross peaks are now clearly aligned along the diagonal, as t_1 does not have as great of an effect due to increased peak intensity.

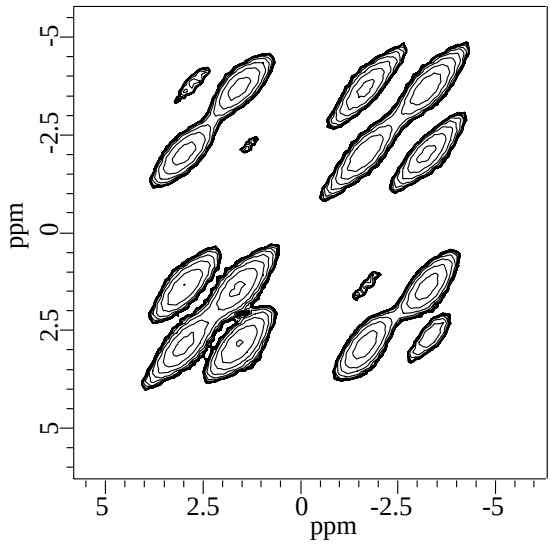

Figure 72 ^{19}F NOESY/EXSY spectra of octafluoronaphthalene using a long mixing time of 23 ms with Lorentzian-Gaussian transformation (subtracting 300 Hz of Lorentzian linewidth and adding 300 Hz of Gaussian line broadening. Parameters are as above.

6.4 Calculation of chemical shifts from crystal structures

The NMR data presented earlier was unable to provide a definitive assignment of the individual resonances to specific fluorine sites within the crystal structure. In order to be able to assign the peaks, density functional theory calculations were performed using the first principles electronic structure package, CASTEP[22]. By comparing the NMR results to the computational chemical shifts it is hoped that full assignment of the NMR peaks can be achieved as well as an more representative crystal structure for OFN at ambient room temperature.

To perform an *ab initio* calculation first the crystal structure needs to be optimised to ensure that the calculations are performed on a representative crystal structure. This is important for nuclei of low atomic mass, typically ^{1}H, as it is difficult to accurately determine their position via X-ray diffraction. Low atomic mass nuclei such as ^{1}H are typically difficult to locate accurately via X-ray diffraction as the technique relies on electron density. From the optimised crystal structure the chemical shielding tensors can be calculated. The crystal structure was obtained from the Cambridge Structural Database (with reference code OFNAPH01). As mentioned earlier there is a large amount of disorder present within the OFN crystal structure, making it difficult to construct an accurate representative crystal structure.

The geometry optimisation was performed for OFN, as the crystal structure within the Cambridge Structural Database had a poor agreement between experimental and theoretical results. The geometry optimisation relies on *ab initio* forces to correctly predict a more accurate crystal

structure for the system being investigated, in this case OFN. The optimised structures were determined by relaxed atomic positions within this symmetry group using *ab initio* forces, considering the calculations to have converged when the components of all the forces are below 0.01 eV $Å^{-1}$. This is a standard procedure prior to running any CASTEP chemical shift calculations.[23]

To explain the idea of the minimisation better the OFN provides a very good example. As mentioned earlier a phase change occurs for OFN at 281.5 K. The geometry optimisation would not be able to predict this phase change as the calculations are performed in idealised conditions, that is no vibrational motion, at 0 K. Therefore if an incorrect crystal structure is used, for example the crystal structure of OFN below the phase transition, then the optimised structure will be for the other form of OFN. It is therefore imperative that as accurate as possible a crystal structure is used for the geometry optimisation step.

Calculations were performed using the Perdew-Burke-Ernzerhof (PBE)[24] and Keal-Tozer-3 (KT3)[25] generalised gradient approximation to the exchange-correlation interactions. The former (PBE) is a non-empirical approximation, which is widely used in solid-state physics and describes many physical properties of solid-state systems accurately. The latter (KT3) is a semi-empirical approximation, which was specifically designed to provide improved quality absolute shielding constants. Initial calculations were performed at the original X-ray structure from the Cambridge Structural Database (reference code OFNAPH01). Additional calculations were therefore performed at optimised structures, determined self-consistently using the respective functionals.

For the chemical shift calculations, we are not particularly interested in absolute chemical shifts values, rather the difference in the chemical shifts for each site. As a result, no effort was made in trying to reference the calculated chemical shifts.

The *ab initio* calculations will calculate the chemical shielding tensor for a particular nucleus. The chemical shifts can be calculated from the shielding tensors via **Equation 10**, where δ is chemical shift and σ is the shielding tensor. For the OFN case, the chemical tensors signs were reversed to give the appropriate chemical shift value. The mean of the chemical shift values were calculated and adjusted to that of the experimental data, to enable a fair comparison[23].

$$\delta \approx (1 - \sigma)$$

Equation 10

There is also considerably difficulty in performing chemical shift calculations for the halogens, or for ^{13}C directly bonded to halogens[26]. The main difficulty in accurately predicting the chemical

shifts values for ^{19}F, is that the chemical shift range for ^{19}F is considerably larger than for ^{13}C, as an accuracy of below 1% of the total chemical shift range is considered acceptable. For ^{19}F this would mean that a chemical shift error of ± 2 ppm, and when the peaks for OFN are separated by a total of 6.3 ppm this could lead to some uncertainty of the peaks assignment.

The effect of geometry optimisation as well as a comparison between the two different functionals can be seen in **Figure 73**. It is immediately clear that the chemical shift calculations for the crystal structure obtained from the Cambridge Structural Database via X-Ray analysis are not in good agreement with the experimental data. This variation clearly shows that performing geometry optimisation is having an effect on the crystal structure. This was to be expected as crystal structure as determined by XRD had a poor fit.

The major issues with the predicted chemical shift are that there are not well defined α and β regions as for the experimental data. Also the chemical shift calculations do not predict a symmetric distribution as in the case of the experimental, meaning confidence in the calculated shifts is low. Interestingly the predicted chemical shifts for the two functionals are comparable for the X-Ray structure.

Geometry optimisation was performed on the X-Ray structure using both KT3 and PBE theory, and the resulting optimised structures used to calculate the chemical shielding tensors (see **Figure 73**). There is a significant variation in the chemical shift values of the optimised structures in comparison to the X-Ray structures, indicating a different crystal structure. The predicted chemical shifts for the optimised structure are in better agreement with the experimental data, there is however some major questions raised about their accuracy. The chemical shift range for the calculated data is significantly larger than the experimental results; 12.5 ppm compared with 6.3 ppm. Due to the significant error associated with the calculations the order can not be confidently assigned without additional evidence confirming the assignments. They correctly predict that the α resonances appear at higher (less negative) chemical shifts than the β peaks, however there is not the clear α vs. β distinction that is observed experimentally. In line with previous observations, KT3[25] absolute shielding constants (not presented) are uniformly above the PBE values.

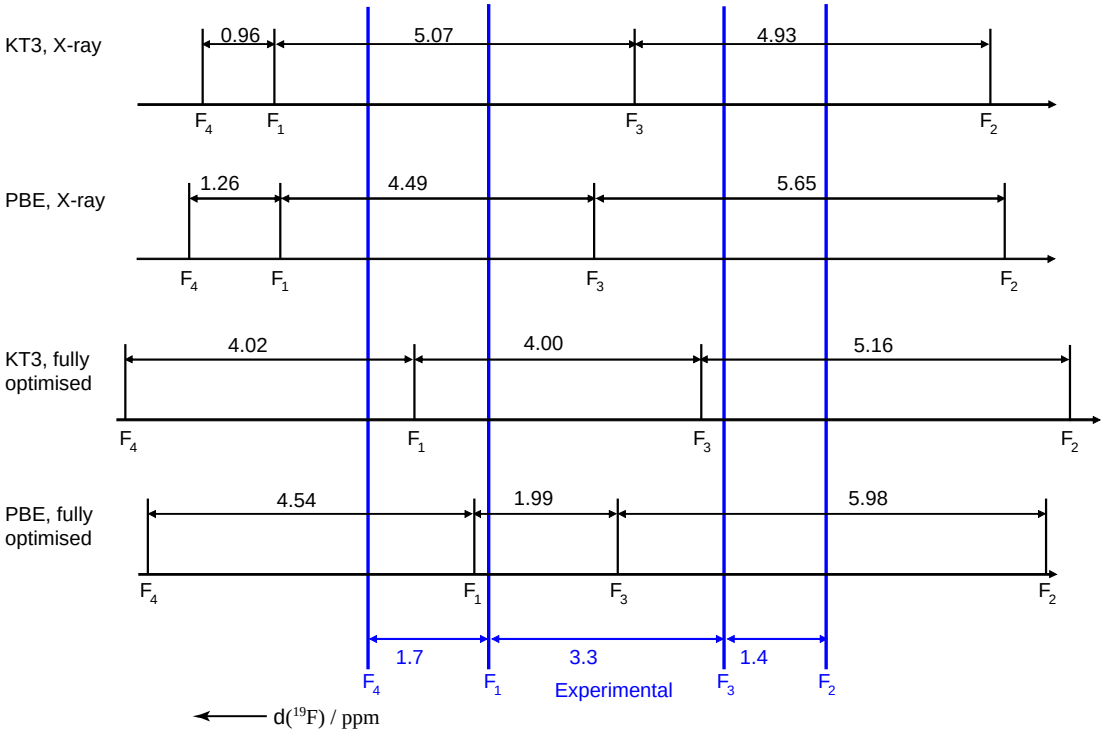

Figure 73 . Comparison of experimental chemical shifts for octafluoronaphthalene with calculated chemical shifts using both optimised and un-optimised geometries, and PBE or KT3 functionals. The mean of each set of calculated shifts has been adjusted to match the mean of the experimental values and only the separations (in ppm) between the shifts are considered

The result clearly show that calculation packages such as CASTEP are providing useful information to aid assign in NMR peaks, which would not be possible with NMR data alone[4,27]. The results also show the limitations of the DFT description for nuclei such as ^{19}F, however the confidence in the calculations is increased compared with previous chemical shift calculations[28-31]. To assign the peaks confidently it is necessary to combine the calculated data with the 2D correlation experiment, to see if a good agreement can be achieved.

The 2D correlation spectrum shows that there is a strong correlation as expected between the two α sites and the two β sites, the interesting couplings are the α–β couplings. From **Figure 67 (b)** it is expected for there to be a strong coupling between ^{19}F sites F1 and F2, and also F3 and F4, and no couplings are to be expected for F1 and F3 and also F2 and F4. In **Figure 67** there is no correlation see between the peaks which relate to F1 and F3, and also F2 and F4, showing good agreement between the NMR and computational data.

In conclusion, it is not possible to assign the peaks for OFN by using just NMR or calculated chemical shifts alone with current techniques. Combining the NMR correlation experiment with the quantum chemistry calculations provides reassurance in the ordering of the peaks, even with the associated errors with the calculations. This leads to the confident assignment of peaks in **Table 2**.

Experimental shift / ppm	Calculated shift* / ppm	Site label
–147.8	–147.5	F4
–149.3	–148.9	F1
–152.8	–153.2	F3
-–154.1	–158.6	F2

Table 2 Assignment of ^{19}F resonances to crystallographically distinct fluorine sites using labelling scheme of Fig. 1 a). *Mean of values adjusted to experimental value.

6.5 Conclusions

The ^{19}F NMR of OFN has been revisited in light of new developments in solid-state NMR, such as faster MAS rate to reduce dipolar couplings that are prominent for moderate MAS rates. Also high field magnets have made ^{19}F a more favourable NMR nucleus with the reduction of the Bloch-Siegert effect[32], as well as better resolution.

At high MAS rates it has been seen that the 'natural' linewidth is dominated by an inhomogeneous contribution, i.e. most of the ^{19}F signal is refocused by a spin echo. This inhomogeneous linewidth could be largely attributed to the large anisotropy of the bulk magnetic susceptibility (ABMS) expected for this material (due to the aromatic stacking within the crystal structure). Due to this large ABMS contribution the resolution of the spectrum was enhanced on the addition of material with a low ABMS (NaCl). This phenomenon has favourable consequences for the detection of low concentration of materials in formulated products, although deliberate sample dilution is not a generally practical solution to improving linewidths due to the unpredictable effects from sample to sample.

The large inhomogeneous contribution has little effect in 1D spectrum apart from poorer signal to noise and resolution associated with the broader lines. This broadening can be well resolved in 2D correlation experiments, which can provide additional information. These correlations can be easily overlooked due to t_1 ridges. In addition, a lineshape transformation that gives a more Gaussian character of the 2D lineshape, not only improves the resolution but also makes any correlation due to the inhomogeneous contribution easier to detect.

In order for efficient lineshape transformation a suitable value of line broadening should be used, in general a value relating to the inhomogeneous linewidth is a suitable starting point. This is an

important point if the correlation spectrum is being used to provide structural information, such as bond angle distribution.

The combination of DFT calculations with correlation experiments have proven to be invaluable in assigning the peaks for OFN. The agreement between experiment and calculated chemical shifts for individual sites show predicted shifts have an accuracy of around 1% of the total chemical shift range (~2 ppm), which is significantly poorer than the experimental resolution. There are clear systematic discrepancies between the calculated and experimental chemical shifts, meaning that it is not possible to assign the peaks with just calculated data alone.

Using just a simple homonuclear correlation experiments readily identifies the sites that are in close proximity with a sufficiently short mixing time, however this is unable, by itself, to provide an absolute assignment of the peaks to sites in the crystal structure. However if the two techniques are combined it is possible to confidently assign each of the ^{19}F resonances to sites within the crystal structure. Co-workers have recently made other demonstrations of the effective combination of DFT calculation and connectivity (rather than proximity) relationships provided by the solid-state NMR variant of the INADEQUATE experiment[27]. By combining the two techniques it has been possible to assign the chemical shifts to identified ^{13}C sites for α-testosterone, which contains two molecules per asymmetric unit cell.

The geometry optimisation of the OFN crystal structure has also highlighted the sensitivity of solid-state NMR to detecting variations in the local structure of the molecule. The effect on the calculated chemical shifts before and after geometry optimisation showed this very clearly. It also highlighted the difficulty that X-Ray diffraction techniques have with determining structures of systems with a considerable amount of motion within them.

For systems with relatively large amounts of motion present, it may be possible to gain a more accurate crystal structure with geometry optimisation performed. Using the CASTEP program it is then possible to make a direct comparison between the structure before and after geometry optimisation with that of the solid-state NMR data. This would then give an idea if the optimised crystal structure is in fact a more representative crystal structure.

6.6 References

(1) Mehring, M.; Griffin, R. G.; Waugh, J. S. *J. Chem. Phys.* **1971**, *55*, 746.

(2) Harris, R. K.; Jackson, P.; Nesbitt, G. J. *J. Magn. Reson.* **1989**, *85*, 294-302.

(3) Pawley, G. S.; Dietrich, O. W. *J. Phys. C: Solid State Physics.* **1975**, *8*, 2549-2558.

(4) Profeta, M.; Mauri, F.; Pickard, C. J. *Journal of the American Chemical Society* **2003**, *125*, 541-548.

(5) Othman, A.; Evans, J. S. O.; Evans, I. R.; Harris, R. K. *J. Pharm. Sci.* **2007**, *32*, 1796.

(6) Vanderhart, D. L.; Earl, W. L.; Garroway, A. N. *J. Magn. Reson.* **1981**, *44*, 361-401.

(7) Brown, S. P.; Spiess, H. W. *Chem. Rev.* **2001**, *101*, 4125-4155.

(8) Zorin, V.; Hodgkinson, P.; Brown, S. P. *J. Chem. Phys.* **2006**.

(9) Garroway, A. N.; VanderHart, D. L.; Earl, W. L. *Phil. Trans. R. Lond. A* **1981**, *299*, 609-628.

(10) Alla, M.; Lippmaa, E. *Chem Phys Lett* **1982**, *87*, 30.

(11) Klymachyov, A. N.; Dalal, N. S. *Z Phys B: Condens Matter* **1997**, *104*, 651.

(12) Lesage, A.; Duma, L.; Sakellariou, D.; Emsley, L. *J. Am. Chem. Soc.* **2001**, *123*, 5747-52.

(13) Sakellariou, D.; Brown, S. P.; Lesage, A.; Hediger, S.; Bardet, M.; Meriles, C. A.; Pines, A.; Emsley, L. *J. Am. Chem. Soc.* **2003**, *125*, 4376-80.

(14) Zorin, V. E.; Brown, S. P.; Hodgkinson, P. *Molecular Physics* **2006**, *104*, 293-304.

(15) Bennett, A. E.; Rienstra, C. M.; Griffiths, J. M.; Zhen, W.; Lansbury, P. T.; Griffin, R. G. *J Chem Phys* **1998**, *108*, 9463.

(16) Scheler, U. *Bull. Magn. Reson.* **1999**, *19*, 52.

(17) Wormald, P.; Apperley, D. C.; Beaume, F.; Harris, R. K. *Polymer* **2003**, *44*, 643.

(18) Jeener, J.; Meier, B. H.; Bachmann, P.; Ernst, R. R. *J. Chem. Phys* **1979**, *71*, 4546.

(19) Claridge, T. D. W. *High resolution NMR techniques in organic chemistry*; Pergamon, **1999**.

(20) Ferrige, A. G.; Lindon, J. C. *J. Magn. Reson.* **1978**, *31*, 337-340.

(21) Freeman, R. *A Handbook of Nuclear Magnetic Resonance*; Longman Scientific and Technical, 1987.

(22) Segall, M. D.; Lindan, P. J. D.; Probert, M. J.; Pickard, C. J.; Hasnip, P. J.; Clark, S. J.; Payne, M. C. *Journal of Physics-Condensed Matter* **2002**, *14*, 2717-2744.

(23) Robbins, A. J.; Ng, W. T. K.; Jochym, D.; Keal, T. W.; Clark, S. J.; Tozer, D. J.; Hodgkinson, P. *Phys. Chem. Chem. Phys.* **2007**, *9*, 2389.

(24) Perdew, J. P.; Burke, K.; Ernzerhof, M. *Phys. Rev. Lett.* **1996**, *77*, 3865.

(25) Keal, T. W.; Tozer, D. J. *J. Chem. Phys* **2004**, *121*, 5654.

(26) Gryff-Keller, A.; Molchanov, S. *Mol. Phys.* **2004**, *102*, 1903-1908.

(27) Harris, R. K.; Joyce, S. A.; Pickard, C. J.; Cadars, S.; Emsley, L. *Phys. Chem. Chem. Phys.* **2006**, *8*, 137-143.

(28) Allen, M. J.; Keal, T. W.; Tozer, D. J. *J. Chem. Phys. Lett.* **2003**, *380*, 70.

(29) Chan, J. C. C.; Eckert, H. *J. Mol. Struct* **2001**, *535*, 1.

(30) Patchkovskii, S.; Autschbach, J.; Ziegler, T. *J. Chem. Phys* **2001**, *115*, 26.

(31) Poater, J.; van Lenthe, E.; Baerends, E. J. *J. Chem. Phys* **2003**, *118*, 8584.

(32) Bloch, F.; Siegert, A. *Physical Review* **1940**, *57*, 522 LP.

7 Appendices

7.1 Appendix 1Solid-state NMR as an aid to crystal structure determination

7.1.1 Introduction

A common problem for the pharmaceutical industry is the accurate crystal structure determination of the proposed drug candidates. The method of choice to determine the crystal structure is single crystal X-ray diffraction (XRD), which relies on high quality single crystals being prepared. These single crystals are exposed to a beam of monochromatic X-rays and the patterns of the diffracted beams are recorded. These may be used to solve the structure relatively easily.

Problems arise with the inability of some compounds to form large enough single crystals for analysis. In this situation, powder XRD must be used, which greatly increases the difficulty of structure determination. The difficulty arises as a result of all crystal orientations being present within the powder, compared to only one for single crystals. Each crystal orientation gives its own diffraction pattern, and individual 'spots' as seen by single-crystal XRD becomes spread out into rings of diffracted intensity for powders. The intensities of these rings can be measured by scanning a point or 1D line detector across a narrow strip of the rings.

The inherent problem with powder XRD is that the 3D intensity distribution of a single crystal experiment is compressed onto a 1D of 2θ space, leading to a major loss of information and greatly increased likelihood of peak overlap. One method to improve powder XRD techniques is the use of high resolution X-rays, where the frequency of the X-rays is controlled more closely by a monochromater. The drawback is that a higher percentage of X-rays are 'filtered' out in the process and the technique becomes less sensitive. The advantage however to this method is that the peaks can be better resolved making structure determination less challenging.

The most commonly used method for determining crystal structure from powder patterns currently is the Rietveld refinement[1], where an approximate starting crystal structure is used. This potential structure has its diffraction pattern calculated and compared to experimental

data. The molecule/s position within the crystal structure is then adjusted. For each new position an examination of the observed and calculated pattern is performed until a good agreement is observed between the two patterns.

Reitveld refinement is an efficient method in determining crystal structures provided a suitable starting position is defined and a diffractogram of high enough quality is used. If however the molecules are not in a suitable starting position, then due to the increased number of degrees of freedom compared to single crystal XRD it is unlikely a suitable crystal structure will be calculated.

By combining powder XRD diffractograms with suitable NMR experiments it is hoped that the structure determination step can be speeded up. The NMR data can be used in one of two ways, either the NMR constraints can be included as penalties within the Rietveld refinement, or the NMR data can be used to discard implausible crystal structures.

From the powder data, a good estimate as to the unit cell will be known, but the orientation of the molecules within the unit cell will not be obvious. By combining the XRPD data with the NMR data it is hoped that the molecule(s) can be arranged within the molecule in a suitable starting position. This could lead to a more rapid structure elucidation or even solving crystal structures that were not possible with powder XRD alone.

7.1.2 The REDOR experiment

Dipolar couplings are a through-space interaction i.e. no bonds are involved, and are inversely proportional to the distance cubed (see **Equation 11**). From **Equation 11** it is possible to see that the dipolar coupling is directly proportional to the gyromagnetic ration of the two nuclei involved. This is why ^{19}F is a good nucleus for REDOR experiments as it has a high gyromagnetic ratio, comparable to that of ^{1}H; therefore it should be easier to measure larger distances compared to less nuclei with lower gyromagnetic ratios i.e. ^{13}C and ^{15}N.

$$d_{12} = \frac{\hbar \mu_o}{4\pi} \frac{\gamma_1 \gamma_2}{r^3}$$

Equation 11 shows how dipolar coupling is inversely proportional to the cube of the distance, where ħ is Planck's constant, μ_o is the permittivity of free space, γ are the respective gyromagnetic ratios and *r* is the distance between the two nuclei.

Rotational-Echo Double-Resonance (REDOR)[2-4] is the most common experiment for re-introducing heteronuclear couplings, where the couplings are between two different spin

types. The pulse sequence consists of a train of rotor-synchronised π pulses, which disrupt the averaging of the heteronuclear couplings by MAS (see **Figure 74**).

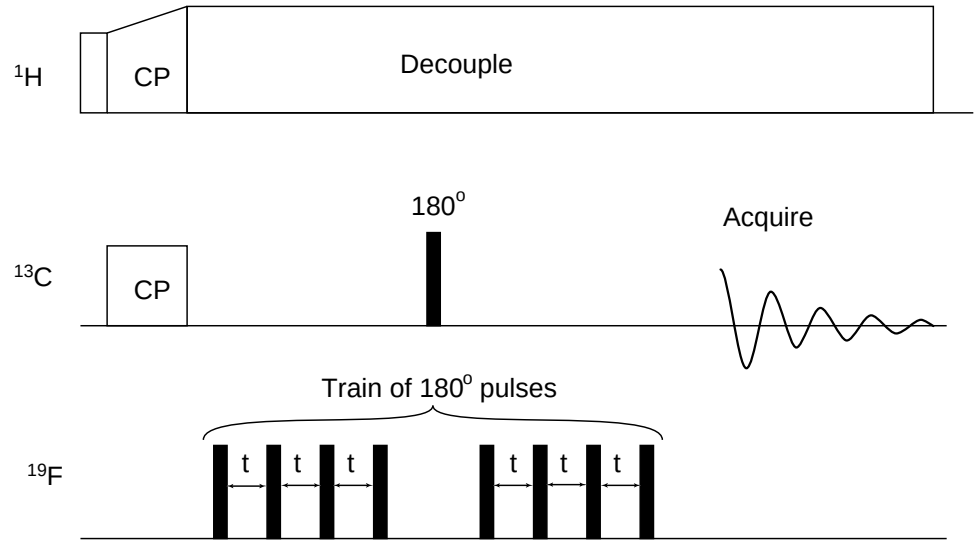

Figure 74 Pulse sequence of the REDOR experiment. Magnetisation is initially transferred from ^{1}H to nucleus of interest, typically ^{13}C. The dipolar couplings are re-introduced by placing a series of rotor synchronised 180° pulses on the ^{19}F channel, until the signal can be detected. A 180° pulse is placed on the ^{13}C channel to refocus any inhomogeneous evolution.

As the magnetisation for ^{13}C precesses about the *z*-axis, a series of 180° pulses that are rotor synchronised are applied on the ^{19}F channel simultaneously. The effect of the 180° is that at the end of the rotor cycle the dipolar couplings between the ^{13}C and ^{19}F nuclei are now only partially averaged, with the dipolar couplings being reintroduced.

The larger the ^{13}C-^{19}F coupling is the more efficient the relaxation process is in comparison to a reference signal. The 'REDOR dephasing' is time dependent as at the start of the re-coupling pulses the intensity of the echo and REDOR pulse sequence are identical. The difference in intensity brought about by the 'REDOR dephasing' can be plotted with respect to the duration of the recoupling period. This is then used to calculate the effective dipolar coupling.

7.1.3 Measuring ^{13}C-^{19}F distances by in SSNMR by REDOR

The main problem associated with any non-selective re-coupling experiment is that it can not measure a specific coupling, rather the sum of all the couplings present, in this case ^{13}C-^{19}F. When a coupling is measured it will consist of both intra and intermolecular couplings

(see **Figure 75**). (As the couplings are inversely proportional to distance cubed the total coupling will be dominated by nucleus in closest proximity to the nucleus being detected, i.e. the strongest coupling.)

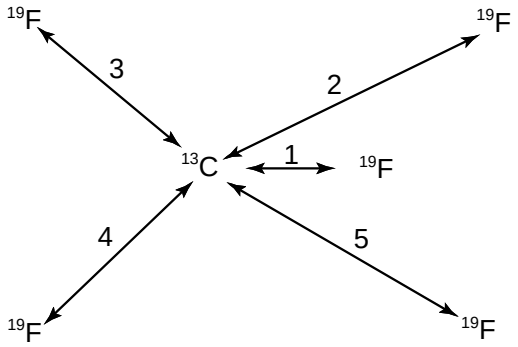

Figure 75 Schematic diagram representing the couplings present within a solid containing both ^{13}C and ^{19}F nuclei, where coupling one represents the intra-molecular couplings. It is not possible to measure a single coupling, rather the combination of all the couplings, (i.e. combination of coupling 1,2,3,4 and 5), although the closest ^{19}F-^{13}C coupling (in this case coupling 1) usually dominates the total value.

There has been a relatively large amount of work involving the REDOR experiments, with a wide variety of nuclei investigated. There has been some work trying to measure ^{13}C-^{19}F distances via REDOR experiments[5-9]although relatively little in comparison to more routine experiments such as ^{13}C-^{15}N[10,11]. There has also been some work performed that utilises the high NMR receptivity of the ^{19}F nucleus and hence coupling to other NMR nuclei.[12-16]

Previous workers[10] have used the REDOR experiment to measure well defined two spin system, where they we using a compound both ^{13}C and ^{15}N labelled. Other workers[3,17,18] have shown that when working with a singly labelled systems (^{15}N) a well-defined two spins system is not seen.

Middleton *et al* was able to distinguish between *intra* and *inter* molecular interactions when working with doubly labelled (^{15}N and ^{13}C) cimetidine[11]. The ^{15}N and ^{13}C dipolar couplings were measured initially and the compound was then 'diluted' with unlabelled cimetidine and the dipolar coupling s were measured again. The couplings that were dominated by *intra*-molecular couplings would be largely unaffected by the dilution, where couplings dominated by *inter*molecular couplings would be reduced on dilution.

For ^{19}F REDOR experiments, it is not possible to 'dilute' the system with an unlabelled form, due to the 100% natural abundance of ^{19}F. Therefore, all observed REDOR dephasing effects are going to be a combination of both *intra*- and *inter*- molecular interactions. The usefulness

of the effective dipolar couplings extracted from the REDOR results needs to be assessed due to this complicated mixture of interactions. Working alongside Alan Sage at the University of Durham the sensitivity of ^{13}C-^{19}F dipolar couplings was calculated for thirty ^{19}F containing organic compounds. The shortest ^{13}C-^{19}F distance was plotted against the overall coupling (see **Figure 76**).

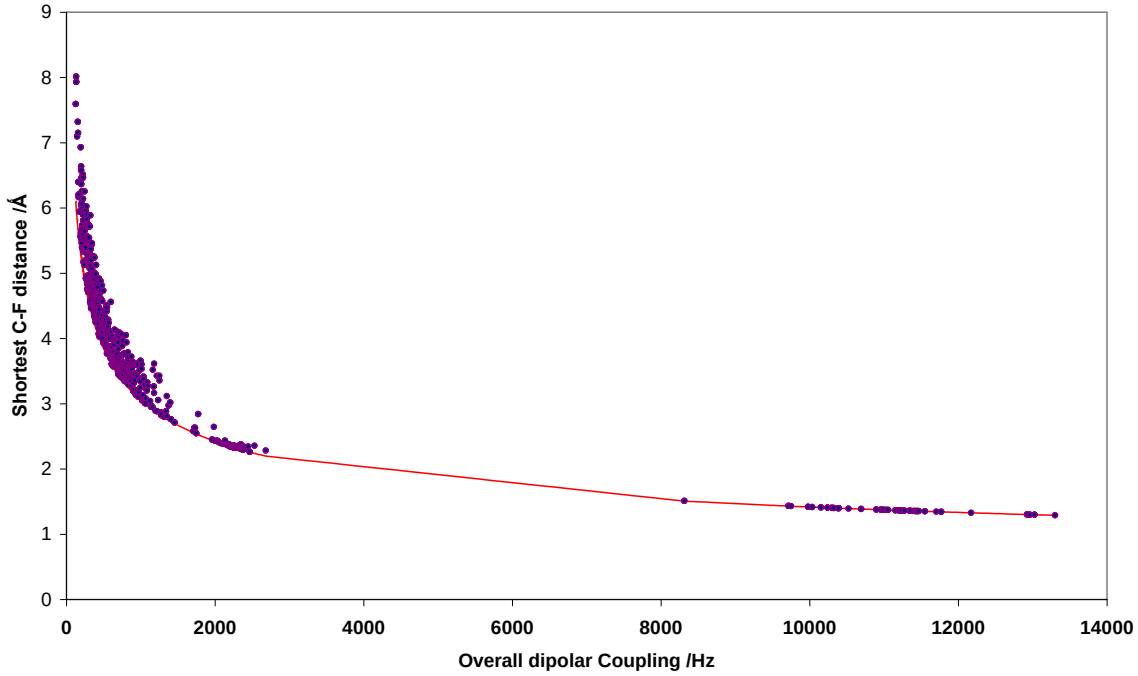

Figure 76 Plot of effective dipolar coupling with respect to closest ^{13}C-^{19}F distance for 30 compounds from the Cambridge Structural Database (CSD). The red line indicates the theoretical coupling for a particular distance, and is proportional to $1/r^3$

The plot was produced by first selecting 30 fluorine containing organic compounds from the Cambridge Structure Database (CSD). For each structure a super cell was created, which was a 3 x 3 x 3 unit cell, which was then converted into *xyz* coordinates. From the *xyz* coordinates, it was possible to calculate the shortest carbon-fluorine distance within the crystal structure and relate this to a coupling. It was also able to calculate the overall ^{13}C-^{19}F coupling that would be measured for that particular ^{13}C site.

Figure 76 shows that for short ^{13}C-^{19}F distances, e.g. carbon fluorine bonds, there is a very large coupling present, which dominates the total coupling. These couplings are generally above 8 kHz and all the points in **Figure 76** lie on the line representing the theoretical coupling. As expected there is a larger scatter of results for the smaller couplings as they will be affected greater by additional couplings present

From **Figure 76** it can be seen that as expected there are a large range of coupling values for ^{13}C-^{19}F containing compounds, ranging from a few hundred hertz to tens of kilohertz. The very large couplings, that is ones larger than 3 kHz are generally of little use as there is relative little variation from polymorph to polymorph since these are dominated by short intramolecular distances and so will be comparable for the two forms. It will also be difficult to measure the difference experimentally.

Likewise, couplings that are below 500 Hz are of little use as from **Figure 76** it can be seen that there is a significant range in the shortest ^{13}C-^{19}F distances. This range makes it difficult to associate them with individual internuclear distances. Also there is the added complication of actually being able to detect this coupling, due to the relatively long time it takes for weak coupling to affect the intensity of the ^{13}C peaks (10's ms). During this time T_2 relaxation is occurring, resulting in a continuous loss of signal, meaning the REDOR effects disappear into noise.

The couplings that are generally of greater use are those between 0.5 kHz and 3 kHz. For crystal structure determination, it is the inter-molecular distances that are of interest i.e. the medium strength couplings, as these will be affected greater by variations in the packing of the molecules.

For the weaker couplings there is still a strong correlation with respect to the closest ^{13}C-^{19}F distance (see **Figure 77**), even though there is some uncertainty on the exact distance. For example, from **Figure 77** a coupling of 500 Hz relates to a distance of between 4-5 Å, due to the combination of ^{13}C-^{19}F couplings. From the data is does appear as though ^{13}C-^{19}F couplings could be used as a constraint, to aid structure determination. Below a certain coupling (for this work I have said 200 Hz) it would be difficult to measure any REDOR dephasing effects, this results in the couplings of average strength that are of interest.

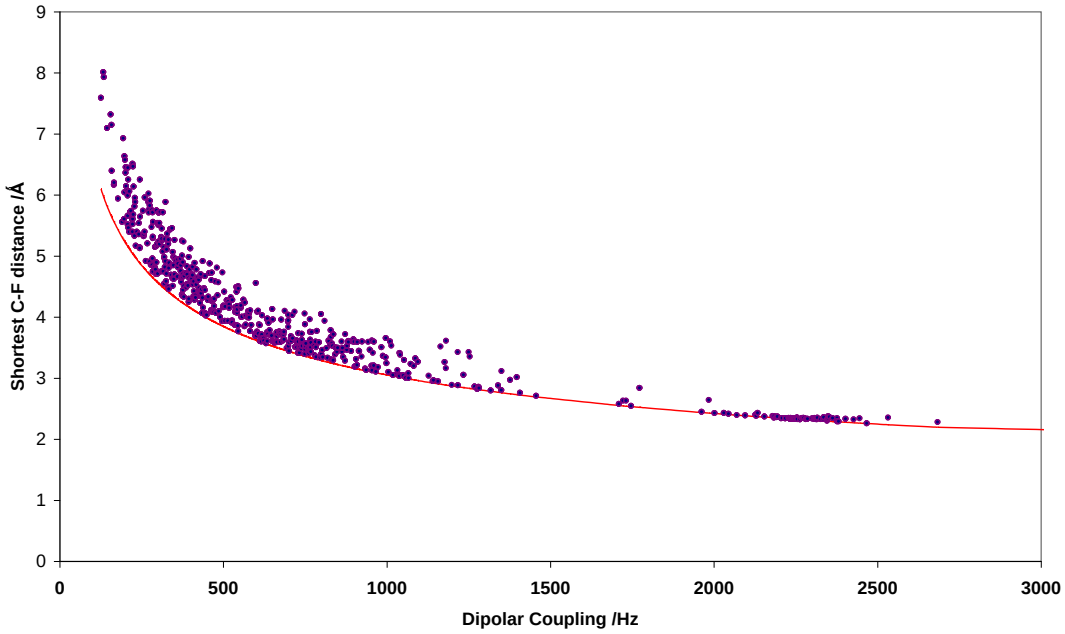

Figure 77 Plot as in **Figure 76** but focused on weaker dipolar couplings, which are more sensitive to variation in the crystal packing

This data suggests that ^{13}C-^{19}F REDOR results could be used to differentiate between dipolar coupling strengths. Although the effective couplings could not be converted into an accurate distance due to the sum of all the other couplings, they however can be used to provide distance constraints, which could be used to speed up structure determination via powder XRD.

In solution state NMR, structure elucidation is usually performed with the NOESY experiment, which uses lots of quite poorly defined distances. In contrast, the REDOR experiment tries to measure a small number (usually one or two) accurate distances. We are trying to measure a good number of moderately accurate ^{13}C-^{19}F constraints, which can be used to aid structure elucidation.

NMR is commonly used to determine protein conformation[19,20], where 'connectivity' information is obtained via a 2D experiment, which can then be used to predict how the protein has 'folded'. NMR can be used in the structural determination of proteins, as it can be difficult to grow single crystals that are suitable for single crystal XRD. For protein structure determination the primary structure is known, it is how the protein folds that is of interest. The folding of the protein can be determined by using NMR correlation experiments.

7.1.4 Dipolar coupling measurements of AstraZeneca pseudo-polymorphs

AstraZeneca supplied two pseudo-polymorphs of a pharmaceutically-active compound, an anhydrous and a monohydrate form. The compound contained a single ^{19}F, and the crystal structures of the two pseudo-polymorphs were sufficiently different to allow differences in the ^{13}C-^{19}F couplings to be measured. Along with the raw drug substance, an electronic representation of the crystal structures was also supplied, from which the overall dipolar couplings for each ^{13}C site could be calculated. The crystal structures were supplied in order to test the principle of being able to measure a difference in the dipolar couplings between the two systems.

From the supplied crystal structures (see **Figure 78** and **Figure 79**) it is clear to see that there are subtle variations in the arrangement of the molecules in the unit cell. This leads to small variations in the ^{13}C chemical shifts, making solid-state NMR a suitable technique for differentiating from two polymorphic forms. The different arrangement of the molecules also affects the ^{13}C-^{19}F couplings for the two forms, and it is this difference that is of interest.

It is not obvious that the dipolar couplings will vary significantly for the two forms, as the REDOR experiments measures the total coupling present. If the calculated couplings for the two forms showed that there was little difference, it is obvious that there would be little point in trying to measure the couplings via the REDOR experiment.

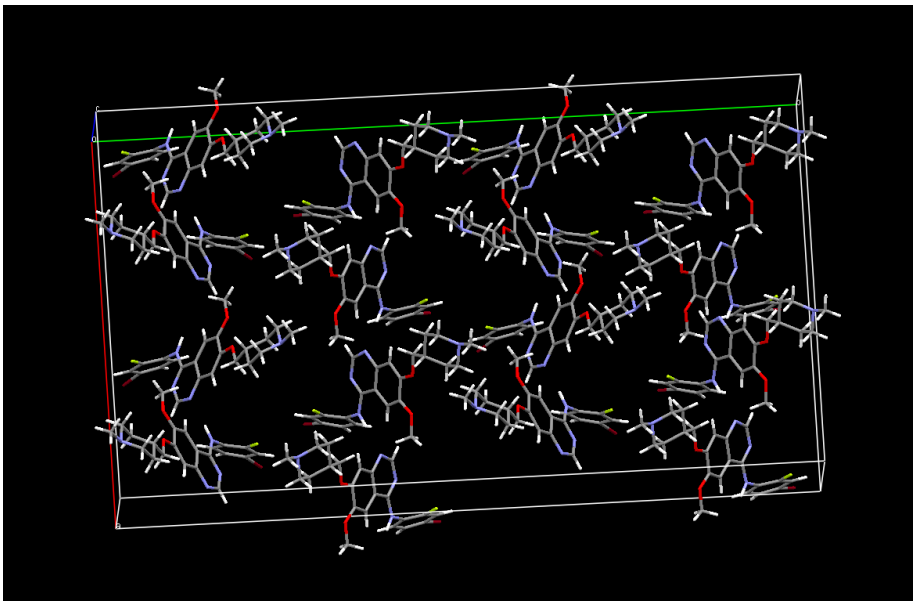

Figure 78 Crystal structure of anhydrous pseudo-polymorph of AstraZeneca compound.

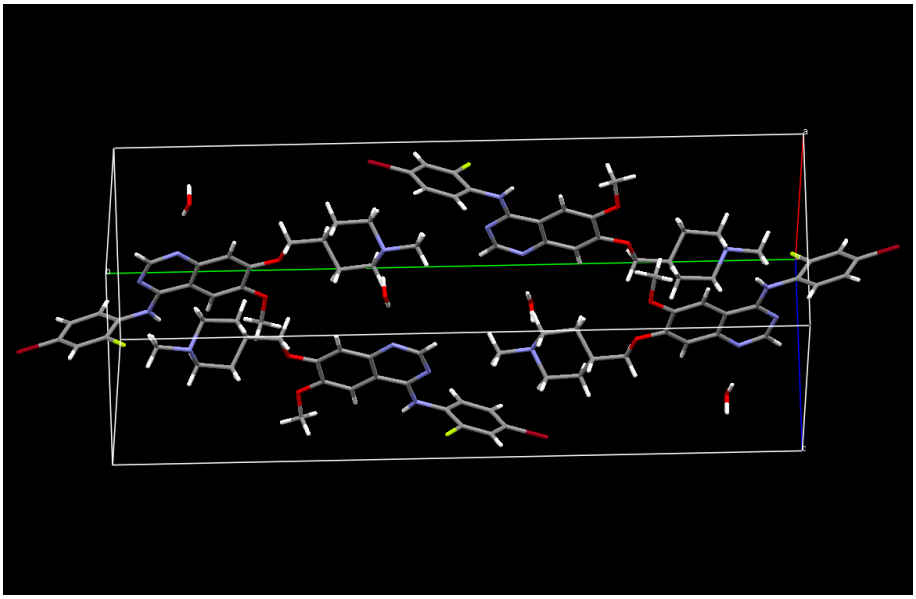

Figure 79 Crystal structure of the monohydrate pseudo-polymorph.

The couplings were calculated as for the CSD compounds by first creating a 'super-cell', which consisted of a series of unit cells in all three dimensions, typically 3 x 3 x 3. Using this super-cell the ^{13}C-^{19}F root sum square couplings (d_{rss}) were calculated for all the ^{13}C atoms in a specific molecule within the central unit cell.

Calculating the ^{13}C-^{19}F dipolar couplings for each carbon site and comparing the two pseudo-polymorphs would show if it would be possible to detect a difference in the overall pattern of dipolar couplings for the two pseudo-polymorphs.

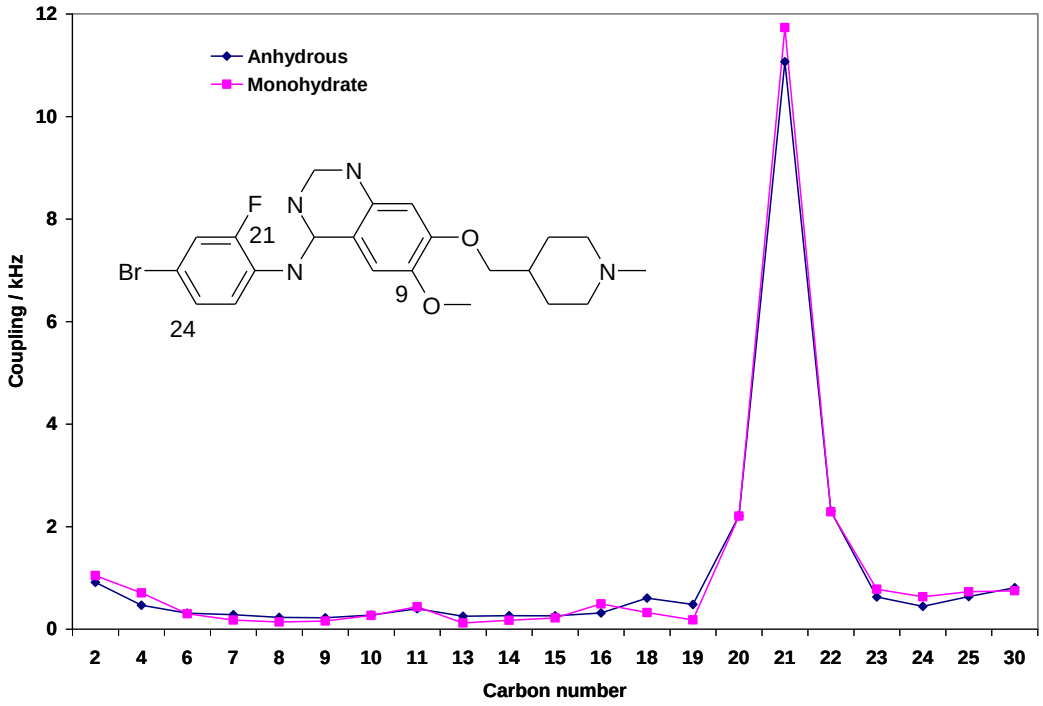

Figure 80 Comparison of effective ^{13}C-^{19}F dipolar couplings for the two forms of the AstraZeneca compound. The couplings in this case are dominated by the ^{13}C-^{19}F bond, making it difficult to detect difference in couplings.

In **Figure 80** the plot is dominated by the C-F bond, which has a coupling of over 10 kHz. As mentioned previously this can be effectively ignored as the bond length is not going to vary a significant amount. For this work it is the medium strength intra molecular couplings of interest, as these will vary sufficiently for each compound but also allow ease of detection. There are cases where *intra*-molecular bonding can provide useful information such as for cimetidine[10], but these tend to be the exception.

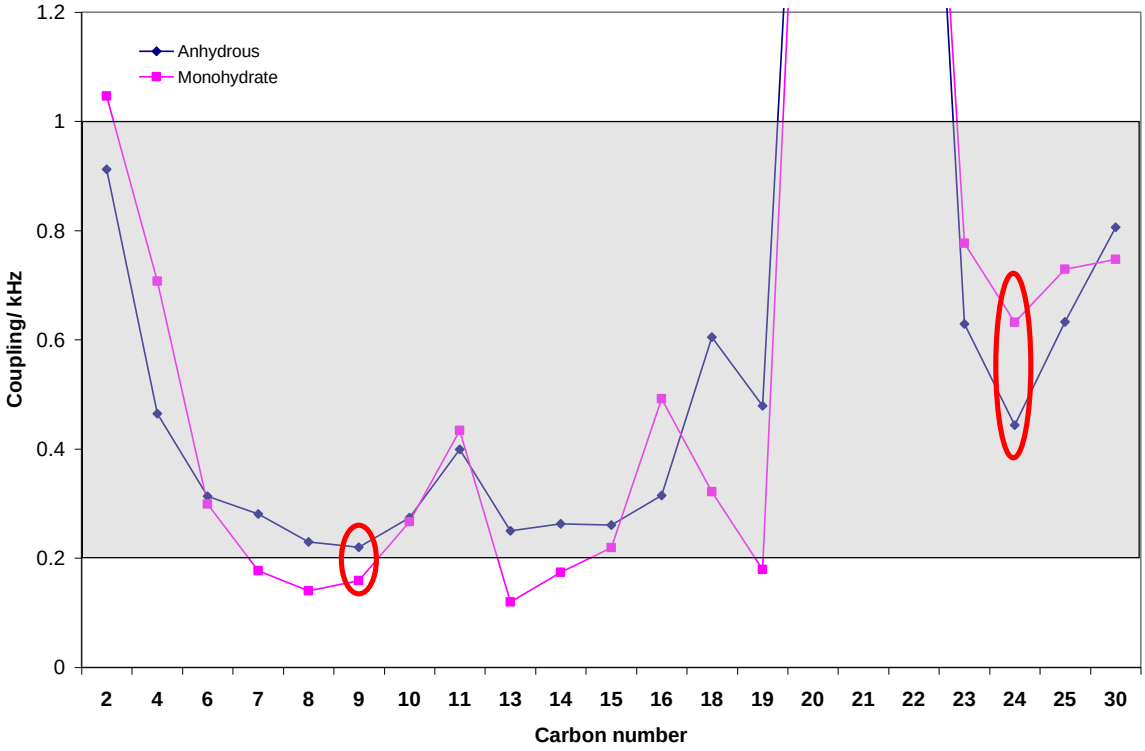

Figure 81 Comparison of the weak dipolar couplings for the AstraZeneca compound, the grey banded area indicates the area of interest. Couplings above and below this will provide little or no structural constraints. Also couplings below 200 Hz will be challenging to measure as mentioned earlier. It important to stress that these couplings are theoretical and do not take motion within the molecule into consideration, which will have an effect.

It can be clearly seen that there are a number of significant variations in the couplings for the two polymorphs. The grey band represents the area in which the couplings need to appear to be of use; couplings of particular interest are for ^{13}C sites 4, 18, 19 and 24. Couplings above 1 kHz tend to be ^{13}C that are *intra*-molecularly coupled and will not vary enough to be detected. Couplings below 200 Hz will simply be difficult to be detect, as the signal will not have time to dephase as a result of the dipolar couplings before the NMR signal has decayed.

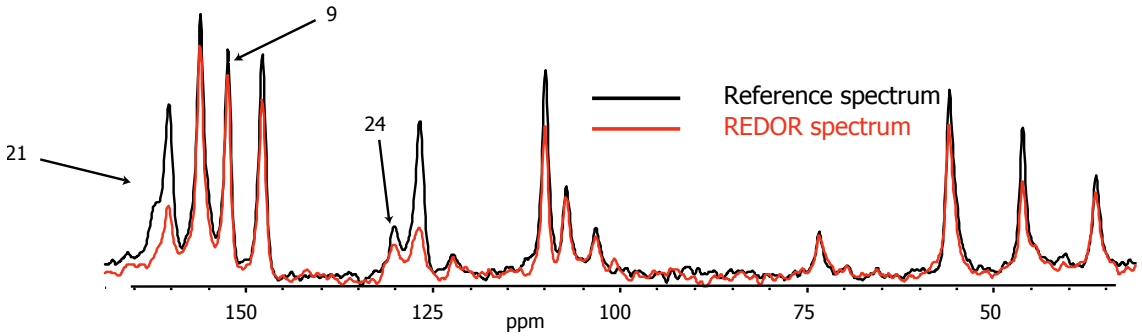

Figure 82 Actual REDOR spectra for AstraZeneca compound. When the ^{13}C strongly interacts with neighbouring ^{19}F nuclei it results in less intensity. The experiment was performed at a MAS rate of 14 kHz and a contact time of 0.5 ms, with a ^{1}H 90º being 3.6µs and the ^{19}F 180º being 7.5µs. An acquisition time of 20.48 ms used with a ^{1}H decoupling power of 62.5 kHz and 384 acquisitions recorded for each row.

As the time the re-coupling pulses are applied increases the greater the effect can be seen. Build up curves showing for each carbon site can be calculated using **Equation 12**. This produces the relative REDOR effect, which has a maximum theoretical value of one, and a minimum of zero. Generally, a value between the two extremes is seen (see **Figure 83**)

$$\frac{S_o - S}{S_o}$$

Equation 12 shows how the dephasing effect can be standardised for each site to give a 'REDOR effect', S_o is the reference intensity, that is without the re-coupling pulses, while S is the intensity with the π pulses applied.

As the main aim is to measure relative distances as opposed to absolute values, it is not necessary to calibrate the dephasing effect to exact distances. Also it would be challenging to relate the dephasing effect to an exact distance due to the range in distances that correspond to a single coupling. Simply the initial gradient of the dephasing effect will give a qualitative value, which will be sufficient in this case.

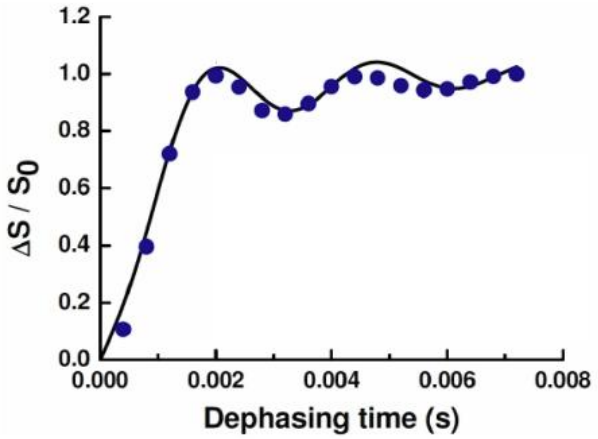

Figure 83 REDOR curve for doubly labelled ^{13}C-^{15}N glycine, where a well defined two spin system can be seen.[21]. The dephasing effect has approached the theoretical maximum of 1 for extended time

The effective REDOR couplings can be calculated by plotting the build up curves for each ^{13}C site, the greater the coupling the more rapid the build up. It is hoped that by comparing the build up curves for the two polymorphs one or more sites will show significantly different effects.

7.1.5 Results

The experiments were performed on a 4mm HFX probe due to the need to simultaneously pulse on the ^{19}F, ^{13}C and ^{1}H channel. A nutation rate of 50 kHz used for both ^{19}F and ^{1}H. The following build up curves have been selected to show clearly how the REDOR effect varies for a series of ^{13}C sites. For the REDOR experiment it is best to use as fast as possible MAS rate, in this case 14 kHz. If slower MAS rates are used, due to the need for the pi pulse to be rotor encoded, this means less points can be used before the signal decays. For each spectrum there were 384 acquisitions performed with 14 different rotor periods of 2-106, which corresponded to a time of 2ms – 15ms. Due to the number of acquisitions and rotor periods used, combined with the relatively long pulse delay (16 s), the total experiment time for each polymorph was around 40 hours.

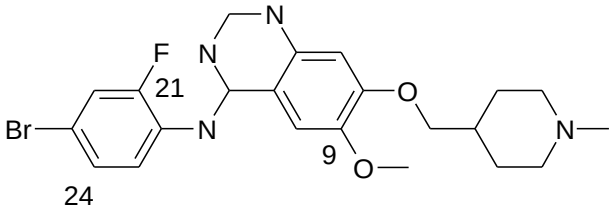

Figure 84 Structure of AstraZeneca compound, with the important carbon sites referenced.

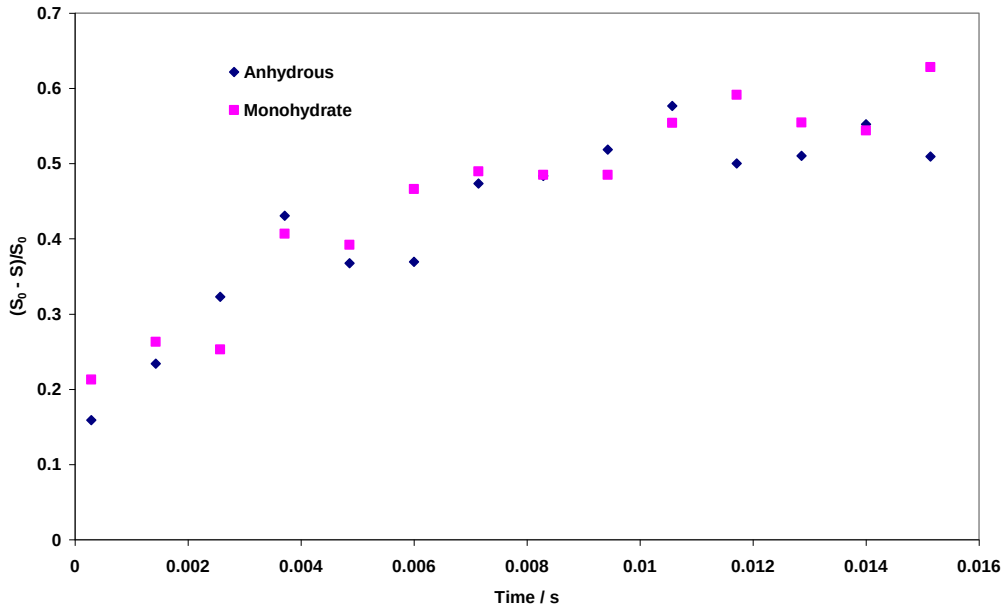

Figure 85 REDOR build up curves for ^{13}C 21

Observing the dephasing effect due to the dipolar couplings for carbon 21 (see **Figure 85**), which is the carbon directly bonded to the fluorine, shows that there is a clear build up for the two polymorphs. As mentioned previously these strong couplings are of little use as they will not very by a measurable difference from for two polymorphs. The plot shows this clearly as the dephasing effect are indistinguishable for the two polymorphs.

Looking closely at **Figure 85** the main observation is that the build up curve does not appear to pass through zero, This is due to the first signal is detected after two rotor periods, which allowed a significant decrease in the signal due to dephasing of the signal. Overall **Figure 85** shows that the REDOR experiment is working, but no other useful information can be taken from it.

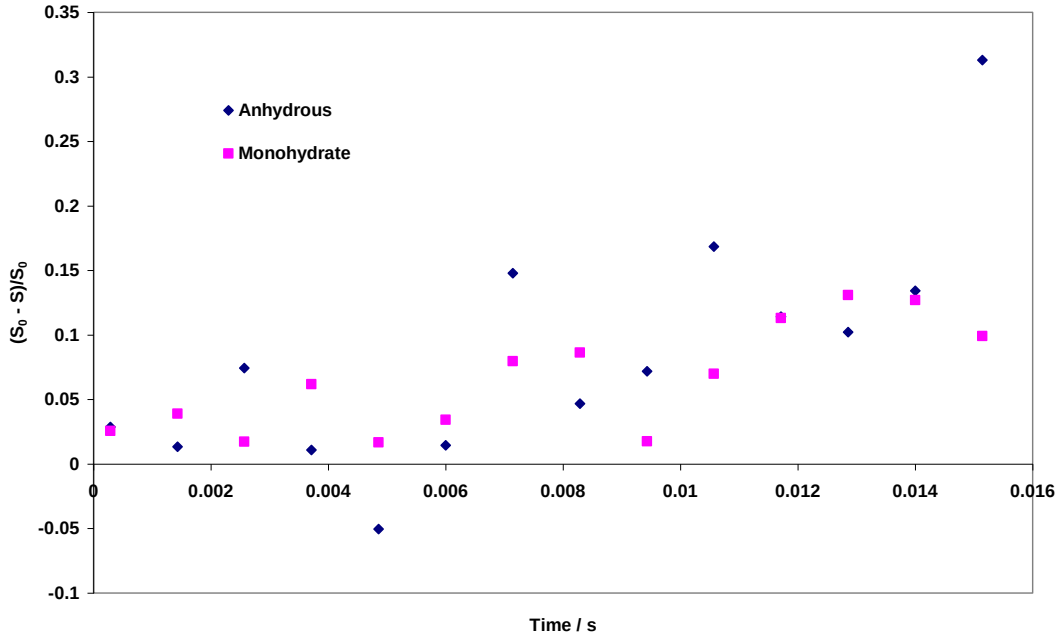

Figure 86 REDOR build up curves for ^{13}C number 9, for when there is little or no dipolar couplings between ^{13}C-^{19}F.

In contrast to **Figure 85** where there was an excessively large dipolar coupling, **Figure 86** is an example when there is a very small dipolar coupling present (~150 Hz). In fact, the dipolar couplings present are so small it is not possible to state whether there is a 'REDOR effect' present due to the noise obscuring the effect. This is of little use as it is impossible to measure a difference in the two build up curves.

Previous workers[10,11] have shown that weak couplings can be measured with the REDOR experiment, but only when working with labelled systems. Working with labelled systems allows the measurement of much weaker couplings, due to the orders of magnitude increase in sensitivity.

For the dipolar couplings to be of any use, a measurable difference needs to be observed. The previous couplings (see **Figure 85** and **Figure 86**) have shown that extreme couplings are of little use. The most useful couplings are when there is a measurable difference in the two compounds, which can be seen in **Figure 87**. Due to the nature of the ^{13}C-^{19}F couplings, it is not possible to accurately quantify the couplings for the two systems, and as the main aim of this investigation was proof of principle to see whether useful effects the couplings were estimated from the build up of the slope and check the relative sizes are reasonable.
It is clearly possible to determine at least qualitatively which ^{13}C nuclei are closer in proximity to the neighbouring ^{19}F nucleus. This could be a useful constraint to aid crystal structure determination via powder XRD. Comparing the experimental data to the predicted

couplings in **Figure 81**, shows that for the specific carbon site (24), the monohydrate has the larger ^{13}C-^{19}F couplings.

These preliminary REDOR experiments show that useful information regarding ^{13}C-^{19}F distances are being measured. Whether this distance information can be usefully incorporated into crystal structure determination from powder XRD data is currently being investigated. All REDOR build up curves can be viewed in Appendix 2.

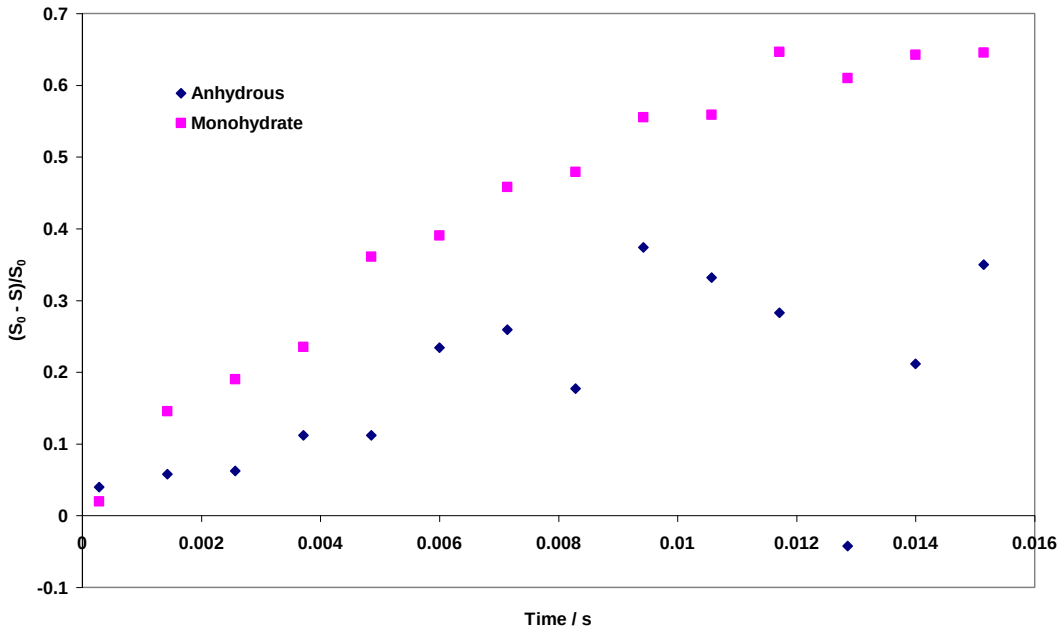

Figure 87 REDOR build up curves for ^{13}C number 24, for when there is a measurable difference in the dipolar couplings

7.1.6 Conclusions

REDOR experiments are a useful method of extracting dipolar couplings, which can be directly related to distances for well defined two spin systems, such as ^{13}C-^{15}N labelled compounds. The samples are normally labelled[11] due to the low NMR sensitivity of the two nuclei, and the system can be 'diluted' with an unlabeled form to reduce inter-molecular couplings

From the results presented, it appears as though ^{13}C-^{19}F REDOR experiments could be potentially used to aid powder XRD structure determination. This particular system proved to be difficult to investigate due to the results being on the limit of sensitivity, as a result of a combination of factors. Both systems had long T_1 which resulted in long pulse delays being used (~16 s), also the peaks were broad in ^{13}C terms (~300 Hz). A possible reason for the broad peaks is that the decoupling power had to be reduced to 50 kHz because of arcing at higher powers.

These two combining factors led to long experiments (~2 days for each run) and difficulty in measuring weak couplings, due to rapid decay of NMR signal. However, even for this system a difference was measured for the mid-range couplings, in a ^{19}F containing pharmaceutical compound. This difference could be used for future compounds to aid crystal structure determination via powder XRD.

The work contained within this chapter was performed along side an investigation to try to include penalty functions within powder XRD. This would then allow NMR data to provide constraints which could be used to aid structural determination. Work is still ongoing with XRD, in which a series of compounds have been investigated with known crystal structures comparing the success rate of structural determination with and without penalty functions.

7.1.7 Future potential work

The work is currently still on going in this technique to try to combine the two complementary techniques in order to aid crystal structure determination. Solid-state NMR experiments have shown that a difference can be observed in the ^{19}F-^{13}C couplings measured for two pseudo-polymorphs. The main problem has been combining the NMR data with the powder XRD programs to suggest suitable starting positions of the molecules within the unit cell. Future work will be focused in trying to insert suitable penalty functions into the structure determination software so that the NMR data can be efficiently used. .

By opting for a selective range of compounds, future work will try to solve their crystal structures with and without NMR data, and comparing the efficiency of the technique. This will give a better understanding on exactly how beneficial NMR data can be, and if the technique proves to be successful. It is hoped that the additional information provided by the REDOR experiments will increase the efficiency of the crystal structure determination from powder samples.

7.1.8 References

(1) Rietveld, R. D. *J. Appl. Cryst* **1969**, *2*, 65.

(2) Gullion, T. *Concepts Magn. Reson.* **1998**, *10*, 277.

(3) Gullion, T.; Schaefer, J. *J. Magn. Reson.* **1989**, *81*, 196.

(4) Gullion, T.; Vega, A. J. *Progress in Nuclear Magnetic Resonance Spectroscopy* **2005**, *47*, 123-136.

(5) Brouwer, E. B.; Challoner, R.; Harris, R. K. *Solid State Nucl. Magn. Reson.* **2000**, *18*, 37.

(6) Brouwer, E. B.; Gougeon, R. D. M.; Hirschinger, J.; Udachin, K. A.; Harris, R. K.; Ripmeester, J. A. *Phys. Chem. Chem. Phys.* **1999**, *1*, 4043.

(7) Giraudet, J.; Dubois, M.; Hamwi, A.; Stone, W. E. E.; Pirotte, P.; Masin, F. *J. Phys. Chem. B* **2005**, *109*, 175-181.

(8) Hagaman, E. W. *J. Magn. Reson. Ser. A* **1993**, *104*, 125-131.

(9) Newmark, R. A.; Webb, R. J. *J. Fluorine Chem.* **2005**, *126*, 355-360.

(10) Middleton, D. A.; Le Duff, C. S.; Peng, X.; Reid, D. G.; Saunders, D. *J. Am. Chem. Soc.* **2000**, *122*, 1161.

(11) Middleton, D. A.; Peng, X.; Saunders, D.; Shankland, K.; David, W. I. F.; Markvardsen, A. J. *J. Chem. Commun* **2002**, 1976.

(12) Goetz, J. M.; Poliks, B.; Studelska, D. R.; Fischer, M.; Kugelbrey, K.; Bacher, A.; Cushman, M.; Schaefer, J. *J. Am. Chem. Soc.* **1999**, *121*, 7500.

(13) Merritt, M. E.; Sigurdsson, S. T.; Drobny, G. P. *J. Am. Chem. Soc.* **1999**, *121*, 6070.

(14) Jack, E.; Newsome, M.; Stockley, P. G.; Radford, S. E.; Middleton, D. A. *J. Am. Chem. Soc.* **2006**, *128*, 8098-8099.

(15) Wi, S.; Sinha, N.; Hong, M. *J. Am. Chem. Soc.* **2004**, *126*, 12754.

(16) Grage, S. L.; Watts, J. A.; Watts, A. *J. Magn. Reson.* **2004**, *166*, 1-10.

(17) Nishimura, K.; Ebisawa, K.; Suzuki, E.; Saito, H.; Naito, A. *Journal of Molecular Structure* **2001**, *560*, 29-38.

(18) Fu, R. *Chem. Phys. Lett.* **2003**, *376*, 62-67.

(19) Zech, S. G.; Wand, J. A.; Mcdermott, A. E. *J. Am. Chem. Soc.* **2005**, *127*, 8618.

(20) Castellani, F.; van Rossum, B.-J.; Diehl, A.; Schuburt, M.; Rehbein, K.; Oschkinat, H. *Nature* **2002**, 98.

(21) http://nmr900.ca/images/gl.jpeg.

7.2 Appendix 2 REDOR build up for pseudo-polymorph

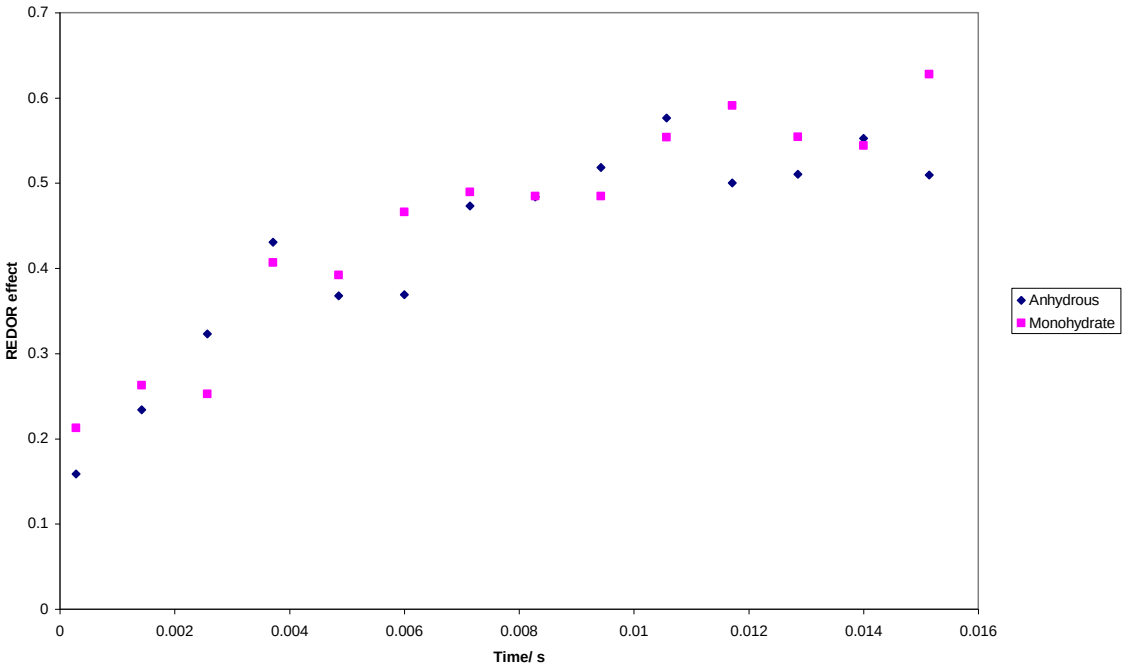

160 ppm

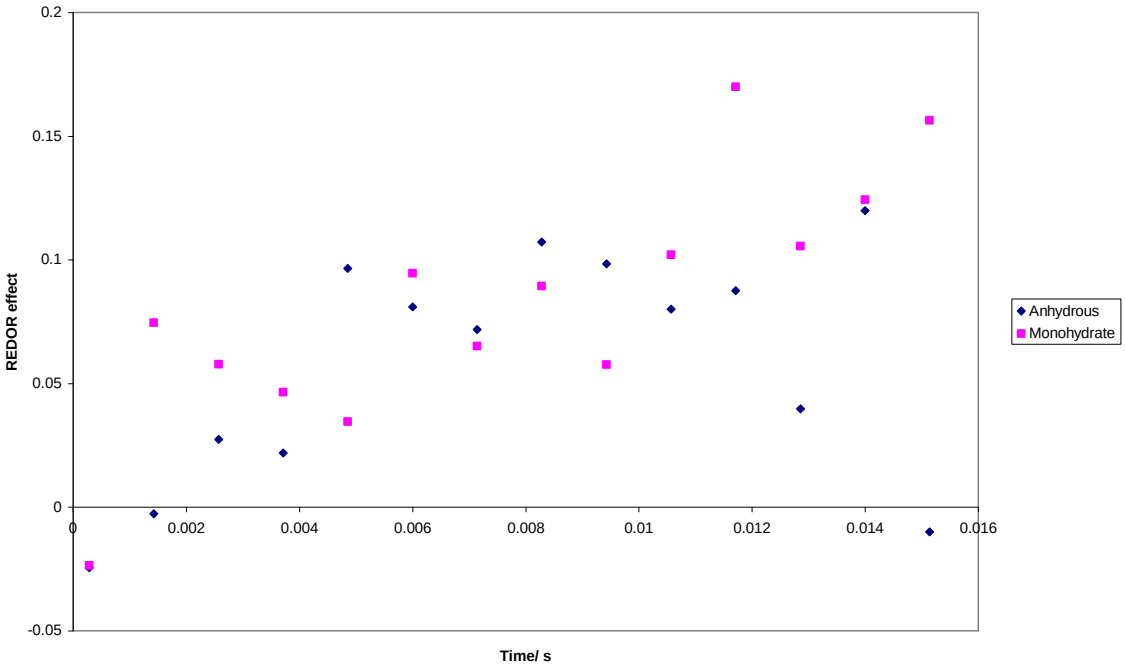

156 ppm

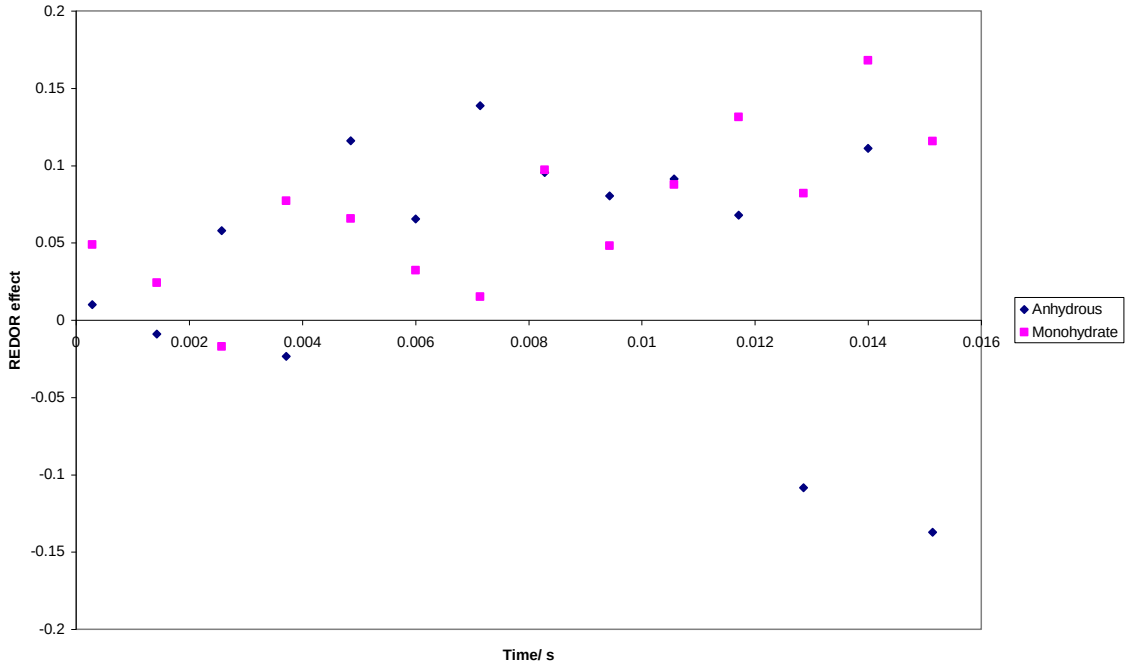

152 ppm

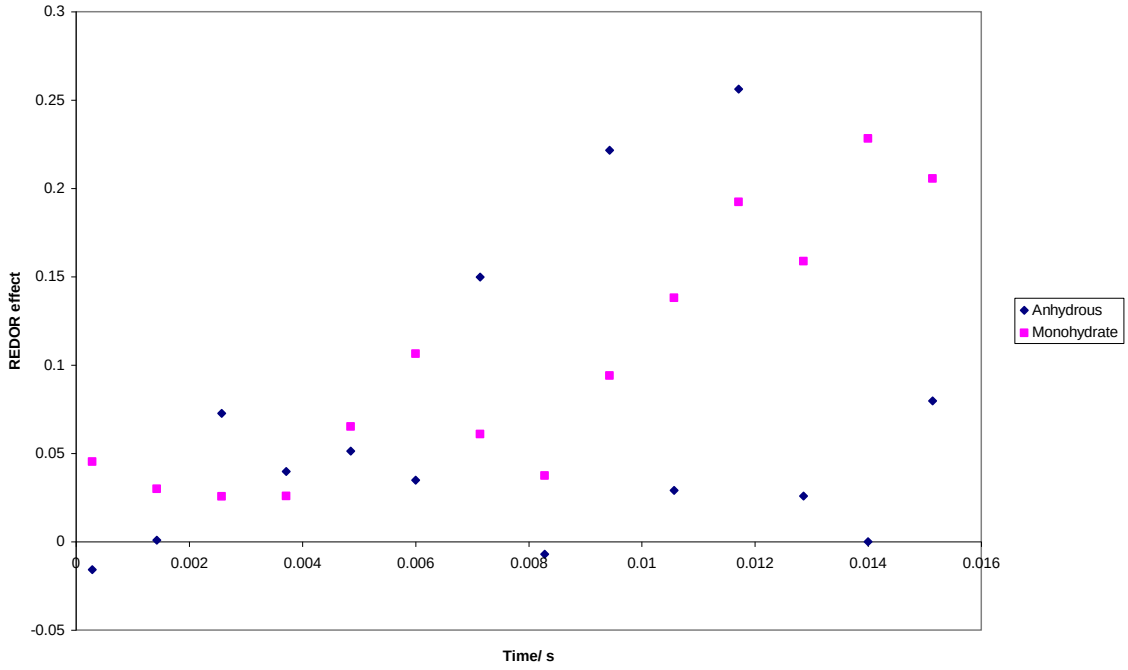

147 ppm

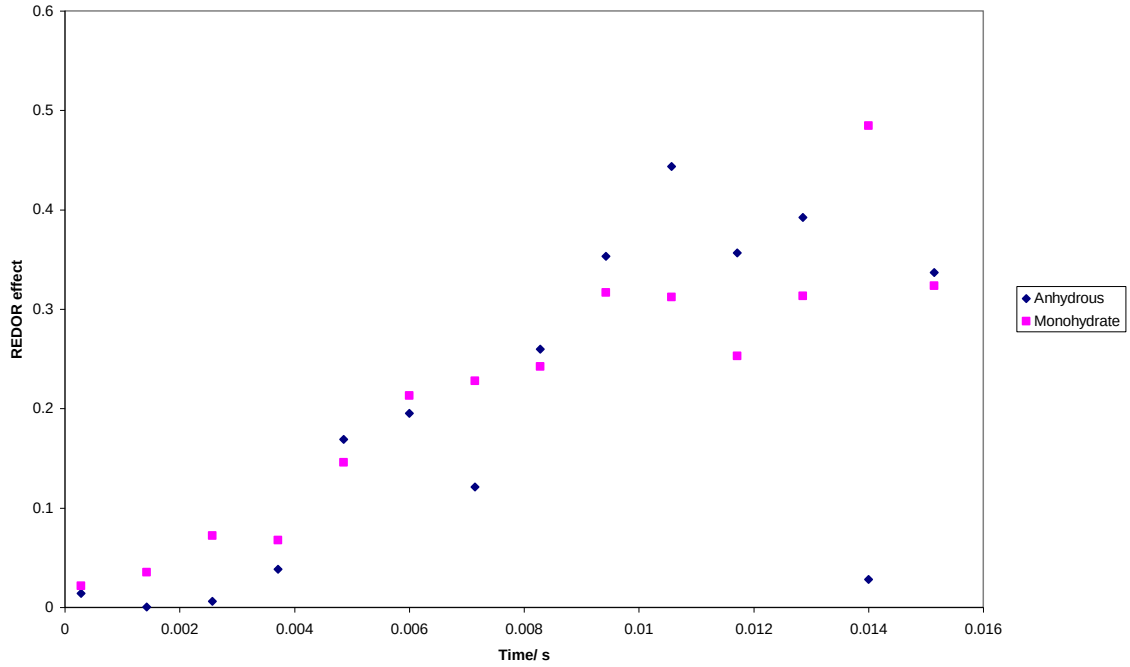

130 ppm

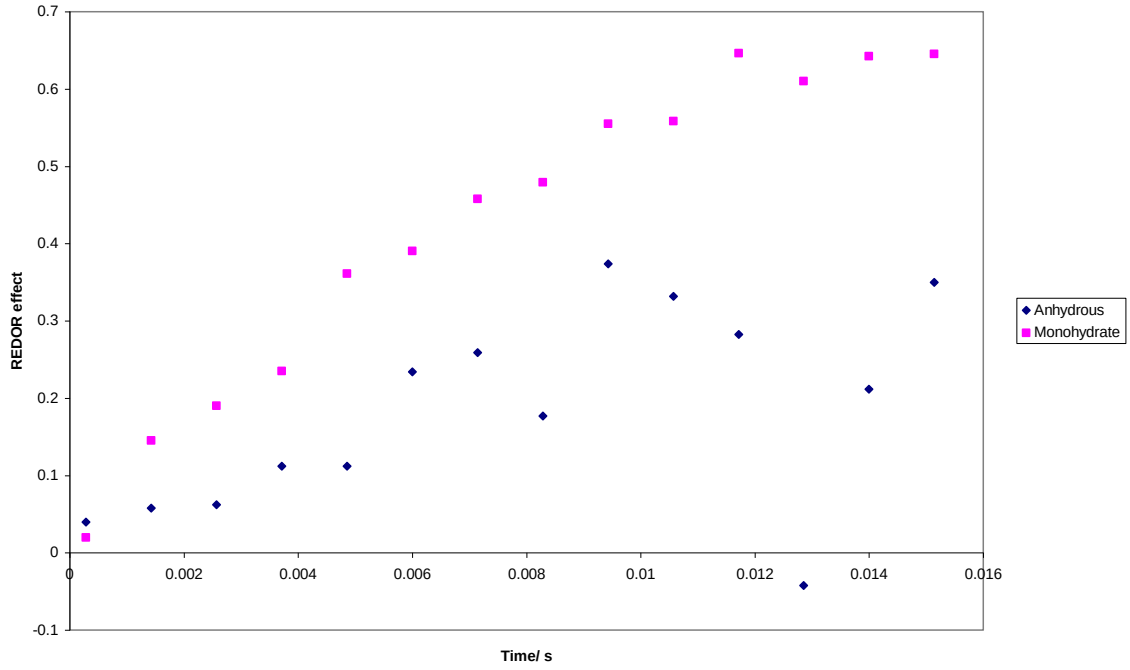

127 ppm

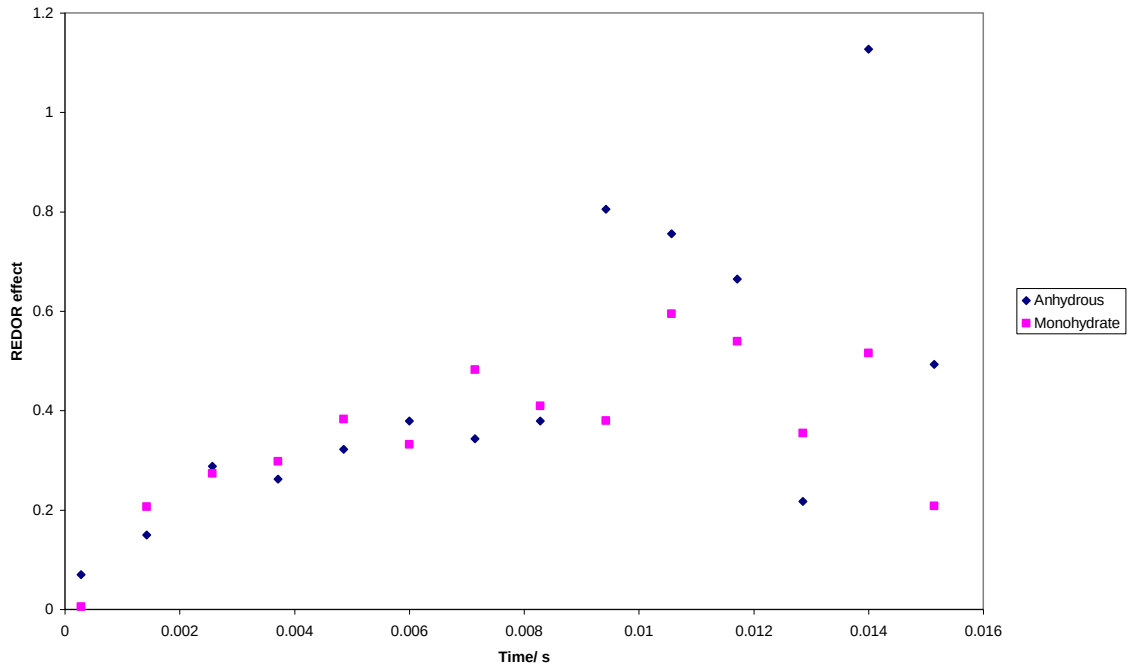

122 ppm

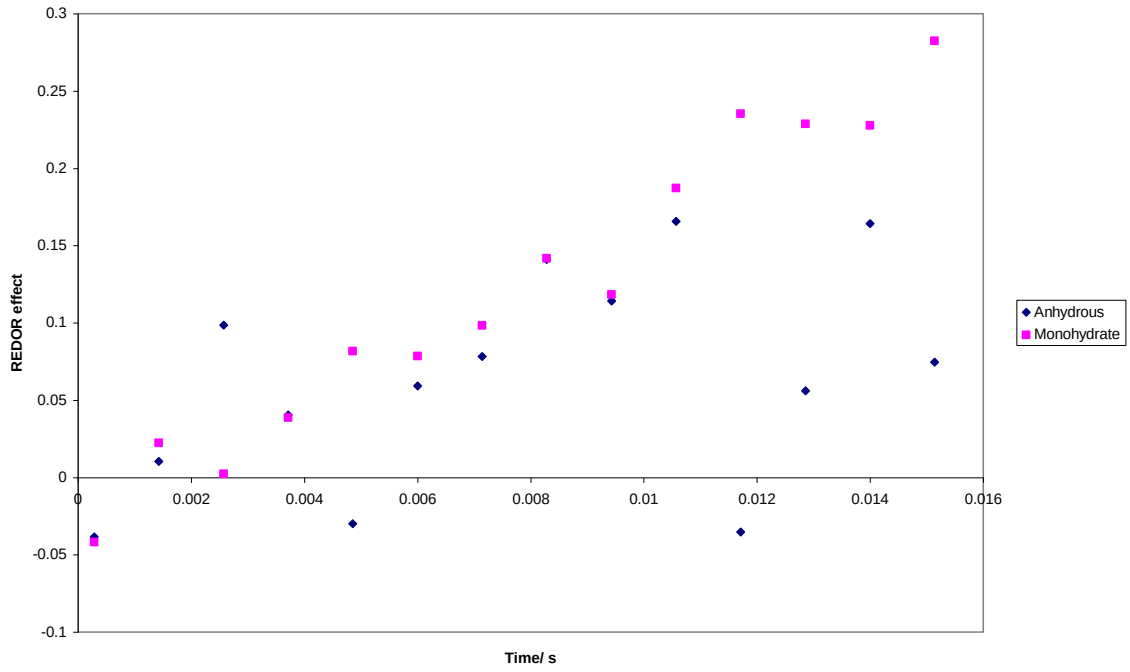

110 ppm

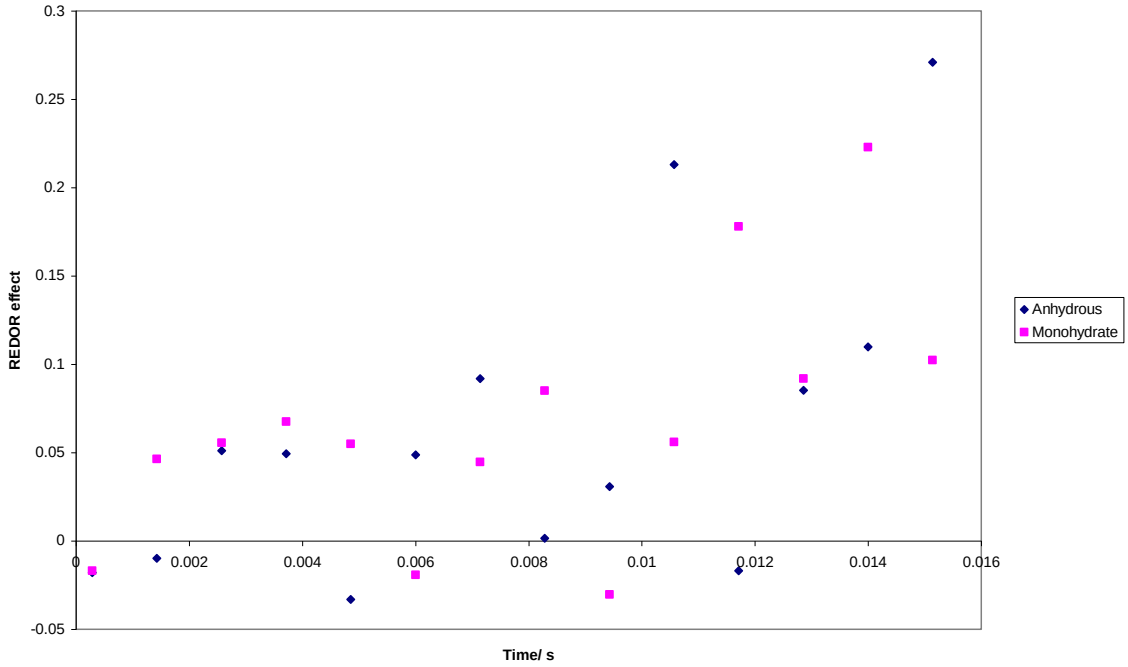

107 ppm

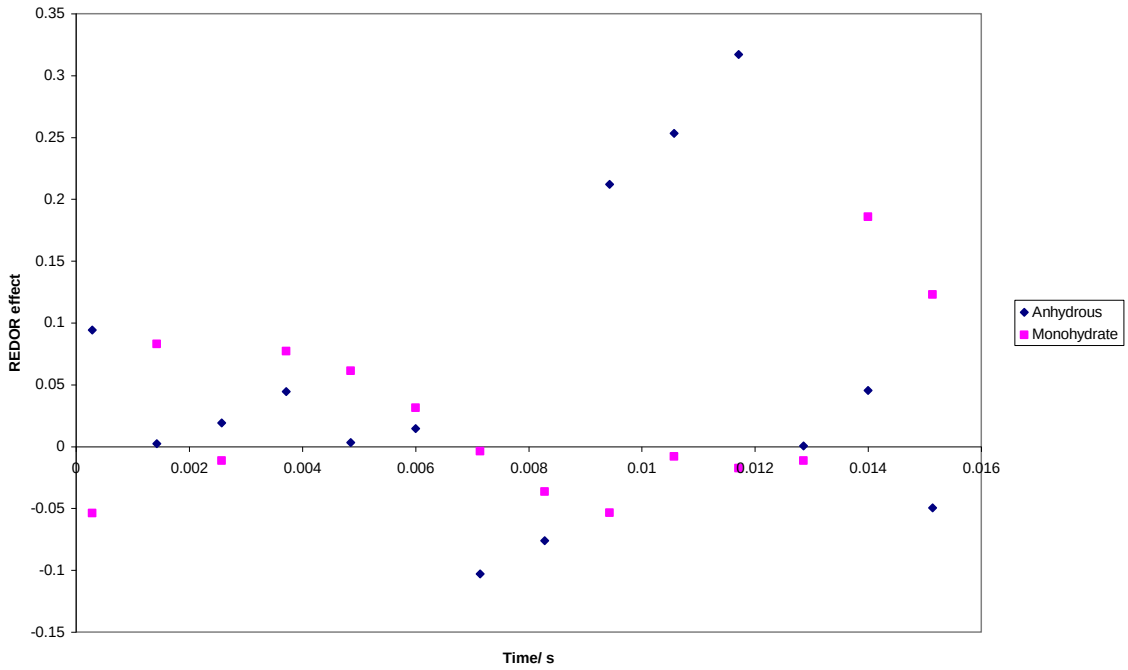

103 ppm

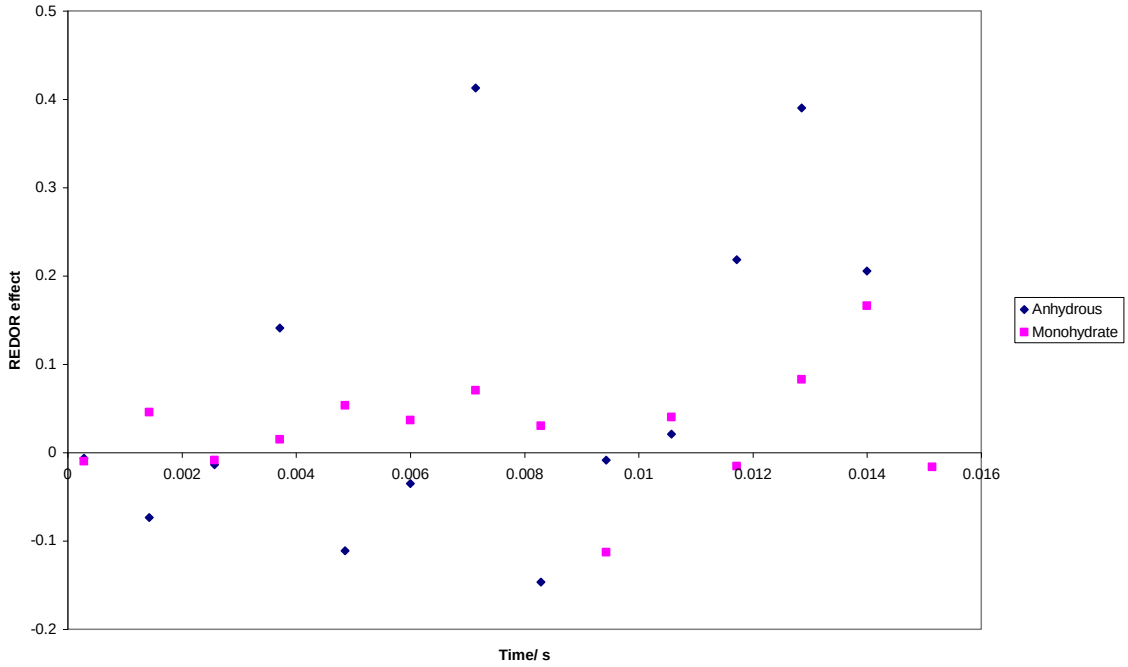
0.5
0.4
0.3
0.2
0.1
0
-0.1
-0.2
REDOR effect
0
0.002
0.004
0.006
0.008
0.01
0.012
0.014
0.016
Time/ s
Anhydrous
Monohydrate

73 ppm

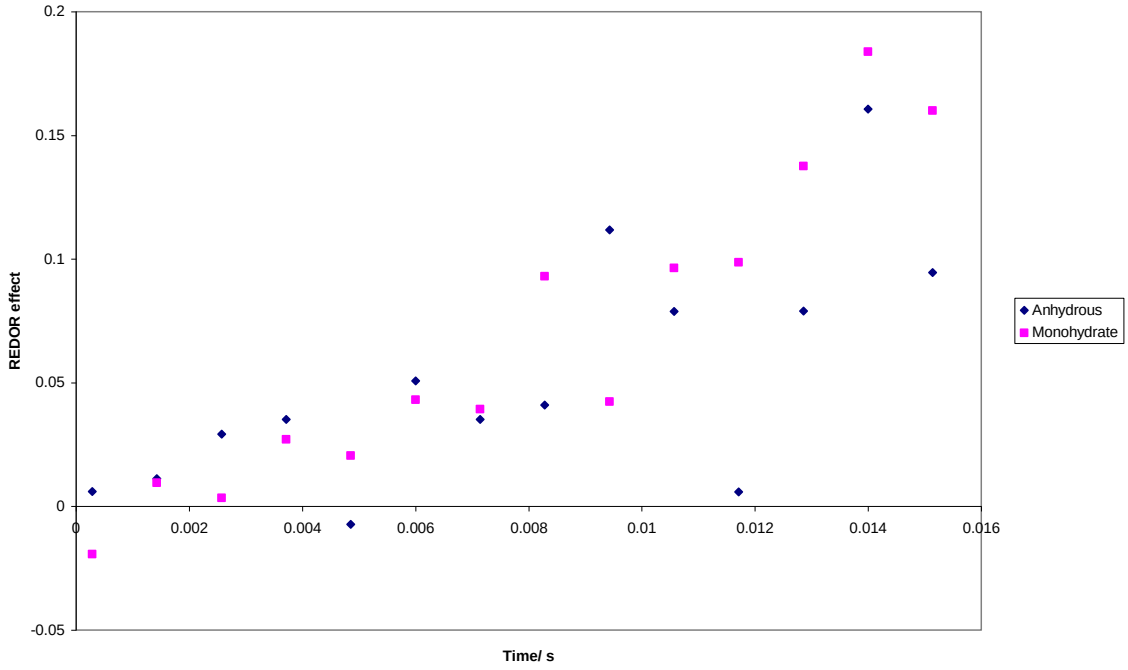
0.2
0.15
0.1
0.05
0
-0.05
REDOR effect
0
0.002
0.004
0.006
0.008
0.01
0.012
0.014
0.016
Time/ s
Anhydrous
Monohydrate

53 ppm

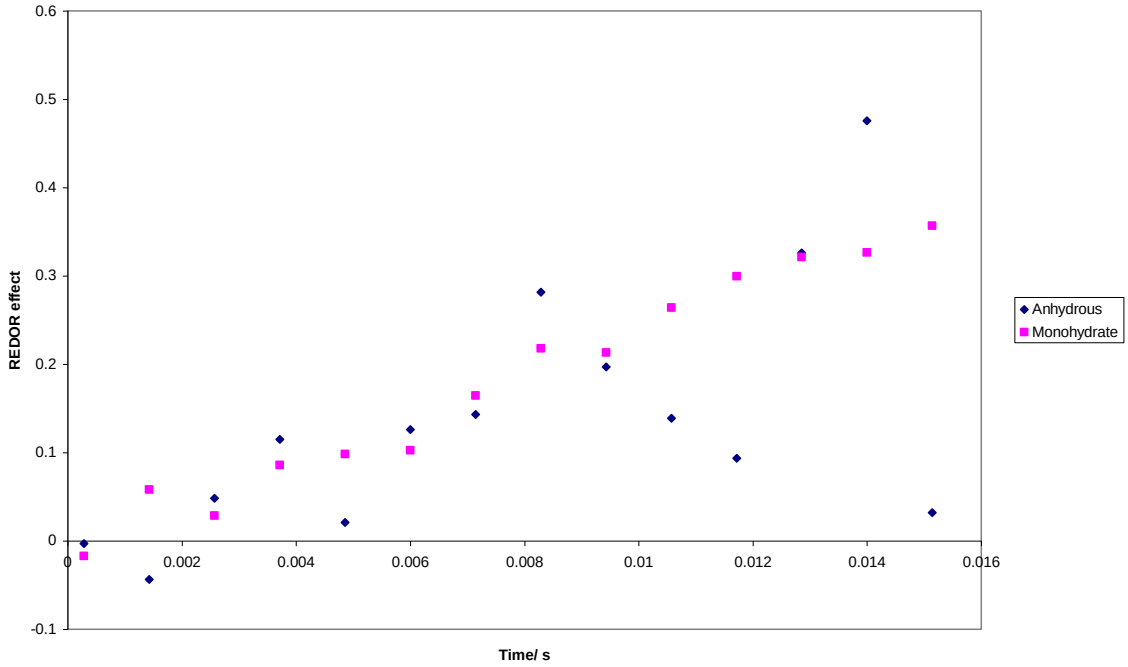
REDOR effect
Time/ s
Anhydrous
Monohydrate

45 ppm

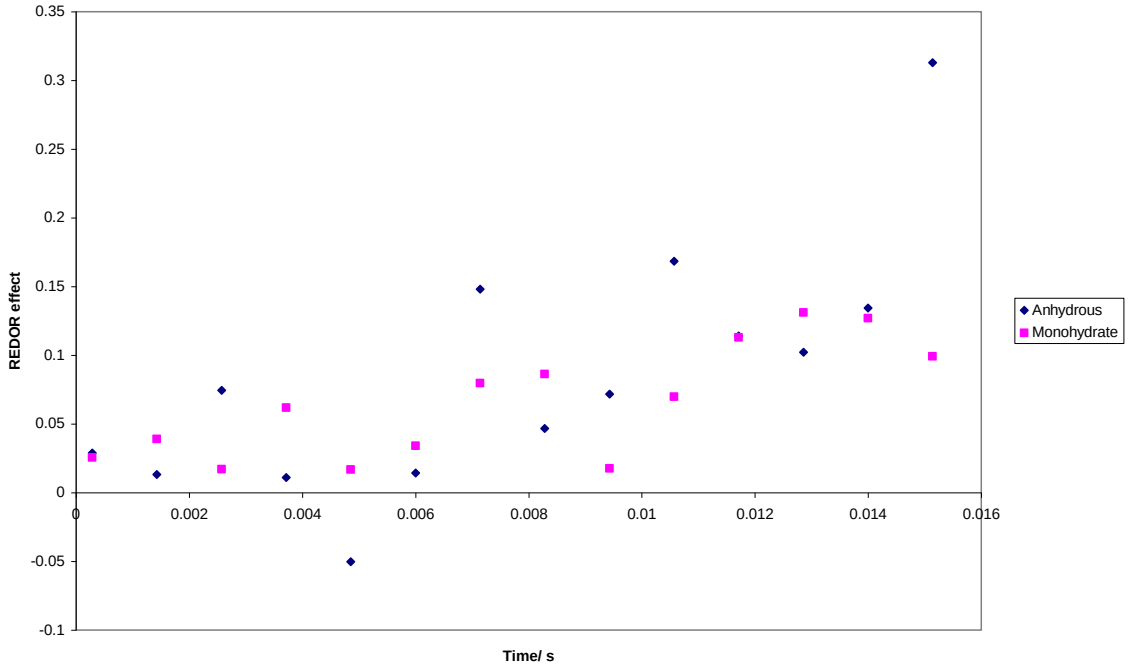
REDOR effect
Time/ s
Anhydrous
Monohydrate

36 ppm

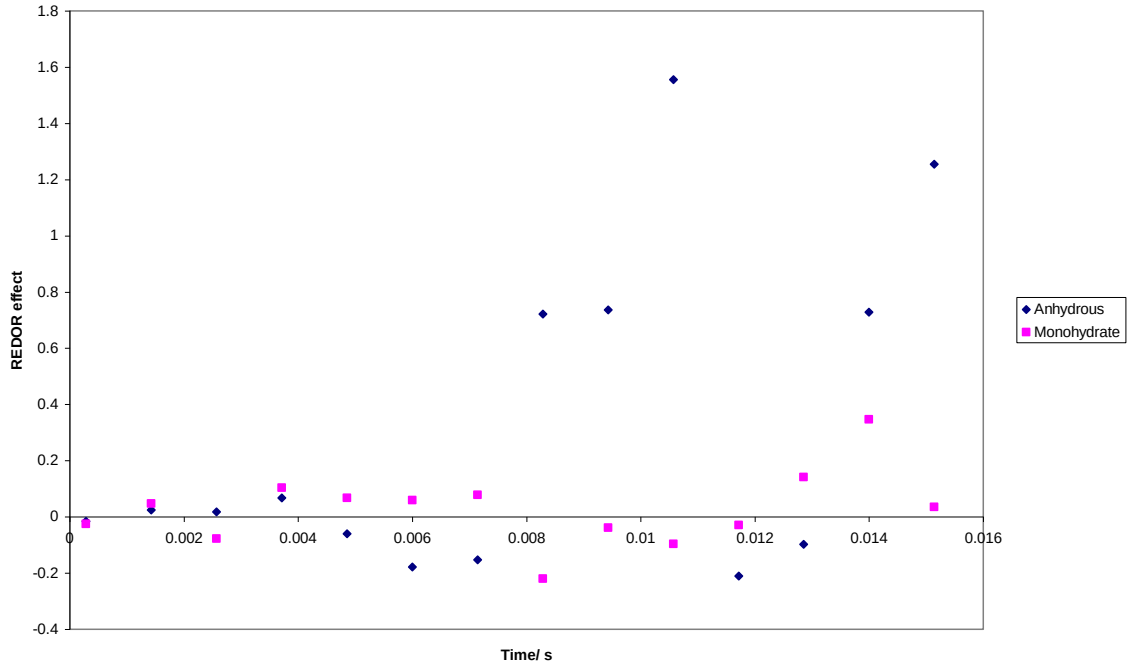

29 ppm

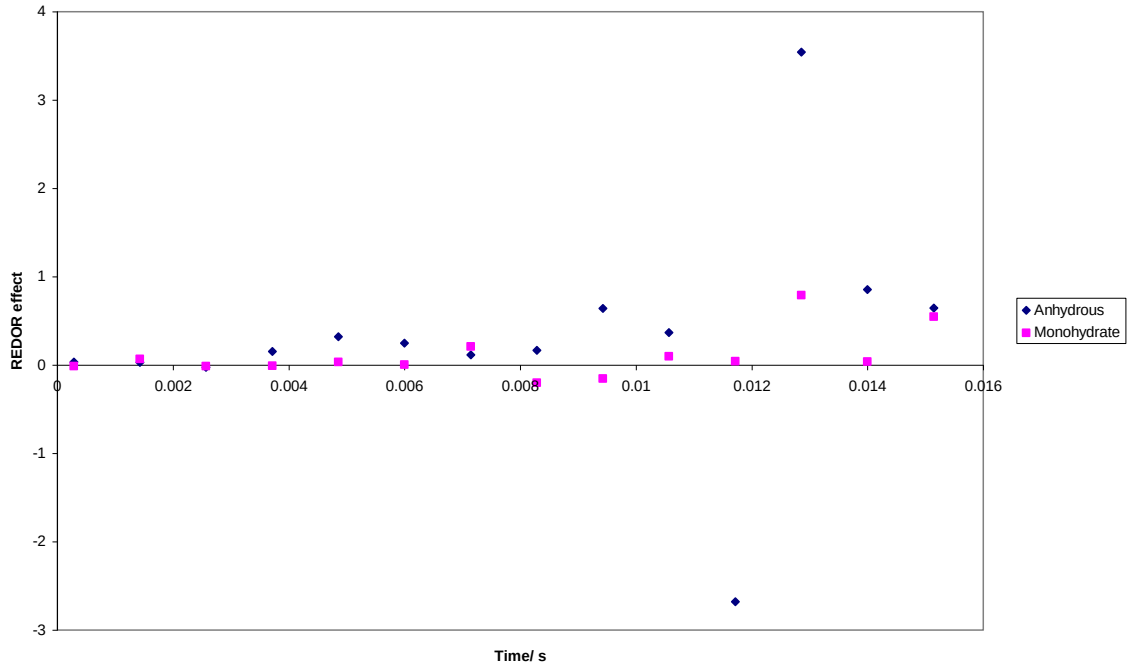

27 ppm

7.3 Appendix 3 (Macro to array condition for CP)

% create input file for ARRAY_FILE

maxcpmid = 0.50;

```
mincpmid = 0.50;

stepscpmid = 5;

cpmid = mincpmid+[0:stepscpmid-1]*(maxcpmid-mincpmid)/(stepscpmid-1);

maxramp = 0;
stepsramp= 5;

cpramp = [0:stepsramp-1]*maxramp/(stepsramp-1);

maxct = 0.005;
stepsct=0;
ctvals= 0.00001+ [0:stepsct-1]*maxct/(stepsct-1);

nexpts=stepsct*stepsramp*stepscpmid;

disp(['Number of experiments: ' num2str(nexpts)]);

exptpars=zeros(nexpts,3);

count=1;
maxaH=40.0;
for nmid=1:stepscpmid
  disp nmid;
  aHcp=cpmid(nmid);
  for nramp=1:stepsramp
    ramp=cpramp(nramp);
    aHcpend=aHcp+ramp/2;
    aHcpstart=aHcp-ramp/2;
    if (aHcpend>maxaH)
      maxaH=aHcpend;
       if (maxaH>1.0)
         error('Maximum amplitude exceeded');
     end
    end
    for nct=1:stepsct
      exptpars(count,:)= [ aHcpstart aHcpend ctvals(nct) ];
```

```
        count=count+1;
      end
    end
end

fid=fopen('exptpars','w');
fprintf(fid,'#created by makearray with (min/max)cpmid=%g,%g (%i steps), maxramp=%g
(%i steps), maxct=%g (%i
steps)\n',mincpmid,maxcpmid,stepscpmid,maxramp,stepsramp,maxct,stepsct);
fprintf(fid,'aHcp_start aHcp_end ct\n');
for i=1:count-1
  fprintf(fid,'%g\t%g\t%g\n',exptpars(i,1),exptpars(i,2),exptpars(i,3));
end
fclose(fid);
%save outfile exptpars -ascii;

disp(['Maximum aH:' num2str(maxaH)]);
```

7.4 Appendix 4 (Output of macro)

```
#created by makearray with (min/max)cpmid=0.5,0.5 (5 steps),
maxramp=0 (5 steps), maxct=0.005 (5 steps)
aHcp_start aHcp_end ct
0.5 0.5 1e-005
0.5 0.5 0.00126
0.5 0.5 0.00251
0.5 0.5 0.00376
0.5 0.5 0.00501
0.5 0.5 1e-005
0.5 0.5 0.00126
0.5 0.5 0.00251
0.5 0.5 0.00376
0.5 0.5 0.00501
0.5 0.5 1e-005
0.5 0.5 0.00126
0.5 0.5 0.00251
0.5 0.5 0.00376
0.5 0.5 0.00501
0.5 0.5 1e-005
0.5 0.5 0.00126
0.5 0.5 0.00251
0.5 0.5 0.00376
0.5 0.5 0.00501
0.5 0.5 1e-005
0.5 0.5 0.00126
0.5 0.5 0.00251
0.5 0.5 0.00376
0.5 0.5 0.00501
0.5 0.5 1e-005
```

```
0.5 0.5 0.00126
0.5 0.5 0.00251
0.5 0.5 0.00376
0.5 0.5 0.00501
0.5 0.5 1e-005
0.5 0.5 0.00126
0.5 0.5 0.00251
0.5 0.5 0.00376
0.5 0.5 0.00501
0.5 0.5 1e-005
0.5 0.5 0.00126
0.5 0.5 0.00251
0.5 0.5 0.00376
0.5 0.5 0.00501
0.5 0.5 1e-005
0.5 0.5 0.00126
0.5 0.5 0.00251
0.5 0.5 0.00376
0.5 0.5 0.00501
0.5 0.5 1e-005
0.5 0.5 0.00126
0.5 0.5 0.00251
0.5 0.5 0.00376
0.5 0.5 0.00501
0.5 0.5 1e-005
0.5 0.5 0.00126
0.5 0.5 0.00251
0.5 0.5 0.00376
0.5 0.5 0.00501
0.5 0.5 1e-005
0.5 0.5 0.00126
0.5 0.5 0.00251
0.5 0.5 0.00376
0.5 0.5 0.00501
0.5 0.5 1e-005
0.5 0.5 0.00126
0.5 0.5 0.00251
0.5 0.5 0.00376
0.5 0.5 0.00501
0.5 0.5 1e-005
0.5 0.5 0.00126
0.5 0.5 0.00251
0.5 0.5 0.00376
0.5 0.5 0.00501
0.5 0.5 1e-005
0.5 0.5 0.00126
0.5 0.5 0.00251
0.5 0.5 0.00376
0.5 0.5 0.00501
0.5 0.5 1e-005
0.5 0.5 0.00126
```

```
0.5 0.5 0.00251
0.5 0.5 0.00376
0.5 0.5 0.00501
0.5 0.5 1e-005
0.5 0.5 0.00126
0.5 0.5 0.00251
0.5 0.5 0.00376
0.5 0.5 0.00501
0.5 0.5 1e-005
0.5 0.5 0.00126
0.5 0.5 0.00251
0.5 0.5 0.00376
0.5 0.5 0.00501
0.5 0.5 1e-005
0.5 0.5 0.00126
0.5 0.5 0.00251
0.5 0.5 0.00376
0.5 0.5 0.00501
0.5 0.5 1e-005
0.5 0.5 0.00126
0.5 0.5 0.00251
0.5 0.5 0.00376
0.5 0.5 0.00501
0.5 0.5 1e-005
0.5 0.5 0.00126
0.5 0.5 0.00251
0.5 0.5 0.00376
0.5 0.5 0.00501
0.5 0.5 1e-005
0.5 0.5 0.00126
```

7.5 Appendix 5 (Tan array)

```
% create input file for ARRAY_FILE

maxcpmid = 0.37;
mincpmid = 0.27;

stepscpmid = 6;

cpmid = mincpmid+[0:stepscpmid-1]*(maxcpmid-mincpmid)/(stepscpmid-1);

maxramp = 0.2;
stepsramp= 6;

cpramp = [0:stepsramp-1]*maxramp/(stepsramp-1);

maxct = 0.002;
stepsct=11;
ctvals= 0.00001+ [0:stepsct-1]*maxct/(stepsct-1);
```

```
maxtan = 0.05;
stepstan = 4;
tanvals=[0:stepstan-1]*maxtan/(stepstan-1);

nexpts=stepsct*stepscpmid*( (stepsramp-1)*stepstan + 1);

disp(['Number of experiments: ' num2str(nexpts)]);

exptpars=zeros(nexpts,4);

count=1;
maxaH=0.0;
for nmid=1:stepscpmid
  aHcp=cpmid(nmid);
  for nramp=1:stepsramp
    ramp=cpramp(nramp);
    if (ramp==0.0)
      usestepstan=1;
    else
      usestepstan=stepstan;
    end
    for ntan=1:usestepstan
      aHcplinear=aHcp+ramp/2;
      aHcpstart=aHcplinear+tanvals(ntan);
      aHcpend=aHcp-ramp/2-tanvals(ntan);
      if (aHcpend<0)
        error('Amplitude below zero!');
      end
     if (aHcpstart>maxaH)
       maxaH=aHcpstart;
      if (maxaH>1.0)
       error('Maximum amplitude exceeded');
     end
     end
     for nct=1:stepsct
       exptpars(count,:)= [ aHcpstart aHcplinear aHcp ctvals(nct) ];
       count=count+1;
```

```
      end
    end
  end
end

if (count ~= nexpts+1)
  error('Miscounted experiments');
end

fid=fopen('tanarray','w');
fprintf(fid,'#created by maketanarray with (min/max)cpmid=%g,%g (%i steps), maxramp=%g
(%i steps), maxtan=%g (%i steps), maxct=%g (%i
steps)\n',mincpmid,maxcpmid,stepscpmid,maxramp,stepsramp,maxtan,stepstan,maxct,stepsct
);
fprintf(fid,'aHcp_start aHcp_linear aHcp ct\n');
for i=1:count-1
  fprintf(fid,'%g\t%g\t%g\t%g\n',exptpars(i,1),exptpars(i,2),exptpars(i,3),exptpars(i,4));
end
fclose(fid);

disp(['Maximum aH:' num2str(maxaH)]);
```

7.6 Appendix 6 (Spectrometer optimisation)

```
% create input file for ARRAY_FILE

maxcpmid = 30;
mincpmid = 10;

stepscpmid = 6;

cpmid = mincpmid+[0:stepscpmid-1]*(maxcpmid-mincpmid)/(stepscpmid-1);

maxramp = 20;
stepsramp= 6;

cpramp = [0:stepsramp-1]*maxramp/(stepsramp-1);
```

```
maxct = 20;
stepsct = 21;
ctvals= 10 + [0:stepsct-1]*maxct/(stepsct-1);

nexpts=stepsct*stepsramp*stepscpmid;

disp(['Number of experiments: ' num2str(nexpts)]);

exptpars=zeros(nexpts,3);

count=1;
maxaH=1000.0;
for nmid=1:stepscpmid
  disp nmid;
  aHcp=cpmid(nmid);
  for nramp=1:stepsramp
    ramp=cpramp(nramp);
    aHcpend=aHcp+ramp/2;
    aHcpstart=aHcp-ramp/2;
    if (aHcpend>maxaH)
      maxaH=aHcpend;
       if (maxaH>1.0)
         error('Maximum amplitude exceeded');
     end
    end
    for nct=1:stepsct
      exptpars(count,:)= [ aHcpstart aHcpend ctvals(nct) ];
      count=count+1;
    end
  end
end

fid=fopen('exptpars','w');
fprintf(fid,'#created by makearray with (min/max)cpmid=%g,%g (%i steps), maxramp=%g
(%i steps), maxct=%g (%i
steps)\n',mincpmid,maxcpmid,stepscpmid,maxramp,stepsramp,maxct,stepsct);
fprintf(fid,'A1 B1 period\n');
for i=1:count-1
```

```
  fprintf(fid,'%g\t%g\t%g\n',exptpars(i,1),exptpars(i,2),exptpars(i,3));
end
fclose(fid);
%save outfile exptpars -ascii;

disp(['Maximum aH:' num2str(maxaH)]);
```

7.7 Appendix 7 (Calculate CP efficiency)

```
% calculate APHH performance using full two spin model

Sn=1; In=2;
sys=[1/2 1/2];

Soff=20e3;
Ioff=0e3;

betasteps=40;
betaang=57.4;

d = 1e3;

theta=1*pi/180;
steps=30;

delta = -40e3; % aHcp_linear - aHcp / Hz
aHcp=80e3; % aHcp / Hz
aXcp=80e3; % aXcp / Hz

Hrf=S(sys,In,'x');
H0=aXcp*S(sys,Sn,'x')+aHcp*Hrf+Ioff*S(sys,In,'z')+Soff*S(sys,Sn,'z');
Hdip=2*S(sys,Sn,'z')*S(sys,In,'z');

sigma0=S(sys,In,'x');
detect=S(sys,Sn,'x');

beta=delta/theta;
```

```
aHmax= beta*tan(theta);
disp(['aHstart - aHcp: ' num2str(aHmax)]);
maxct = 5e-3;
ctsteps=40;

amp=zeros(1,ctsteps);
ctscale=[1:ctsteps]*maxct/ctsteps;

rf=zeros(1,steps);
for j=1:steps
   t=(j-1)/(steps-1)-0.5;
   rf(j)=beta*tan(2*theta*t);
end

figure(1);
plot(rf/1e3);
ylabel('aH - aHcp / kHz');

for k=1:ctsteps
  ct=ctscale(k);
  dt=ct/steps;

  v=0;
  for p=1:betasteps
    if (betasteps>1)
      betaang=pi*p/(betasteps+1);
      betascale=sin(betaang);
    else
      betascale=1;
    end
    p2=(3*cos(betaang)^2-1)/2;
    Hbase=H0+d*p2*Hdip;
    Utot=eye(4);
    for j=1:steps
      H=Hbase+rf(j)*Hrf;
      U=expm((-2*pi*i*dt)*H);
      Utot=U*Utot;
    end
```

```
    sigmat=Utot*sigma0*Utot';
    v=v+betascale*trace(sigmat*detect);
  end
  amp(k)=v;
end
amp=amp/betasteps;

figure(2);
plot(ctscale*1e3,amp);
xlabel('time / ms');
```

7.8 Appendix 8 Use of macros in CP investigation

In order to make the most efficient use of time, a series of macros were created to aid the optimisation of the CP process. The majority of macros designed were used to create suitable experimental parameters for the CP process. Macros are generally preferred as they have a number of advantages in comparison to typical manual methods, when creating large arrays.

The main advantage of using macros is the time saving factor that they provide, as macros are commonly used to perform routine tasks. The generation of large arrays is a classic example of where a macro can be used to perform a routine task. When designing the macro it was important to ensure that it was sufficiently flexible enough so it could be used for a number of situations, this would mean that one macro could be used for a number of times for different experiments.

As well as the time saving advantage associated with macros they also reduce the risk of human error. When large arrays are setup it is possible that incorrect parameters may be entered if doing so manually. Due to the systematic method in the way macros work, this is not possible. It is also possible within the macro to have maximum power settings than can be used, as measure of protection to prevent out of specifications powers being used. As an extra precaution a summary of the parameters being used can be displayed, once again ensuring that only suitable conditions are used.

Due to the nature of the setup of the ramps, it was possible to combine all the macros that are used to provide the experimental parameters into one. Just one macro is now possible to produce both positive and negative ramps, with varying midpoint. The macro is sufficiently flexible, that it can be used to create the parameters for a tangential ramp.

7.9 Appendix 9 Long ct for chitin/chitosan

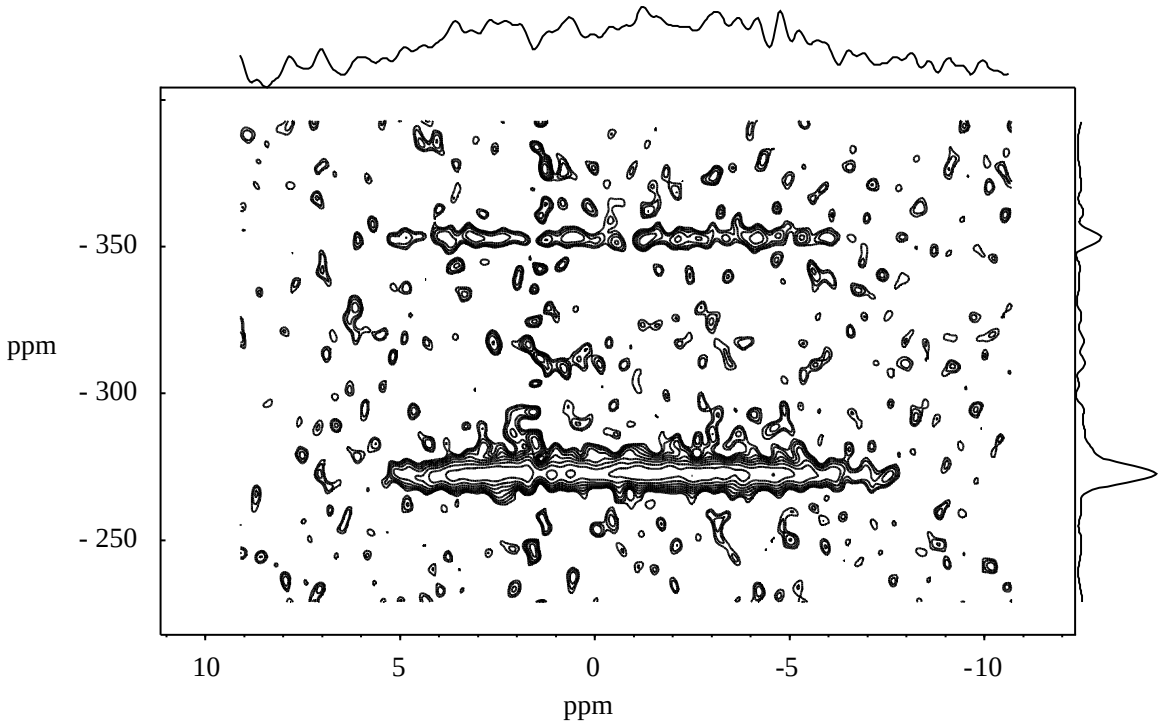

Figure 88 Inverse detection of chitosan and chitin mixture with long contact time

7.10 Appendix 10 (Inhomogeneous contribution)

```
% inhomogenous and homogenous simulation
sw=1000; % spectral width/ Hz
%frequencies of lines
% linepos= [ 270 330 670 730];
% indicates which peaks are 'active'
% correlmap= eye(4);
 correlmap(1,3)=1;
 linepos =[300 700];
 correlmap=[1 1 ; 1 1];
```

```
homolwlor = 30; % Homogeneous linewidth (lorenztian) / Hz
homolwgauss = 0; % Homogeneous linewidth (gaussian) / Hz

inhomolw = 100; % Inhomogeneous distribution width (gaussian) / Hz

corfac = 0.20; % degree of correlation between inhomogeneous frequencies

freqbins = 80; % number of spectral bins


inhomolwmin=inhomolw*sqrt(1-corfac*corfac);

npeaks=length(linepos);

basemap=zeros(freqbins,freqbins);

c=1/sqrt(2);
irotm=[ c c; -c c];
rotm = [ c -c ; c c];

gaussfac=pi/(2*sqrt(log(2)));

junk=zeros(freqbins,freqbins);
for r=1:freqbins
  for c=1:freqbins
    mapint=0.0;
    freqr=(r-1)*sw/freqbins;
    freqc=(c-1)*sw/freqbins;
    for ni=1:npeaks
      for nj=1:npeaks
        correlint=correlmap(ni,nj);
        if (correlint~=0)
          diff=[freqr-linepos(ni); freqc-linepos(nj) ];
          if (corfac>0)
            rot=irotm*diff;
          else
            rot=rotm*diff;
```

```
            end
            kmaj=gaussfac*rot(1)/inhomolw;
            kmin=gaussfac*rot(2)/inhomolwmin;
            mapint=mapint+correlint*exp(-kmaj*kmaj-kmin*kmin);
          end
        end
      end
      basemap(r,c)=mapint;
    end
end

scale=[0:freqbins-1]*sw/freqbins;
figure(1);
pcolor(scale,scale,basemap);
xlabel('f1'); ylabel('f2');

% apply homogeneous lw

lwbins=20;

%fid=ifft2(basemap);
inds=[0:freqbins-1];
dt=1/sw;
gaussx = inds*dt*gaussfac*homolwgauss;
gaussmult=exp(-(gaussx.*gaussx));
t2=1/(2*pi*homolwlor);
lormult= exp(-inds*dt/t2);
totmult=gaussmult.*lormult;
totmult(1)=0.5;
freqmult=real(fft(totmult));
weight=zeros(freqbins,freqbins);

for r=1:freqbins
  for c=1:freqbins
    w=freqmult(r)*freqmult(c);
    weight(r,c)=w;
    %refr=freqbins-r+1;
    %refc=freqbins-c+1;
```

```
    %weight(refr,refc)=0.0;
  end
end

%newfid = fid.*weight;
%spec=fft2(newfid);
spec=real(conv2(basemap,fftshift(weight),'same'));
maxv=max(max(spec));
conlev=[4 6 8 12 16 24 32 48 64 ]*maxv/100;

figure(2);
contour(scale,scale,spec,conlev);
xlabel('f1'); ylabel('f2');

axis square;
```